Synthesis and Application of Novel Fluorescent Molecules

PhD student: Cheng Cheng
Supervisor: Prof. Enzo Terreno

2024-02-29

Contents

Abstract

The development of simple, inexpensive, sensitive, and selective bioanalytical methods is essential for advancing many aspects of life research, such as the diagnosis and treatment of disease, drug delivery, forensic identification, environmental monitoring, and quality monitoring of industrial products.etc. are essential. Organic small molecule fluorescent probes are widely used in fluorescence-based bioanalytical sensing due to their excellent properties. Meanwhile, aggregation-induced emission (AIE) molecules have excellent properties, such as good photostability, thermal stability, chemical inertness, high fluorescence quantum yield, and long fluorescence lifetimes, which are of great significance for analytical applications. In addition, perylene-3,4,9,10-tetracarboxylic acid and phorbol series derivatives are good precursors for the synthesis of fluorescent probes with a variety of properties and structures as well as promising applications. Therefore, we have synthesized perylenimine compounds (PBIs), cyanine derivatives, and AIE molecules, extensively investigated their properties, and developed a series of applications. On this basis, we present the development and application of various fluorescent probes customized for specific sensing tasks. These probes are suitable for a variety of fields ranging from chemical detection to healthcare, safety and product authentication. The main results of the paper are listed below:

1. Nitric oxide (NO) sensing N-PBI: Nitric oxide (NO) plays a crucial role in physiology and pathology, so the development of highly sensitive and selective fluorescent probes for its detection is essential. In this study, a novel NO sensing fluorescent probe, N-PBI, was synthesized, which exhibits excellent sensitivity, low detection limit, and fast response time compared to existing probes. Detailed property studies and cellular imaging further highlighted its application value. Notably, the probe was embedded in a thin film for sensitive detection of nitric oxide in air, thus expanding its utility and demonstrating its great potential in the detection of NO.
2. BN-bonded sensor (BNOH) for efficient detection of picric acid (PA): Trace Detection of Nitro Explosives Plays Important Role in Homeland Security. This section outlines the design and synthesis of a BN-bonded sensor, BNOH, for the detection of picric acid (PA).

BNOH is easily synthesizable and highly yielding, and possesses an aggregation-induced emission (AIE) effect, and its solid-bright fluorescence makes it an excellent sensor. BNOH exhibits excellent selectivity and sensitivity with detection limits up to the ppb level. The PA response mechanism of BNOH was explored by a computational simulation approach. Notably, this study demonstrated that trace solid PA can be easily and rapidly detected using the BNOH paper sensor.

3. pH sensing arrays for cosmetic certification pC: Cosmetic consumption is a hot issue of concern, and in the context of cosmetic certification, we designed and synthesized pH sensors and applied them to ensure cosmetic safety. The study started with the design of two probes, CH with aggregation-induced emission (AIE) properties and the near-infrared fluorophore derivative CYTYR. By encapsulating these probes in DSPE-PEG2000-NH2, CYCH nano-micelles with fluorescence resonance energy transfer (FRET) response were generated. These probes were combined into a sensor array called PC for sensitive detection over a wide pH range (5.25 to 9.05.) The PC sensor array effectively differentiated anti-aging creams from different countries, providing a fast and accurate method for cosmetic safety identification, and demonstrating its significant potential in the consumer health and cosmetic safety industries.
4. "Clinical" Liposomal CST for Sensitive Hypochlorite Detection: Hypochlorite (HClO) plays an important role in the body, and inflammation is often accompanied by aberrant expression of hypochlorite. Therefore, the development of sensitive hypochlorite detection probes is urgent. Two probes, Se-TPA and CYLYS, were designed, synthesized and characterized. se-TPA has aggregation-induced emission properties and CYLYS is a near-infrared emitting fluorophore. Both probes were used to create a clinical liposome CST with FRET effects, enabling the proportional detection of hypochlorous acid. The CST had a wide detection range (0-30 μM) and a detection limit as low as 17.5 nM. Computational simulations and mass spectrometric characterization confirmed the response mechanism. Selectivity and stability tests produced good results, demonstrating the potential of CST for hypochlorite detection and imaging of rheumatoid arthritis.

Abstract

Key words: Fluorescent probes, aggregation-induced emission (AIE), fluorescence resonance energy transfer (FRET), Nitric oxide (NO) sensing, picric acid (PA) detection, pH sensing arrays, hypochlorite detection, homeland security, cosmetic certification, inflammation.

Chapter 1 Introduction

1.1 Introduction

This thesis describes the synthesis of a series of fluorescent probes and a detailed study of their structural and property characterization. New AIE molecules have been synthesized and their properties revealed, thus expanding the understanding of their possible applications and developing simple, fast and convenient methods for the analysis of sensing and interfacial applications. Chapter 1 demonstrates in detail the basic concepts and principles underlying the subject of the experimental study.

1.2 Photoluminescence: Theory and Principle

Photoluminescence (PL) is a phenomenon of light emission from a matter after being excited by a photon. It is one of the forms of luminescence. Photoluminescence examines the electronic structure and optical properties of luminogenic materials and is a nondestructive technology. After being excited various process of relaxation with variable time domains typically occur ranging from femtoseconds in plasma to milli-seconds in molecular systems. In special cases, emission may delay up to minutes or hours. Based on the time domain PL is classified into phosphorescence (Long-time) and fluorescence (Short-time). Phosphorescence is a phenomenon where molecules relaxed from excited singlet state to the ground singlet state passing through an excited triplet state. The excited triplet state has a much longer lifetime, thus it is a delay process and the spin of an electron is inverted during the process. So it is quantum mechanically a forbidden transition. In contrary fluorescence is a kind of PL where molecules relaxed to the ground singlet-state from an excited singlet-state without changing the electron spin. Thus it is fast and allowed transition with excited state lifetime of 10^{-9} - 10^{-6} s.[1-3]

1.3 The Basic Concept of Fluorescence

Fluorescence is the member of ubiquitous luminescence family of processes that involves the absorption of light of a particular wavelength and emission at a longer wavelength on relaxation after a short interval of time term as fluorescence lifetime. [2-5]The mechanism of fluorescence involves three basic events. The excitation of the molecular system by an incoming photon that particularly occurs in femtoseconds (10^{-15} s), the vibrational relaxation of the excited electron to the ground vibrational level that occurs in picoseconds (10^{-12}s) and the emission of a photon

at a longer wavelength. Thus the molecules return to the ground state relatively at the time period of nanoseconds (10^{-9}s). In fact, the phenomenon of fluorescence is the stunning manifestation of the molecular interactions with electromagnetic radiations (EMR). The expensive fields of time-resolved and steady-state spectroscopy and microscopy were originated on the basis of these interactions. [1, 2, 4, 5]These techniques are rapidly becoming significant tools in various disciplines such as biosensing, genetics, medicine, and cell biology etc.[3, 6-10] [11, 12]

The term fluorescence was first coined in honor of fluorspar (a blue-white fluorescent mineral) in 1852 by Sir George G. Stokes.[13] And he described the phenomenon of fluorecence for the first time. The wavelength shift to longer values was named as Stokes shift that bears his name. Two German physicists Otto Heimstadte and Henrich Lehmann together developed first fluorescence microscope in 1913 that was the mildstone discovery of the time. The study of dye binding in tissues and living cells employing fluorescence microscopy by Stanislav Von Provazek had launched a new era. In 1940s immunofluorescence was emerged as a new field introduced by Albert Coons by developing a technique for labeling antibodies with fluorescent dyes. Thus in the 21st-century fluorescence microscopy has revolutionized the cell biology and genetics by coupling the power of cell imaging and molecular systems with encoded fluorescent probes. [3, 11, 14, 15]

Highly conjugated polycyclic aromatic hydrocarbons are generally associated with fluorescence. For any specific molecules there exist different electronic states termed as S_0, S_1, …. S_n. Each electronic state further comprises of vibrational and rotational levels. In the ground state, all electrons are spin paired. At room temperature, most of the molecules exist in the lowest vibrational level of the ground state. Thus excitation process begins from this level. [16-18] A group of molecules that can undergo the electronic transition and induce the fluorescence are termed as fluorochromes or fluorescent probes. [3, 6, 9, 19, 20] In fluorochromes, absorption occurs in different molecular orbitals between closely spaced vibrational and rotational energy levels of excited states. Jablonski energy diagram best describes the various energy levels involved in the absorption and emission of EMR by fluorochromes (**Fig. 1.1**).

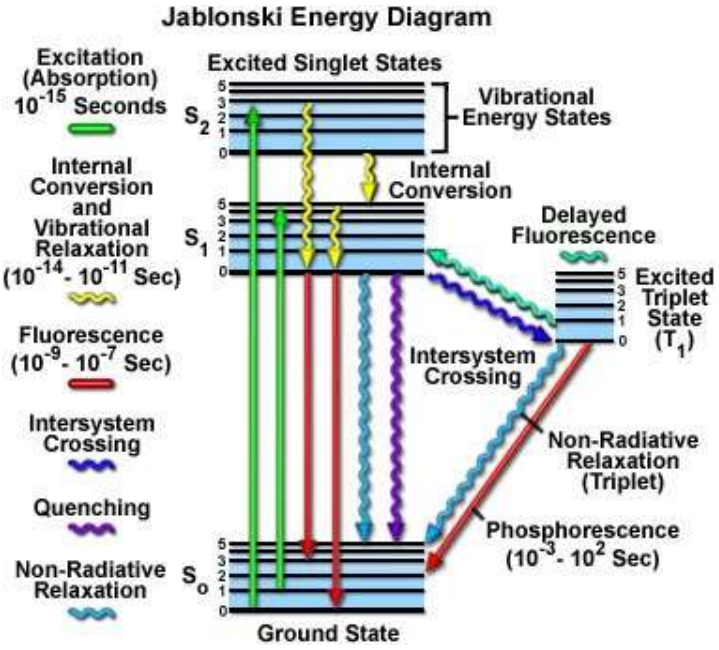

Fig. 1.1: The typical Jablonski diagram illustrating the luminescence processes in fluorochromes. [3]

A typical Jablonski diagram illustrates the singlet ground state, first and second excited states as S_0, S_1, and S_2, respectively. The transition between states is illustrated by lines. The straight lines are associated with absorption and emission process and wavy lines denote the non-radiative relaxations process or molecular internal conversion. [3]

The emission of a photon from an excited fluorochrome is measured in terms of quanta. The Plank's law best describes the energy in a quantum in terms of equation

$$E = hv = hc/\lambda$$

Where E, v, and λ are the energy, frequency and wavelength of photon, h is planks constant and c is the speed of light. The absorption of a photon by the fluorochromes occurs due to the interaction of oscillating electric field vectors of EMR with electrons in the molecules and it only occurs with specific wavelength termed as absorption band. The broad absorption bands in emission spectra arise from the closely spaced vibrational levels and thermal motion. The fluorescence studies were conducted usually in the wavelength range of 250 to 700 nm. Several processes occur after the absorption of a photon. The most likely event is the relaxation to the lowest vibrational level of S1. The process is termed as internal conversion. The fluorochromes

mostly undergo excitation and emission process hundreds to thousands of time before the excited molecules photobleached. Various relaxation processes with varying degree of probability compete with fluorescence. The molecules should undergo spin conversion to produce unpaired electrons. It indicates the low probability of the intersystem crossing. In the triplet state molecules exhibit a high degree of chemical reactivity. It results in photobleaching and the generation of toxic free radicals. For instance, oxygen is an effective quenching agent for most fluorophores in the triplet state. The triplet molecular oxygen excites to the reactive singlet oxygen and bleaches the fluorophore or exhibit the phototoxic effect on living cells. [21] The Frank Condon principle describes the probability of occurring a transition. According to this rule, the degree of similarity between the vibrational and rotational energy states defines the transition from the ground state to the excited singlet state. The nuclear configuration of the molecules does not change due to the faster transition. [15]

1.4 Fundamental Parameters of Fluorochromes

The efficiencies of fluorochromes are usually described in terms of three fundamental parameters that include molar absorption coefficient, quantum yield and lifetime. [22]The molar absorption coefficient (Ɛ) is the measure of the ability of fluorochrome to absorb EMR. The fluorochromes holding high Ɛ values have more probability of fluorescence emission. [3] The quantum yield (Φ) is the measure of the efficiency of fluorescence emission relative to the total possible ways of relaxation. In general, it is the ratio of a number of photons emitted to the number of photons absorbed. The value ranges between 0-1. The high quantum yield is desirable for sensitive applications. The quantum yield can be expressed mathematically as

$$\Phi = \frac{\text{Photons emitted}}{\text{Photons Absorbed}}$$

The value of Φ of a fluorochrome varies with the environmental conditions such as pH, concentration, and solvent system.

The fluorescence lifetime is the time a fluorochrome spare at excited state prior to coming to the ground state. It is a parameter to gather the information from emission profile. The fluorophores usually undergo conformational changes and interact with other molecules during the excited state lifetime. The decay of fluorescence intensity as a function of time can be

described by the equation

$$I(t) = I_o . e^{(-t/\tau)}$$

Where I(t) is the intensity of fluorescence measured at time t, I_o is the initial intensity at t = 0 and τ is the fluorescence lifetime. The lifetime of the fluorophores can be measured by measuring the fluorescence decay after excited by a short pulse of excitation. The fluorescence decay is mono-exponential in uniform solvents. In complex systems, the decay is multi-exponential. [3, 22] Besides the fluorescence, several other pathways are possible for the decay of excited molecules such as intersystem crossing and quenching. All non-fluorescent pathways can be combined into single rate constant and denote by K(nr). The quantum yields can also be expressed in terms of rate constants and lifetime.

$$\Phi = \frac{\text{Photons emitted}}{\text{Photons Absorbed}} = \frac{\text{Kf}}{\text{Kf} + \text{Knf}} = \tau f/\tau_0$$

K(f) is the rate constant of fluorescence decay. τ_f is intrinsic lifetime. The measured lifetime (τ_o) can never be greater than an intrinsic lifetime. So the maximum value of Φ is unity. The fluorescence lifetime of probes has significant benefits over fluorescence intensity because the lifetime measurements are less sensitive to photobleaching objects than intensity. Lifetime can also be used as a probe to distinguish the fluorophores which have similar spectral features.[3, 21-24]

1.5 Quenching and Photobleaching

The terms photo-bleaching and quenching are associated with the effective reduction in the emission intensities of fluorochromes. The two terms can be distinguished that quenching is a reversible phenomenon and photo-bleaching is an irreversible process. Quenching is caused by the non-radiative relaxations that dramatically lower or completely eliminate the emission. Most often, quenching reduces the excited state lifetime and quantum yield of fluorochrome. The deactivation of excited state fluorochromes as a result of collision with nonfluorescent molecules is common examples of quenching. Oxygen, amines, halogens, and electron deficient organic molecules are common collisional quenching agents. Spin-orbit coupling, electron transfer, and intersystem crossing are the common mechanisms of collisional (dynamic)

quenching. On the other hand, static quenching arises from the formation of a non-fluorescent reversible complex between fluorophore and quencher in the ground state. Dipolar resonance energy transfer is another mean of static quenching. [25, 26]

Photo-bleaching is a phenomenon in which a fluorophore undergo a covalent modification and photon induces chemical damage and losses fluorescing ability permanently. The irreversible covalent modification arises when a fluorophore interacts with another molecule upon the transition from excited singlet state to the excited triplet state. Some fluorophores bleach quickly and others take a long time. Photodynamic is a photobleaching event that involves the interaction of the fluorophore with oxygen and light. This reaction permanently destroys the fluorescence and produce free radical and singlet oxygen species that have the ability to modify the chemistry of other molecules in living cells. The extent of photobleaching due to photodynamic is a function of the concentration of molecular oxygen and the distance between interacting elements. By reducing the exposure time or lowering the energy of excitation the photo-bleaching can be reduced. [26, 27]

1.6 Solvent Effects on Fluorescence

Various micro-environmental factors affect the fluorescence emissions that include interactions of solvent molecules and fluorophores, pH, solvent polarity, temperature and concentration of fluorescent materials. The extent to which these variables affect varies from one fluorophore to another. A fluorophore at excited state can be considered as another molecule relative to the molecule in the ground state. Because they display different properties with regards to interactions with microenvironments. The dipole moment of solvent molecules surrounding the fluorophores interacts with the dipole moment of fluorophores in solution. The change of ground state molecule to the excited state molecules induces the change in dipole moment. And thus induce a rearrangement of surrounding solvent molecules. The solvent molecules stabilize the fluorochrome by lowering the energy of excited states through reorientation around the excited fluorophore termed as solvent relaxation. And induce a red shift in fluorescence emission by reducing the energy difference between excited and ground states. Increasing the solvent polarity enhances the solvent effect on the excited state and can enhance the signal intensity and display large fluorescence Stoke shifts that offer the high degree of selectivity and

sensitivity for sensing applications. Thus the polarity of the fluorophore is a parameter to determine the sensitivity of the excited state to the solvent effect.[3, 11, 28]

1.7 Resonance Energy Transfer (RET)

RET is a process in which an excited state fluorophore as a donor, nonradiatively transfers its excitation energy to the acceptor (a neighboring chromophore) through long-range dipole-dipole interaction. The donor fluorochrome can be assumed as an oscillating dipole that transfers its energy to a chromophore of a similar dipole at a particular resonance frequency like the behavior of coupled oscillators. The RET occurs when the emission spectrum of donor overlaps with the absorption spectrum of the acceptor. In the processes of RET, the emission of the donor is quenched in the presence of acceptor and the emission of acceptor increases. However, the process does not involve the subsequent absorption of photon by acceptor with the emission of a photon by the donor. The efficiency of RET varies with the degree of spectral overlap and the distance between the donor and acceptor. RET can be detected by monitoring the changes in emission of acceptor with exciting at the wavelength corresponding to the absorption maxima of the donor. The efficiency of RET (E_T) and rate of energy transfer (K_T) are related to lifetime of donor in the presence and absence of acceptor that can be expressed as:

$$K_T = \left(\frac{1}{\tau_D}\right).\left(\frac{R_o}{r}\right)^6$$

R_o is the critical Forster distance *i.e.* the separation radius between donor and acceptor where the energy transfer probability equals the donor decay rate in the absence of the acceptor. τ_D is the lifetime of the donor in the absence of acceptor. The energy transfer efficiency is related to the separation distance between donor and acceptor

$$\mathrm{r} = R_o[(1/E_T) - 1]^{1/6}$$

Where $E_T = 1 - (t_{DA}/t_D)$. Thus r and E_T can be determined by measuring the lifetime of the donor in the presence and absence of acceptor. The Fluorescence resonance energy transfer (FRET) based systems show high selectivity and sensitivity for the sensing applications. [29-32]

1.8 Instrumentation

Different types of fluorescence detection instruments have been designed, each with the definite

experimental method. However, the fluorescence detection instruments possess four basic components

a. Excitation source

b. Fluorophore Chamber

c. Filter

d. Detector

In our experiments, we used Fluormax-4 spectrofluorimeter installed at the Biosensor Lab (**Fig. 1.2**). The instrument is equipped with Xenon lamp as radiation source that is focused on the entrance slit of excitation monochromator with an elliptical mirror. The slits are bilateral that can be continuously adjustable from the computer. The excitation monochromator ensures the image of the light diffracted from the grating fits via the slit. The instrument is equipped with a reference detector that monitors the intensity as a function of time and wavelength before the excitation light reaches the sample. For this purpose, photodiode detectors are commonly used. A sample chamber is allowed to use accessories. The features associated with the excitation monochromator are also incorporated into the emission monochromator. The electronics of the emission detector employ the photon counting that concentrates on signals originated from fluorescence emission. The fluorescence measurements are controlled by FluorEssence™ Software from a computer.[11, 33]

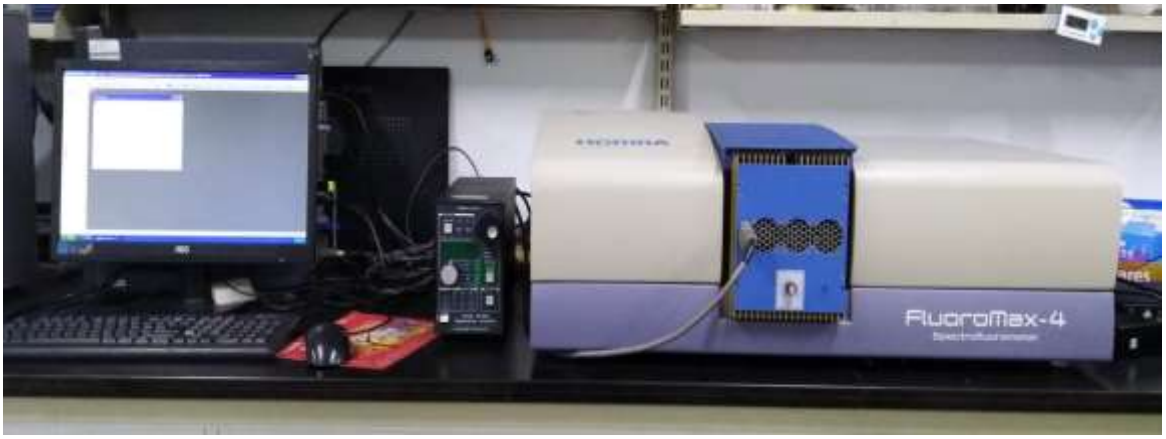

Fig. 1.2: Fluoromax-4 Spectrofluorometer used for fluorescence studies installed at Biosensor lab.

1.9 Fluorescent Probes

A fluorescent probe is a fluorophore designed to respond a specific analyte or localize within a

specific region of the biological specimen. In general, fluorescent probes are intrinsic or extrinsic. Intrinsic fluorophores occur naturally such as porphyrins, neurotransmitters, and aromatic amino acids etc. Extrinsic fluorophores are synthetic dyes or modified biochemicals that induce fluorescence with specific spectral properties. Thus fluorescent probes can be further divided into organic dyes, metal-ligand complexes, biological fluorophores, and quantum dots. Millennia was used for the first time in 1990 as a biological fluorophore. Since then various proteins have been designed and used commonly for biological research. However, the use of fluorescent proteins is time-consuming and can induce toxicity if generate reactive oxygen species. Biological fluorophores normally do not reveal the photostability and sensitivity as offered by synthetic fluorescent dyes. [34]

Quantum dots provide the tight control over the spectral features. They were developed in the 1980s and since increasingly used in fluorescence base applications. The quantum dots were reported to be more stable. And they can be used for different biological applications. However, the cell toxicity in response to the breakdown of particles was reported. The quantum confinement effect and cross-linked enhanced emission effects are common PL mechanisms described for quantum dots. [34, 35]

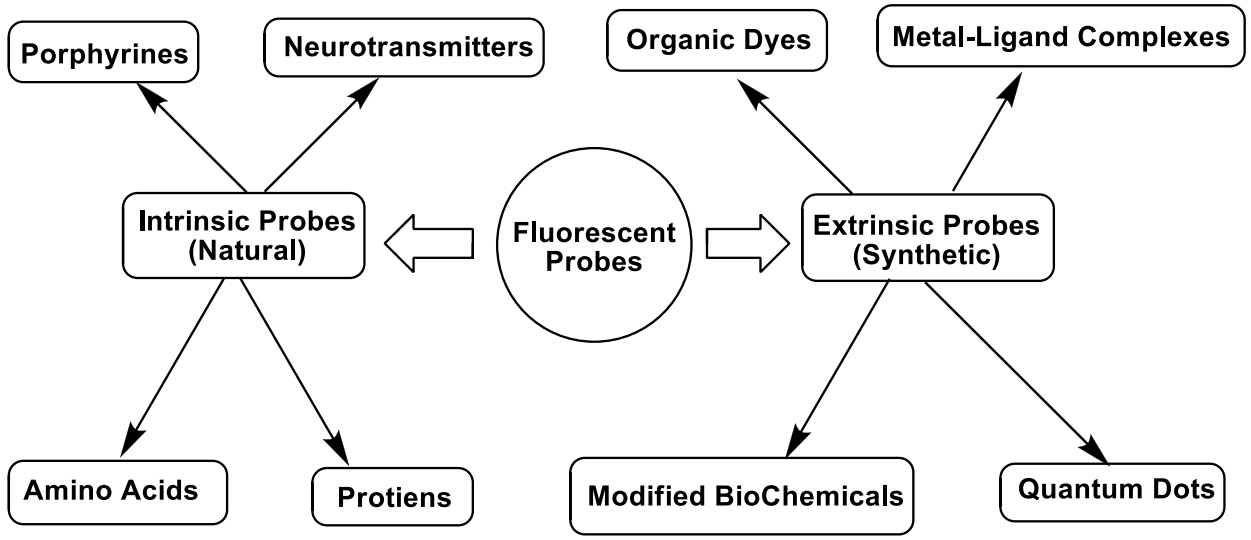

Scheme 1.1 Classifications of fluorescent probes

Fluorescein was the first fluorescent compound used in research. Since then organic dyes and metal-ligand complexes are widely used fluorescent probes. The small size of these probes has benefits over biological probes for bioconjugation techniques. They can be cross-linked with

macromolecules without interfering biological functions. A wide variety of dyes with desirable absorption and emission behaviors are commercially available for different applications. These probes provide unlimited opportunities for monitoring the simple and complex biological and environmental systems to make the world safer, healthy and cleaner. [10, 19, 20, 23, 36-38]

1.10 Small Molecular Organic Fluorochromes

Due to the fluorescence abilities small molecular probes has prime importance as sensing and labeling elements in bio-analytical techniques such as disease diagnosis, environmental monitoring, macromolecular (protein, DNA, RNA etc) analysis, control self-assembly and particles aggregation. The molecular probes based fluorescence techniques offer high sensitivity and selectivity, simple operation and cost-effectiveness. The simplicity of these techniques is due to the use of small changes in fluorescence signals. Most of the small molecular probes exhibit the concentration quenching or fluorescence turn-on based on which a number of sensing strategies have been developed. Condensed polycyclic aromatic hydrocarbons (PAHs) are the organic fluorochromes of prime importance. They display excellent thermal stability, high quantum yields, and longer lifetime. Pyrene, perylene, anthracene, coronene, and benzo[ghi]perylene etc are commonly used PAHs for probing application. The structures and properties of these probes can be fine-tuned in a controlled manner through derivatization. However, they often exhibit the disadvantages of being water-soluble and easy to gather in organic solvents. This limits their own application.

1.11 Aggregation-induced emission

The Aggregation-Induced Emission (AIE) effect, a groundbreaking phenomenon in the field of luminescent materials, was discovered by Professor Ben Zhong Tang and his research group. This discovery fundamentally altered our understanding of light emission in molecular aggregates compared to traditional chromophores.

The mechanism behind the AIE effect is based on the restriction of intramolecular rotation (RIR). In traditional fluorescent dyes, when the dye molecules aggregate, their fluorescence is usually quenched due to non-radiative energy transfer between the molecules. However, in AIE dyes, when the molecules aggregate, their rotation is restricted, preventing non-radiative energy transfer and allowing fluorescence to be maintained or even enhanced. This mechanism can be

achieved by introducing rigid structural units, such as benzene rings or triazine rings, into the dye molecules.

AIE luminogens have found applications in various high-tech domains, serving as chemosensors, bioprobes, and solid-state emitters. When employed as chemosensors, AIE luminogens are invaluable for detecting volatile organic compounds (VOCs), addressing hygienic and environmental concerns. As bioprobes, these luminogens serve as turn-on biosensors, emitting light upon binding to biological molecules, offering advantages over their turn-off counterparts. To enhance their versatility, hydrophilic functional groups, including hydroxyl, amino, ammonium, sulfonate, and boronate, are incorporated into the AIE dye structures, making them water-soluble. Additionally, AIE luminogens exhibit exceptional performance as solid-state emitters, making them integral to light-emitting devices.

One of the most distinguishing features of AIE systems is their unique response to concentration. In contrast to traditional chromophores, which typically exhibit strong fluorescence in dilute solutions but become non-emissive in aggregated states due to excimer or exciplex formation, AIE luminogens display precisely the opposite behavior. AIE luminogens are non-emissive in solution but become highly emissive in the aggregated state, owing to the RIR mechanism. This extraordinary characteristic endows AIE luminogens with remarkable sensitivity to changes in concentration, rendering them ideal for use as concentration sensors.[39-42]

1.12 Recent Applications based on Fluorescent Probes: A Brief Review

Over the last decades, luminogenic materials have been utilized extensively for high tech innovations. Various new luminogenic materials were developed through mechanistic synthetic strategies that offered useful applications. [43-56] Number of fluorochromes displayed excellent PDT effect and utilized for photodynamic therapy. [57-60]

Professor Enzo and his team developed a novel near-infrared fluorescence dye targeted at the gastrin-releasing peptide receptor (GRPR) for image-guided surgery of prostate cancer. The article provides detailed information on the synthesis of the fluorescent dye, in vitro experimental results, and in vivo imaging results in a mouse model. The results demonstrate that the fluorescent dye can effectively identify prostate cancer tissue and improve the identification rate of malignant tissue during surgery. The authors further discuss the potential

applications of this technology in prostate cancer surgery, as well as its limitations and future research directions. Although further research and validation are needed, this technology shows great promise and deserves further attention and investigation.[61]

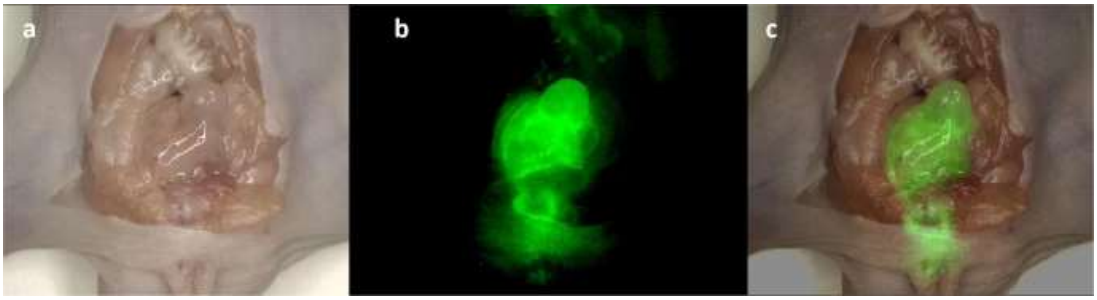

Fig. 1.3 Novel Gastrin-Releasing Peptide ReceptorTargeted Near-Infrared Fluorescence Dye for Image-Guided Surgery of Prostate Cancer developed by E.Terreno et, al[61]

Tang,B.Z. et al propose an innovative approach to address challenges in deep tissue imaging by developing a novel aggregation-induced emission (AIE) luminescent material with unique near-infrared ii(NIR-II) excitation and near-infrared i(NIR-I) emission properties. This paper describes the characteristics of AIE fluorescent substances, including their high fluorescence quantum yield and strong fluorescence emission in the aggregation state, and their application in deep tissue imaging. The paper also introduces the method of ultra deep in vivo two-photon microscopy imaging using NIR II excitation and NIR I emission, and discusses the application of AIE fluorescent substances in this imaging technique. In addition, the paper describes the potential applications of AIE fluorescent substances in other biomedical applications, such as fluorescence probes and fluorescence sensors. Overall, the literature provides detailed information on the use of AIE fluorescent substances in deep tissue imaging and explores its potential applications in the biomedical field.[62]

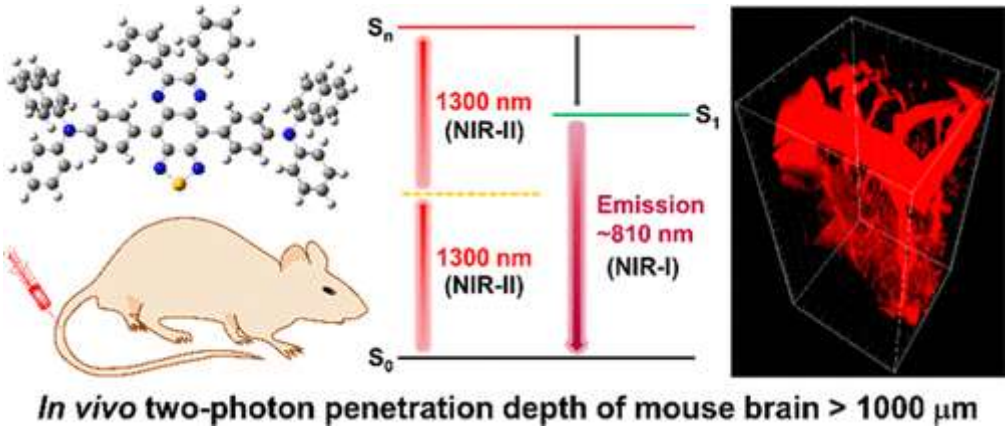

Fig.1.4 Aggregation-Induced Emission Luminogen with Near-Infrared-II Excitation and NearInfrared-I Emission for Ultradeep Intravital Two-Photon Microscopy by Tang. Et.al. [62]

F. Zhang et.al introduce a new type of chemiluminescence sensor that operates in the second near-infrared window (NIR-II CLS) with a deep penetration depth. The sensor can detect local inflammation in mice with a 4.5-fold higher signal-to-noise ratio than that under the NIR-II fluorescence modality. To achieve this goal, the researchers engineered the cascade CRET and FRET processes and designed dyes with excellent energy match and large Stokes shift characteristics to efficiently transfer chemical energy. The sensor provides a promising perspective and strategy for constructing probes with extended emission wavelength in classical CL for higher contrast imaging and offers the possibility of sensing various analytes by changing the chemiluminescent substrate in the future. Although the sensitivity and brightness of the current NIR-II CLS are still not ideal, the present results indicate that the NIR-II CLS is promising for NIR-II CL in vivo imaging with higher SNR compared to the NIR-II fluorescence signals in the same system.[10]

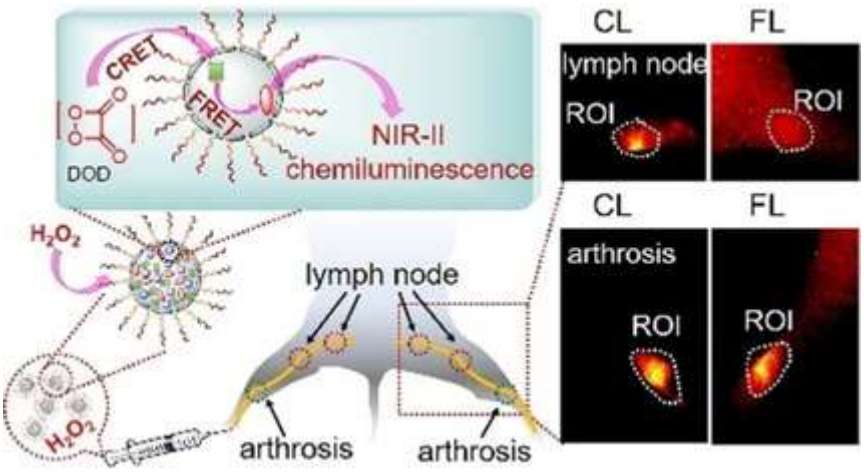

Fig. 1.5 An NIR-II chemiluminescent molecular sensor for high-contrast imaging of inflammation in vivo developed by Zhang et. al.[10]

Fluorescent probes play a crucial role not only in vivo but also in vitro.Li et al. have achieved the construction of a highly efficient and sensitive sensor array by conducting an in-depth investigation into the emission transition of the perylene probe monomer-radical group. This sensor array exhibits remarkable selectivity and sensitivity towards diverse metal ions and drinking water samples, while offering the significant advantages of real-time monitoring and multi-target detection capabilities. Furthermore, the research delves into the differentiation of various metal ions and drinking water samples, thereby expanding the prospects for the practical implementation of this sensor array. This pioneering study not only introduces novel concepts and methodologies for the advancement of water quality assessment, characterized by enhanced efficiency, precision, and real-time monitoring, but also furnishes valuable insights for the design and fabrication of fluorescent sensor arrays. It is anticipated that this technology will find extensive applications in the realms of environmental monitoring and ensuring the safety of drinking water in the foreseeable future.[20]

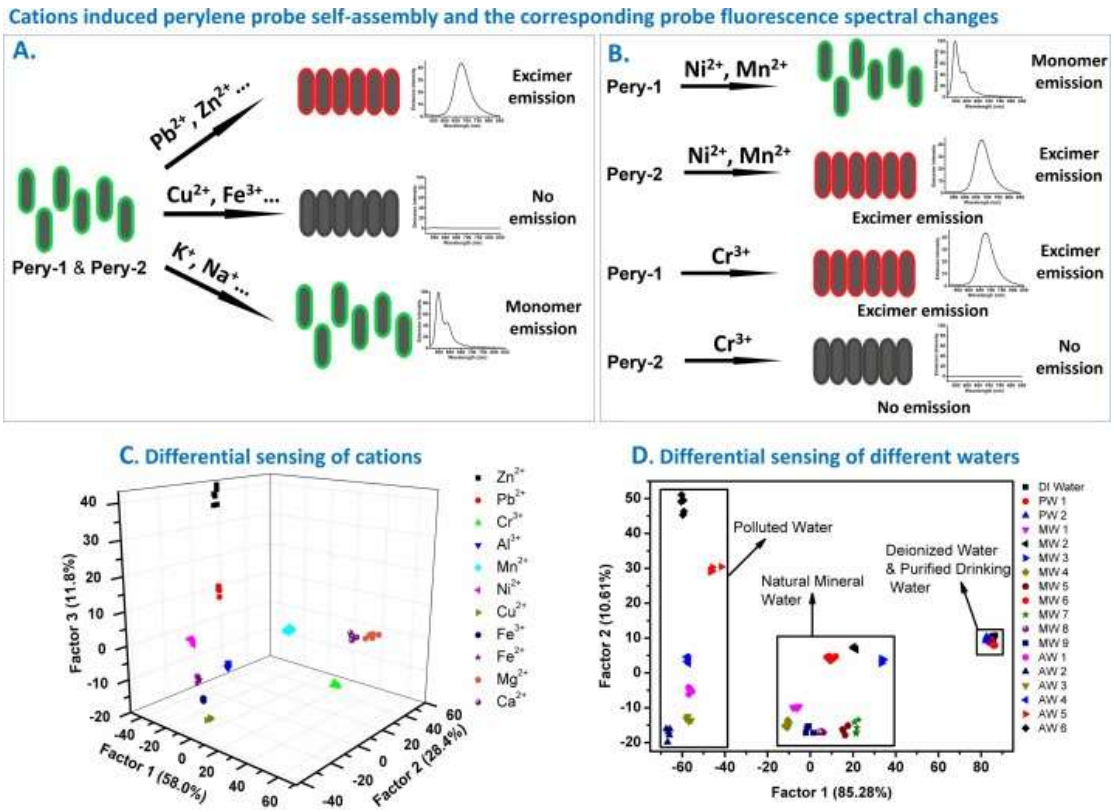

Fig 1.6 Fluorescent sensor arrays based on peroxyacetic acid probe monomer-excimer emission transition for efficient differential sensing of metal ions and drinking water discovered by Li et al.[20]

Dey et al. successfully employed self-assembled nanomaterials based on naphthalene monoimide in an aqueous medium for the multimodal detection of picric acid, an organic explosive compound. The research begins with the synthesis of self-assembled naphthalene monoimide nanomaterials, followed by an in-depth exploration of their optical properties, including absorption and fluorescence spectra, as well as their sensitivity and selectivity in detecting picric acid.The results demonstrate that these self-assembled naphthalene monoimide nanomaterials exhibit a high level of selectivity and sensitivity for picric acid. Utilizing different detection modes, such as absorption spectroscopy, fluorescence spectroscopy, and fluorescence microscopy imaging, these nanomaterials prove effective in detecting picric acid. This multimodal detection approach holds promise for applications in explosive detection and offers a potential, efficient, and sensitive solution for the detection of organic explosives.[63]

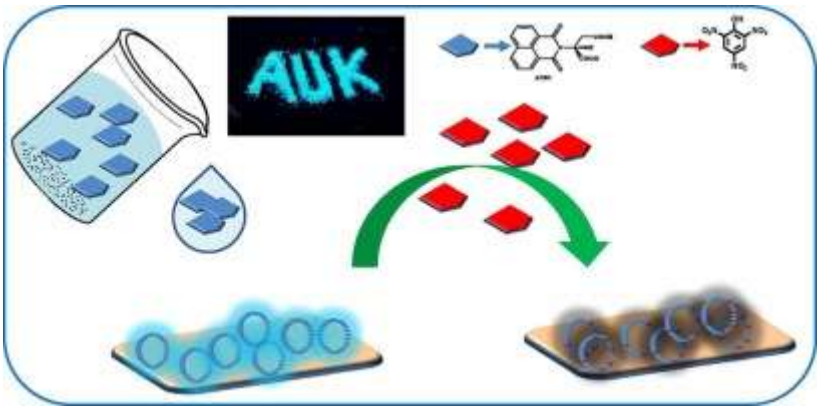

Fig.1.7 Self-assembled nanomaterials of naphthalene monoimide in aqueous medium for multimodal detection of picric acid developed by Dey et al.[63]

Chapter 2 Development of a PDI-based fluorescent probe for sensitive detection of nitric oxide

Abstract

Nitric oxide (NO) is considered a gas signal molecule because its important role in physiology and pathology. Therefore, the development of high- sensitive and selective fluorescent probes has become significant for NO detection. In the current study, a new type of NO sensing fluorescent probe was synthesized and compared with other probes, showing lower detection limit and excellent response time. The probe was studied in detail and used for cell imaging. Importantly, the probe was embedded into thin film for sensitive detection of NO in air.

Key words: Nitric oxide; fluorescent probes; cell imaging

2.1 Introduction

Nowadays, nitric oxide (NO) is considered an important gas signal molecule in living organisms. Basically, it is produced through the catalysis of nitric oxide synthase in cells, using L-arginine, NADPH and oxygen.[64] It plays important physiological functions in several systems (such as cardiovascular, immune and central nervous system, etc…).[64, 65] Different studies showed that NO is mainly produced by intracellular mitochondria and participates in the breath regulation and apoptosis by binding to the hemoglobin group of the cytochrome c oxidase and regulating pH in mitochondria.[66-69] Moreover, NO is able to penetrate the mitochondrial membrane and spread freely into lysosomes to regulate their functions, including autophagy.[70-73] However, under non-physiological conditions, NO can be overexpressed, leading to the outbreak of peroxy-nitrite (ONOO-), its downstream oxidation product.[74-79] ONOO- can oxidize various biological macromolecules at mitochondria and lysosome level, resulting in function loss, and contributing to the onset of a series of diseases, including cancer, diabetes, high blood pressure, Alzheimer's disease, and lysozyme storage disease.[78, 80-94] Low and moderate levels of nitric oxide may cause irritation for eyes, nose, throat and lungs, and may cause coughing or shortness of breath, tiredness, and nausea.[67, 68, 75, 79, 95-105] It may also cause fluid accumulation in the lungs 1 or 2 days after exposure to low temperatures.

Breathing high levels of nitrogen oxides may cause short burn, dyspnea, laryngeal tissue and upper respiratory tract congestion, tissue hypoxia, fluid accumulation in the lungs and death. On this basis, it is clear how relevant the development of NO sensors can be.[71, 76, 106-111] In the past decade, in order to track intracellular NO changes, different fluorescent probes have been developed. Among these, NO fluorescent probes based on o-phenylenediamine reaction groups were first developed, and then widely used in commercialization.[70, 112-119] The mechanism of action of this kind of probe consists in the reaction between o-phenylenediamine group and NO, under aerobic conditions to form a benzotriazole group, which inhibits the photoinduced electron transfer quenching process (PET) of the probe molecule and leads to the fluorescence "off-on" response. Despite these probes have been widely used in biological systems, there are still some limitations, such as the interference by intracellular species as dehydroascorbic acid (DHA)/ascorbic acid (AA) and the relatively long fluorescence response time (usually more than 5 minutes).

Condensed polycyclic aromatic hydrocarbons (PAHs) are organic fluorochromes of primary importance. They display excellent thermal stability, high quantum yields, and long fluorescence lifetime. Pyrene, perylene, anthracene, coronene and benzo[ghi]perylene are commonly used PAHs for probing application. The structures and properties of these probes can be fine-tuned in a controlled manner through derivatization. Perylene diamides (PDIs) are excellent choices to bring the structural diversity and fine-tuning of photophysical properties. PDIs are extensively used as pigments, organic field effect transistors, solar cells, biosensors and fluorescent labels, because they exhibit a large optical absorption in the Near InfraRed (NIR) region. [99, 100] Moreover, they emit fluorescence with almost unity of quantum yield and reflect significant charge transport properties. In this work, the probe **N-PBI (Fig.1a)**, hydroxylamine substituted at bay site, was designed and synthesized for sensing NO.

2.2 Experiment

2.2.1 Materials and Instrumentation

Unless otherwise noted, materials were obtained from Sigma (Shanghai, China) and used without further purification. CaH was distilled from dichloromethane. Toluene was purified by

refluxing sodium in nitrogen for several hours and then distilled to remove trace water. Nitric acid was purchased by Beijing Chemical Plant (Beijing, China). Nitric oxide was provided by sodium nitroprusside and $ONOO^-$ was prepared according to the literature method.[102] Deionized water was obtained by Milli-Q water purification system (Millipore, Shanghai, China) with an electrical conductivity of 18.2 s/m. Using tetramethylsilane (TMS) as the internal standard, ^1H and ^{13}C NMR spectra were recorded on Bruker Avance III spectrometer at 500 MHz frequency. The mass spectrometry was recorded on the Brook Electron spray Ionization Mass Spectrometer (ESI-MS). The UV-Vis absorption spectrum was collected by CARY50 biological spectrophotometer (Varian Inc., CA, USA). The fluorescence spectrum was measured on Fluoromax-4 fluorescence spectrophotometer (HoribaJobinYvon Inc., USA). The spectrum was recorded at 25 °C with excitation and emission slits of 2 nm. The MTS-based test data were collected using a 96-well plate (Sang on Biotech, China, Shanghai) on the SynergyH1 enzyme labeling instrument (BioTek, USA). The CLSM image of the confocal microscope was from Nikon ECLIPSETi (Japan).

2.2.2 Synthesis of probe N-PBI

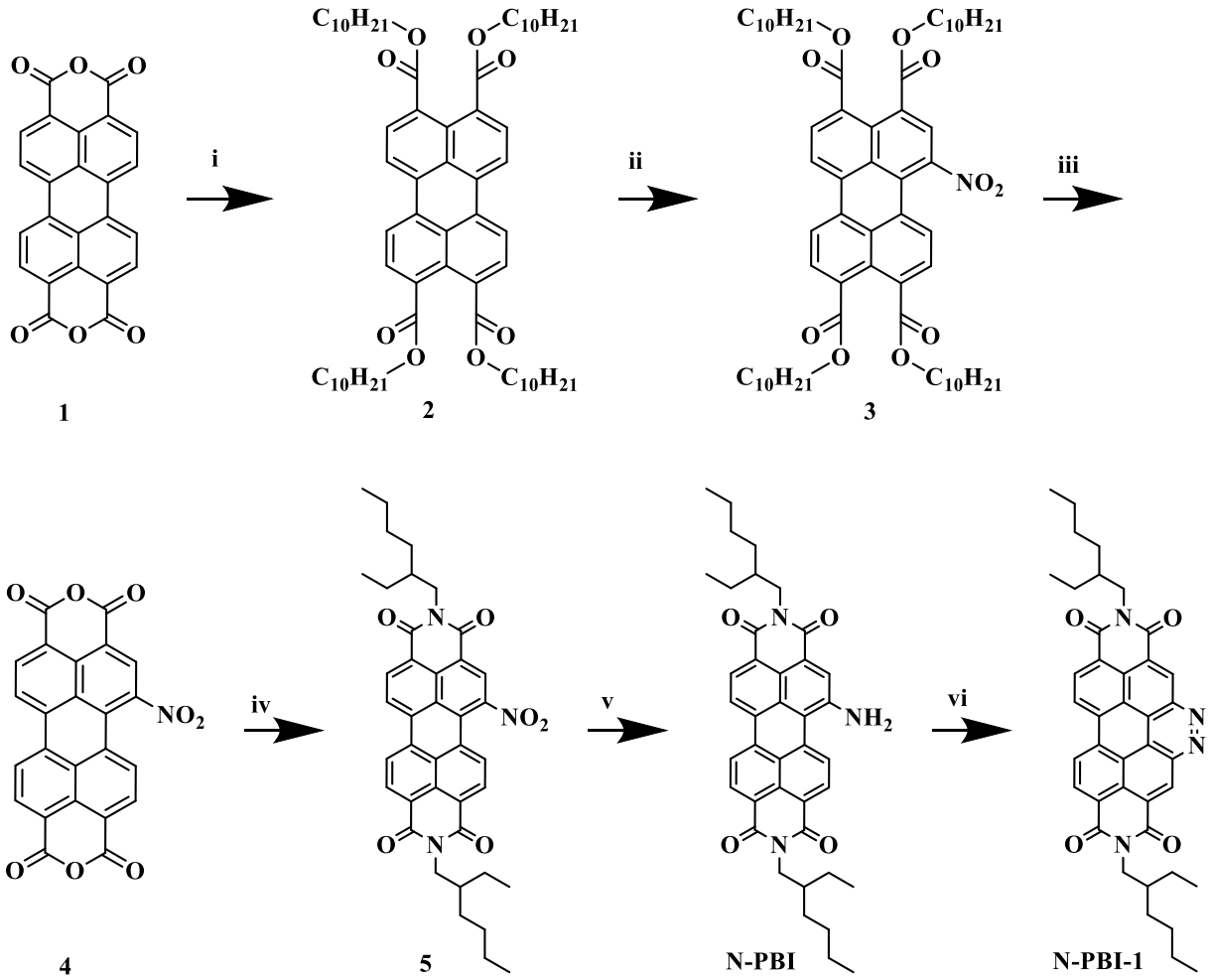

Scheme 2.1 synthesis of N-PBI (i) KOH ,70 °C, water, 0.5 h. Aliquat336, KI, 1-bromodecane, reflux, 12h. (ii) $(NH_4)_2Ce(NO_3)_6$, HNO3 in DCM 20 ℃ ,1 hour. (iii)TsOH in toluene, reflux, 24h. (iv) 2-ethylhexylamine in propionic acid, refluxed, 6 h. (v) NH_2-NH_2,Pd/C in THF, reflux, 12h. (vi)HCl, $NaNO_2$ in THF, RT, 15min.

2.2.3 Synthesis of tetrakis(decyl) perylene-3,4,9,10-tetracarboxylate(2) [120]

Tetracarboxylic acid dianhydride (2.5 mmol, 1 equivalent) was dissolved in 30mL KOH (13.76 mmol 5.4 equivalents) aqueous solution and stirred at 70 °C for 0.5 h. The solution was filtered and the pH was adjusted to a value between 8 and 9 with a 10% HCl solution. Then Aliquat336 (0.9 mmol, 0.4 equivalents) and KI (1.4 mmol, 0.6 equivalents) were added to the above mixing system and stir vigorously for 10 minutes. 1-bromodecane (15.3 mmol, 6 equivalents) was

added to the reaction mixture. The obtained solution was brought to reflux and was stirred for 12 hours until the red oil floats on top and the rest of the solution becomes clear. 10mL was then poured into the mixture, filtered to remove the unreacted part, and the residue was washed with chloroform. The organic phase was collected and washed twice with 15% sodium chloride solution, dried with sodium sulfate and concentrated in vacuo to obtain a viscous concentrate solution. The desired compound was precipitated by addition of methanol, filtered, dried under vacuum and was used for the next step without further purification.

2.2.4 Synthesis of tetrakis(decyl) 1-nitroperylene-3,4,9,10-tetracarboxylate (3)

Sodium nitrite (0.7 mmol, 1 equivalent) was added to the dichloromethane (5mL) solution of product 2 (0.7 mmol, 1 equivalent) at 0 ℃. 69% HNO_3 (3.42 mmol, 5 equivalents, 10% DCM) was added to thestirred suspension. The mixture was stirred at 0 ℃ for 1 hour. The reaction mixture was poured into water, extracted with DCM (4×25mL), and washed with Brine. The organic phase was collected, dried with anhydrous Na_2SO_4 and concentrated in vacuo. The crude product was purified by direct phase silica chromatography with DCM: petroleum ether = 1: 1, and the yield was 91% as a blood red oil (658 mg, 0.64 mmol). ^{1}H NMR (500 MHz, Chloroform-*d*) δ 8.41 (dd, *J* = 10.8, 8.0 Hz, 2H), 8.01 (d, *J* = 7.9 Hz, 1H), 7.97 (d, *J* = 7.9 Hz, 1H), 4.32 (td, *J* = 7.1, 1.9 Hz, 8H), 1.81 – 1.76 (m, 8H), 1.45 – 1.41 (m, 8H), 1.35 (d, *J* = 8.4 Hz, 8H), 1.28 (d, *J* = 7.9 Hz, 41H), 0.88 (t, *J* = 6.8 Hz, 12H).

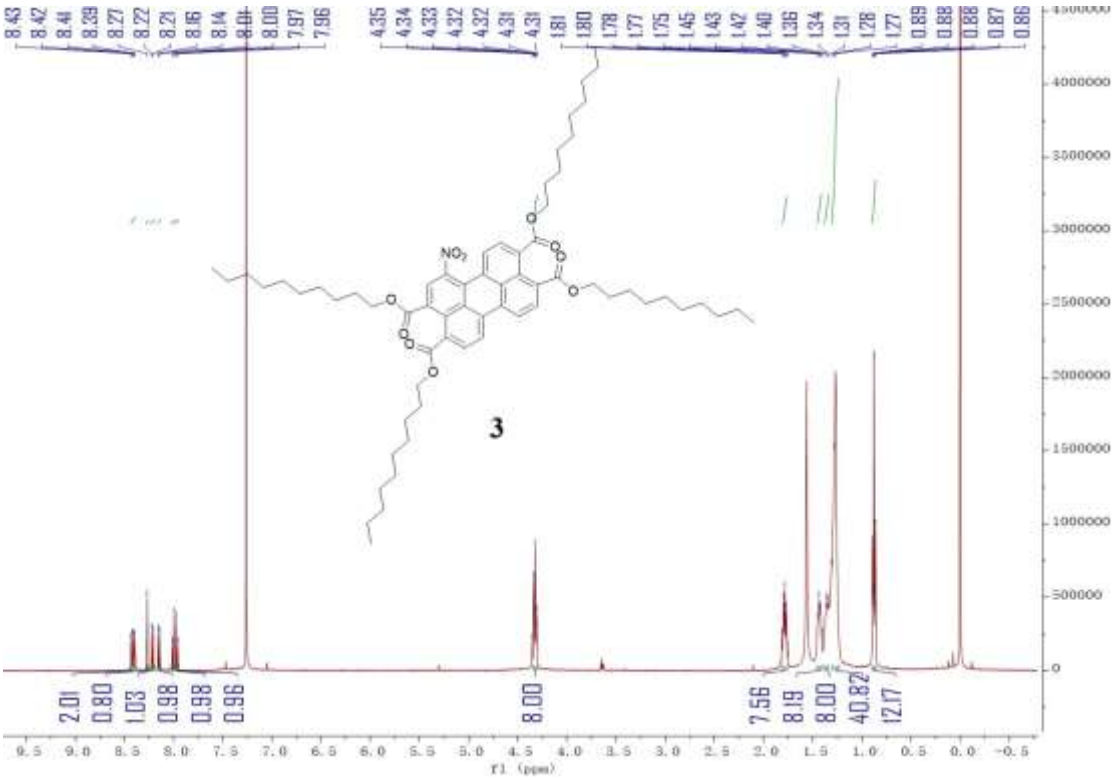

Fig 2.1 ^{1}H NMR of compound 3 in δ-Chloroform.

2.2.5 Synthesis of 5-nitroanthra[2,1,9-def:6,5,10-d'e'f'] diisochromene-1,3,8,10-tetraone(4) [121]

Compound 3 (1 mmol,1 equivalent) was dissolved in 15mL of dry toluene and was stirred until complete solubilization., Then, p-toluene sulfonic acid (4 mmol,4 equivalents) was added to the reaction mixture and the solution was refluxed for 24 h. A large amount of precipitation have been formed. The solution was cooled to room temperature, and the precipitate was filtered and washed with water and chloroform. The product was dried in vacuum to obtain a dark red solid with a yield of 89%(389 mg, 0.89 mmol). Proceed to the next reaction without characterization.

2.2.6 Synthesis of 2,9-bis(2-ethylhexyl)-5-nitroanthra[2,1,9-def:6,5,10-d'e'f']diisoquinoline-1,3,8,10(2H,9H)-tetraone(5)

Product 4 (218 mg, 0.5 mmol) was uniformly dispersed in 10mL propionic acid, followed by the addition of 2-ethylhexylamine (130 mg,1 mmol), and the reaction was refluxed for 6 h. After the reaction time, the above system was poured into 200mL distilled water and stirred for

0.5 h, then settled. The solution was filtered and the residue was washed 3 times with Brine. The crude product was dried in a vacuum oven and purified by direct phase silica chromatography with dichloromethane. The fractions containing the desired product were collected and evaporated to obtain a red powder (264 mg, 0.4mmol) with a yield of 85%.^{1}H NMR (500 MHz, Chloroform-*d*) δ 8.81 (d, *J* = 8.0 Hz, 1H), 8.77 – 8.70 (m, 4H), 4.20 – 4.12 (m, 4H), 1.96 (t, *J* = 6.7 Hz, 2H), 1.40 (dd, *J* = 12.7, 6.0 Hz, 9H), 1.35 – 1.27 (m, 10H), 1.25 (s, 2H), 0.95 (t, *J* = 7.4 Hz, 6H), 0.90 (td, *J* = 7.0, 1.9 Hz, 7H).

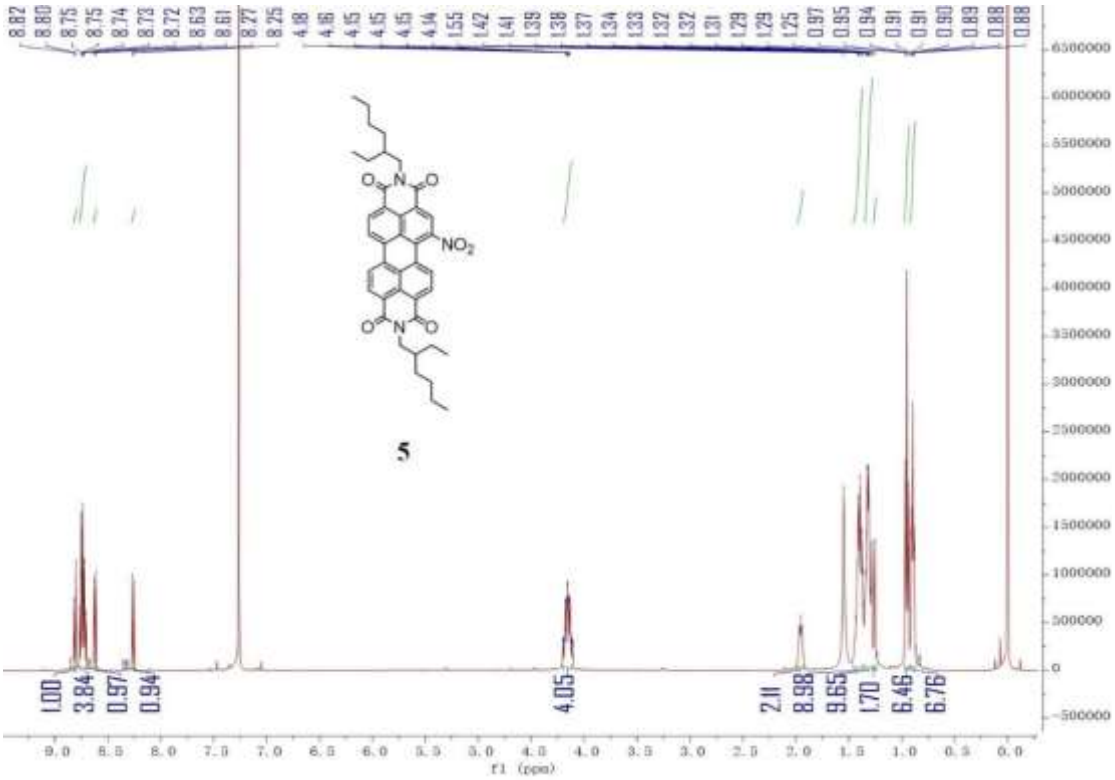

Fig 2.2 ^{1}H NMR of compound 5 in δ-Chloroform.

2.2.7 Synthesis of N-PBI

Hydrazine hydrate (100mg, 2mmol) and 1%mol palladium carbon were added to the tetrahydrofuran solution of compound 5 (216mg, 0.32mmol). The reaction was refluxed for 12 h. After the reaction stopped, the catalyst was filtered, the solvent was removed in vacuo, and the crude product was separated by column chromatography with DCM: MeOH=30:1 (containing 0.5% triethylamine) as eluent. The yield was 86% as a purple solid(173 mg, 0.28 mmol). ^{1}H NMR (500 MHz, DMSO-d_6) δ 8.30 (s, 2H), 8.02 (dd, *J* = 72.7, 39.9 Hz, 5H), 4.01 –

3.76 (m, 4H), 3.39 (s, 3H), 1.82 (s, 2H), 1.26 (s, 16H), 0.85 (s, 12H). ^{13}C NMR (126 MHz, DMSO) δ 163.72, 163.48, 142.34, 132.79, 132.05, 128.54, 128.21, 127.04, 126.31, 125.24, 122.91, 122.74, 122.61, 121.93, 121.57, 121.27, 120.95, 120.70, 119.01, 43.66, 37.57, 30.68, 28.61, 28.57, 24.01, 22.98, 14.42, 10.93. MS m/z: Calcd 645.34; found 645.3 $[M+H]^+$.

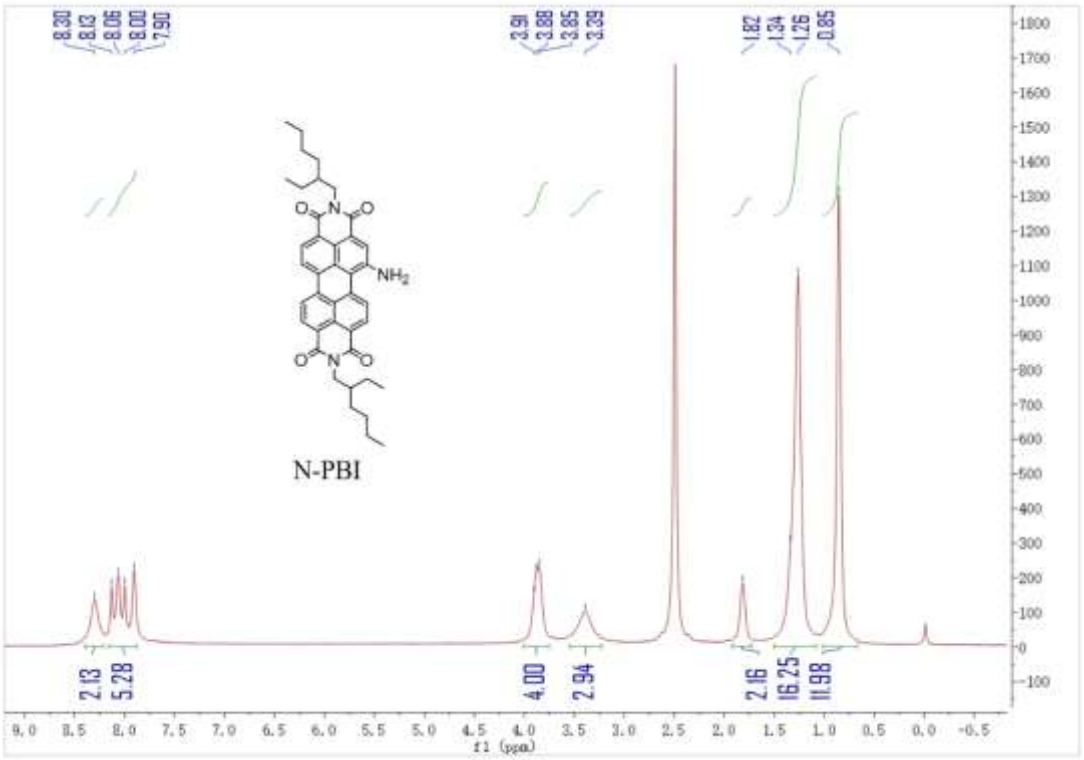

Fig 2.3 ^{1}H NMR of N-PBI in δ-DMSO

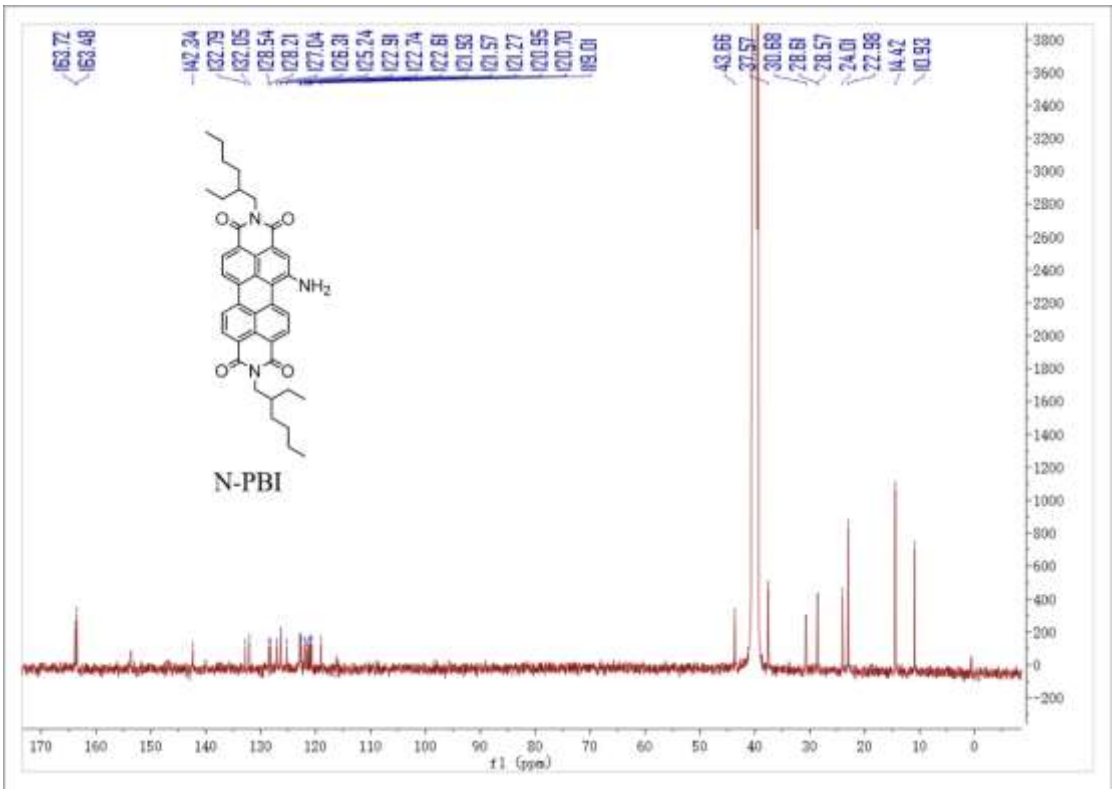

Fig 2.4 ^{13}C NMR of compound N-PBI in δ-DMSO.

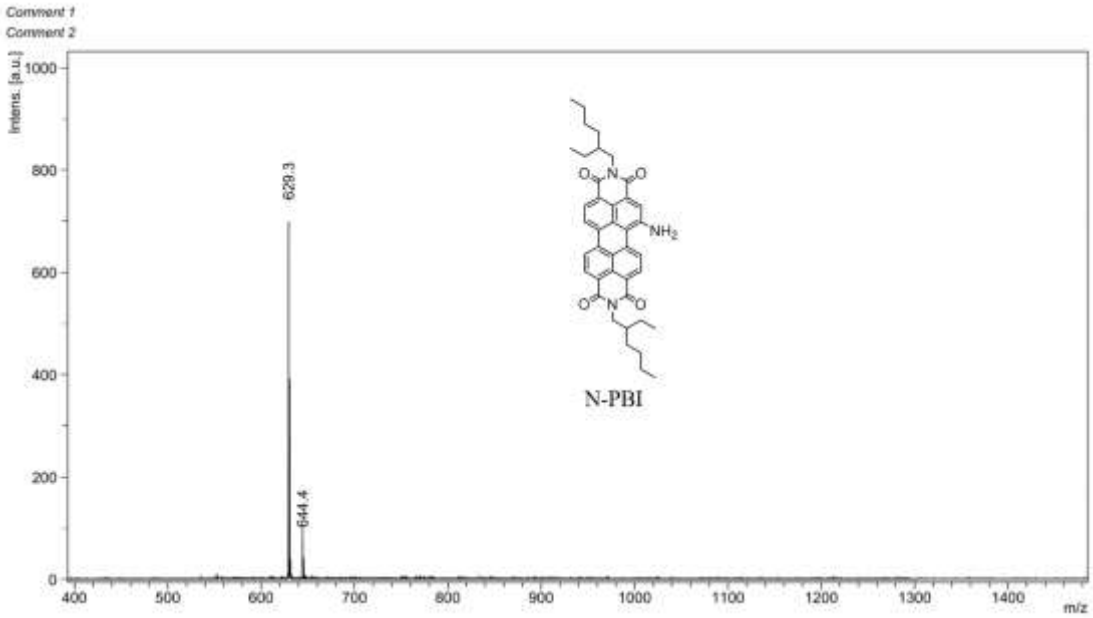

Fig 2.5 MS of N-PBI in THF.

2.2.8 Synthesis of N-PBI-1

1mL $NaNO_2$(0.3mmol 1.5 equivalent) solution was added to the tetrahydrofuran solution of N-

PBI (0.2mmol 1 equivalent). After full stirring, hydrochloric acid was added and reacted at room temperature for 15min. The reaction was poured into 150mL distilled water. After filtration, the residue was washed with saturated sodium chloride solution 3 times and dried to get orange powder with a yield of 97%.^{1}H NMR (400 MHz, Chloroform-d) δ 8.69 (d, J = 29.7 Hz, 6H), 4.16 (s, 4H), 1.97 (s, 2H), 1.37 (d, J = 32.4 Hz, 16H), 0.93 (d, J = 24.7 Hz, 12H). ^{13}C NMR (126 MHz, Chloroform-d) δ 163.35, 131.04, 122.75, 44.29, 37.94, 30.74, 29.71, 29.43, 28.68, 24.03, 23.10, 14.14, 10.61. MS m/z: Calcd 640.34; found 640.3 $[M+H]^{+}$.

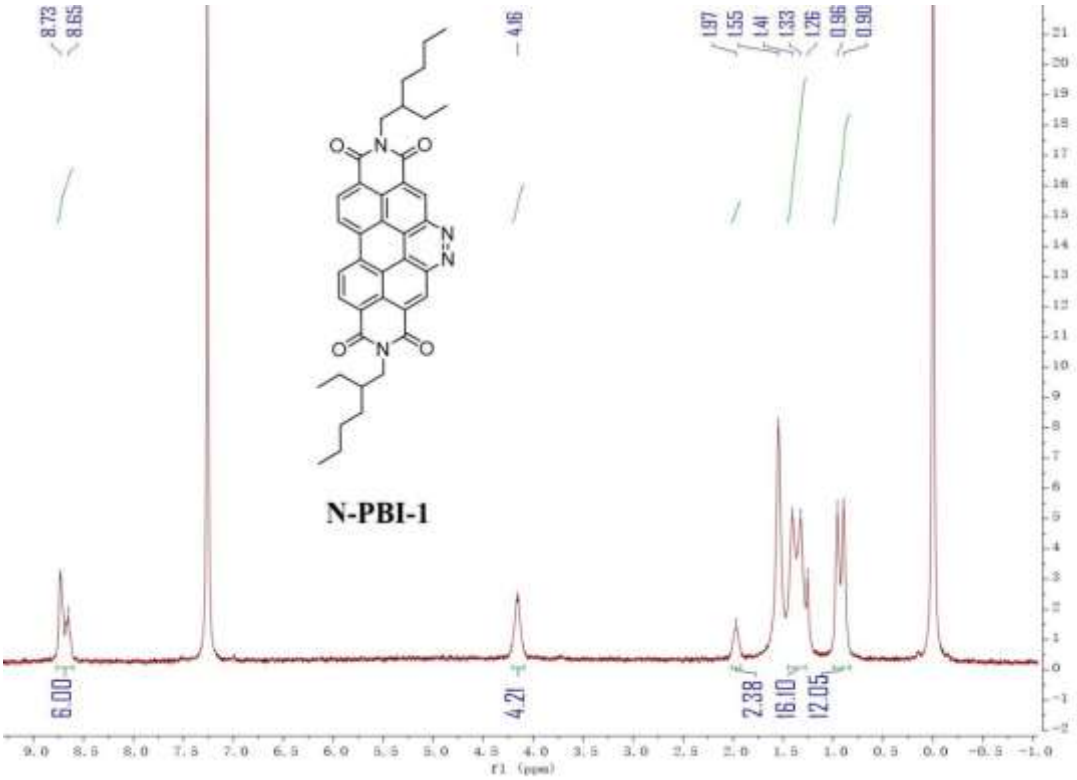

Fig 2.6 ^{1}H of N-PBI-1 in δ-Chloroform.

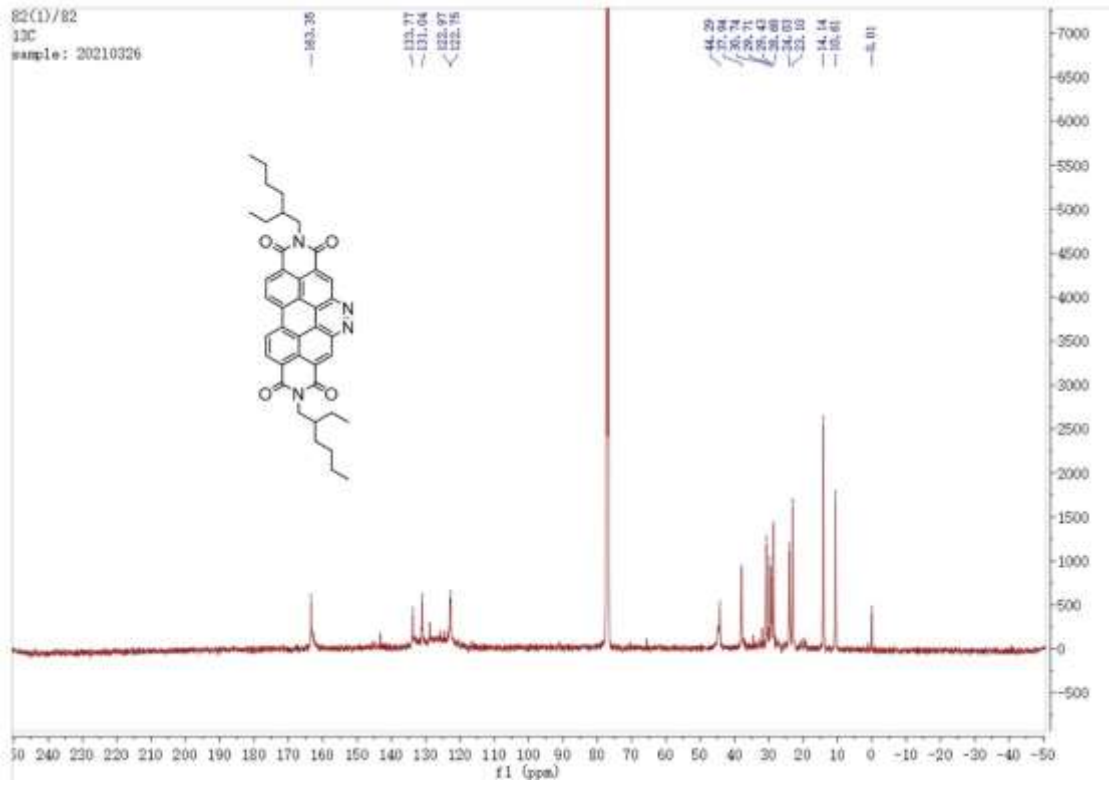

Fig 2.7 ^{13}C NMR of compound N-PBI-1 in δ-Chloroform.

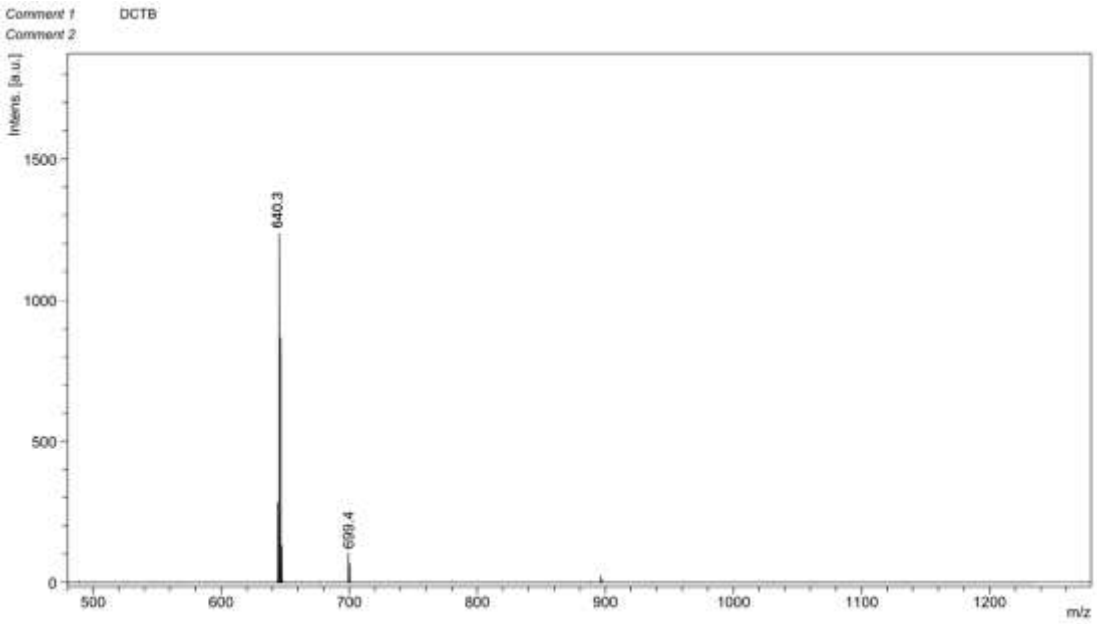

Fig 2.8 MS of N-PBI-1.

2.2.9 Synthesis of N-PBI thin film

10ml 184 silicone elastomer and 1ml 184 silicone elastomer curing agent were put into a 50ml

centrifuge tube, 1mM of N-PBI THF solution 500 μL was added and stirred fully with a glass rod. Air in the system was discharged through the vacuum pump. The mixture was evenly smeared on the slide and baked at 150 degrees overnight.

2.2.10 Optical studies

N-PBI mother liquor with 1.0mM concentration was prepared in THF and stored at 4 ℃. The 5 μL mother solution was diluted to 1 mL with solvent (PBS / THF=1:2), and the final concentration of 5 μM was obtained, which was used to determine the ultraviolet absorption spectrum and fluorescence emission spectrum. In the experiment, the slit width measured by fluorescence intensity was 2nm and the excitation wavelength was 490nm. All the spectra were tested at room temperature, and the interference solutions used for selective experiments were freshly prepared with secondary deionized water, in which the anions were sodium salts. Nitric oxide was provided by sodium nitroprusside (SNP). The in vitro test method was to add SNP (10 equivalent,100μ M) to 10 μ M N-PBI solution. After mixing evenly, the solution was placed in a self-made dark box and irradiated with white light. The solution was detected every two minutes, and the change of ultraviolet fluorescence spectrum was recorded.

2.2.11Cell experiment

4T1 cells were cultured in 1640 medium supplemented with 1% penicillin, streptomycin and L-glutamine and 10% fetal bovine serum. Cultured in 5%CO_2 constant 37°C incubator. The results of cytotoxicity were obtained by MTS experiment. For fluorescence imaging, the cells were cultured in a petri dish with 35mm glass at the bottom for 24 hours to grow on the wall. The PBS solution of the probe (the final concentration was 10 μM) was added to the petri dish and the cells were incubated at 37 ℃ for 2 hours.

2.3 Results and Discussion

Inspired by ours and other studies, amino-substituted molecules in the bay were designed to detect nitric oxide. The rationale of this approach is based on the expected different optical properties of the sensor (N-PBI) and its reaction product with NO (N-PBI-1)

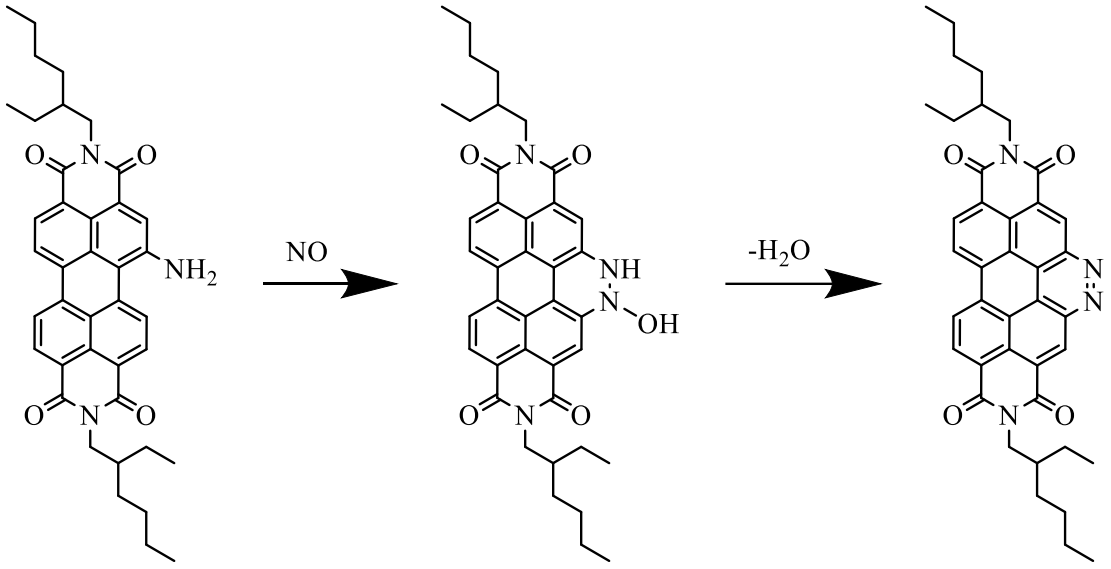

Scheme.2.2. Response mechanism of N-PBI to nitric oxide

The synthesis of N-PBI is shown in **Scheme 2.1**. First, the compound **1** as anhydride was opened under alkaline conditions, and then decane was added to improve the solubility in organic solvents. After that, compound **2** was nitrified by nitric acid and ceric ammonium nitrate under mild conditions. This step allowed to get the mono-nitro derivative only with high yield. compound **4** was obtained by removing alkyl chain with p-toluene sulfonic acid in toluene. In propionic acid, compound **4** was reacted with 2-ethylhexane to get compound **5**. Finally, the amino group was obtained by traditional palladium carbon and reducing agent. **Figs. 2.1-2.8** show the NMR/MS characterization of the products.

When compared with the parent PDI, the absorption spectrum of N-PBI showed a significant red shift of 66 nm (**Fig. 2.9b**). This is because the amino group at the bay site acts as an electron donor which formed a D-π-A structure with the acceptor at the imide site. When nitric oxide reacts with N-PBI, the absorption spectrum of the resulting compound N-PBI-1 displayed an absorption at 475 nm, which was almost the same observed for PDI (**Fig. 2.9b**). The spectra reported in **Fig. 2.9b** highlight the presence of a common absorption at 510 nm for the three species that is attributable to the main conjugate ring.

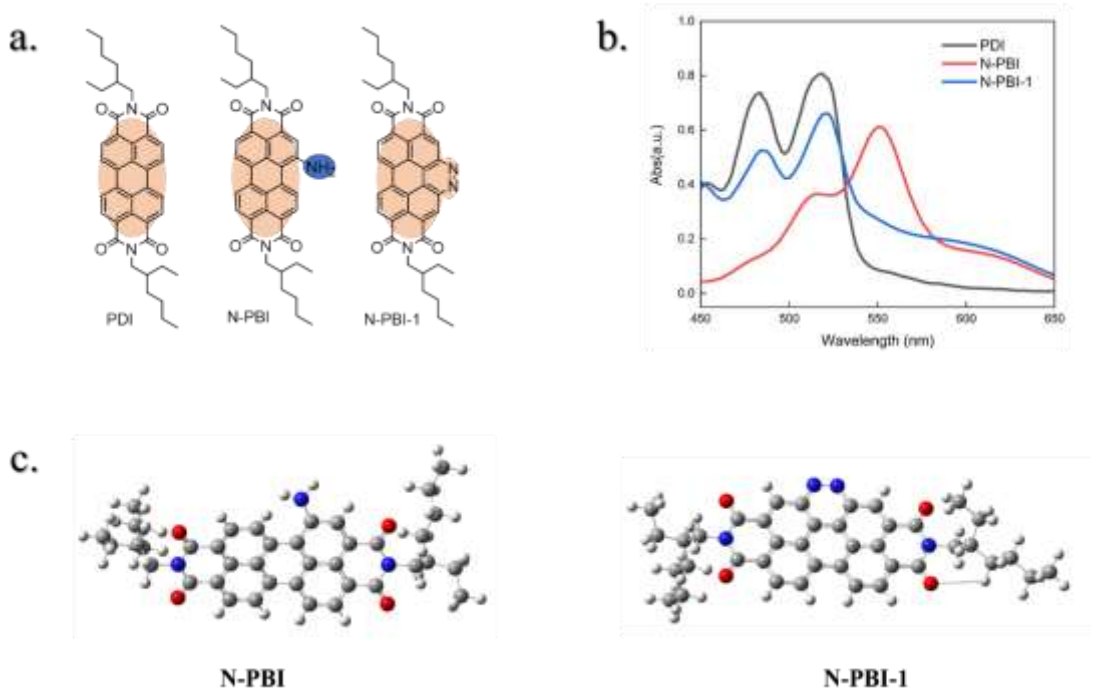

Fig. 2.9 (a) Chemical structures, (b) absorption spectra, (c) optimized molecular models for the compounds relevant in this work

In order to understand the spectroscopic features of N-PBI/N-PBI-1 pair, the UV-vis spectra were acquired in solvents with different polarity. **Fig. 2.10** indicates that in low polarity solvents, such as chloroform, THF, and toluene, N-PBI behaves as monomeric species, with a broad intense absorption around 550 nm, and a weaker shoulder around 510 nm, which likely reflects the p-π conjugation of the aromatic system. In more polar solvents, such as methanol and ethanol, a broad peak appeared in the 600-700 nm range, with a concomitant significant reduction of the 550 nm absorption. This observation can be explained in terms of a molecular aggregation of the lipophilic compound in polar solvents. We speculated that polar solvents may promote the formation of an excimer. **Fig. 2.10** also showed the effects of solvent polarity on the N-PBI emission.

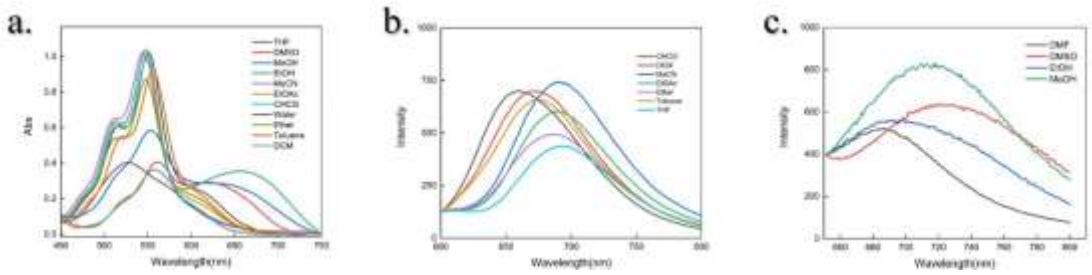

Fig 2.10. UV-vis (a) and fluorescence emission (l_{exc} 550 nm) spectra (b, c) of N-PBI in solvents with lower (b) and higher (c) polarity.

Fluorescence spectra were obtained upon excitation at 550 nm. **Table 2.1** reports the maximum absorption wavelength (l_1), the maximum emission wavelength (λ_2), and the Stokes shift values (Dl) observed for N-PBI in the different examined solvents. The Dl values ranged from 111 nm (chloroform) and 146 nm (acetonitrile), indicating a direct correlation with solvent polarity. It was worth noting that the Stokes displacement in THF (where N-PBI solubility was higher than acetonitrile) also reached 141 nm, which could satisfy the separation of emission spectrum and excitation spectrum, greatly reducing the possibility of self-absorption and self-quenching.

Table 2.1. Stokes shift of probe N-PBI in different solvents

	THF	MeCN	EtOAc	$CHCl_3$	Ether	Toluene	DCM
λ_1(nm)	551	545	547	549	548	556	548
λ_2(nm)	692	691	690	660	687	676	669
$\Delta\lambda$ (nm)	141	146	143	111	139	120	121

For testing the effect of NO on the absorption spectra of N-PBI (10 mM solution), sodium nitroprusside (SNP) was used as NO source. SNP is a highly unstable structure under light conditions and decomposes when exposed to white light to produce NO. To test the optical properties of N-PBI in aqueous systems, we examined the effect of adding PBS buffer to a THF solution of N-PBI (**Fig. 2.11 a, b, c**). We placed the pre-configured solution in a dark box, irradiated it with white light, and collected the absorption spectra of N-PBI before and after ten minutes of light exposure to determine the optimal solvent ratio for N-PBI. At THF: PBS=1:1,

the absorption spectra of N-PBI changed very little. After increasing the ratio of THF (2:1-3:1), the spectra changed significantly. Considering the toxicity of THF, we decided to use 2:1 as the solvent ratio.

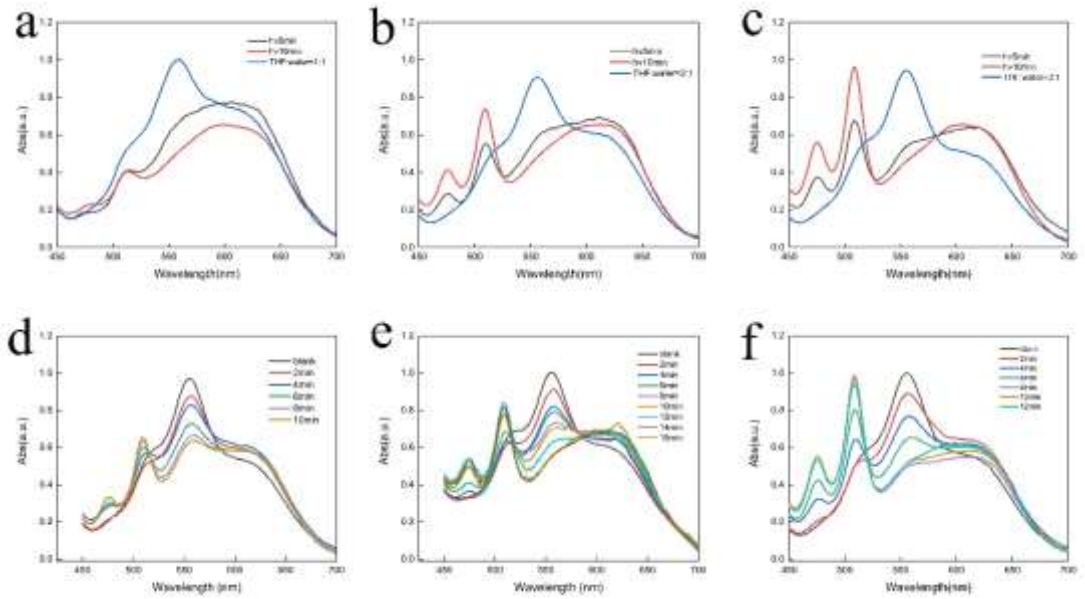

Fig 2.11. UV-vis spectra of N-PBI in different THF/PBS ratios. THF: PBS is (a)1:1. (b)2:1. (c) 3:1. and its response to (d)10μM, (e) 20μM, (f) 50μM SNP.

The spectra indicated that the presence of 10, 20 and 50 μM of SNP caused a progressive decrease of the absorption peak of N-PBI at 550 nm (**Fig. 2.11 d, e, f)**, which disappeared in presence of 100 μM of SNP after an illumination of 10 mins **(Fig. 2.12a)**, time in which the absorption of N-PBI at 475 nm reached the maximum.

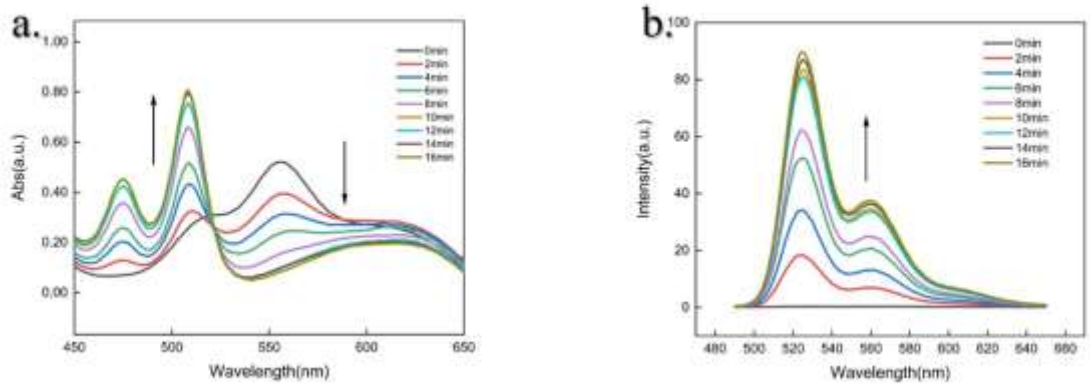

Fig 2.12 (a) UV–vis absorption spectra of N-PBI 10 mM in presence of 100 mM of SNP in THF:PBS ratio 2:1 as a function of the irradiation time; (b) corresponding fluorescence spectra under excitation at 475 nm

Most likely, the peak at 475nm can be attributed to the product of the reaction between N-PBI and NO (*i.e.*, N-PBI-1) during illumination. After the reaction with NO, amino and NO was dehydrated away from the aromatic nucleus, and a new N=N bond was formed at the bay position**.** The same result is expected to be found acquiring the fluorescence spectrum. We selected the absorption wavelength at 475 nm as the excitation wavelength for N-PBI-1, and measured the fluorescence intensity in the 500-650 nm range (**Fig. 2.12b**). Upon exposure to NO, N-PBI generated a new emission peak at 525 nm and reached the maximum emission intensity after 10 min of irradiation, and the spectra did not show any significant change by continuing to extend the light exposure time.

Hence, the 475/556 nm ratio of the absorption wavelengths as a function of illumination time (proportional to NO production) showed a linear behavior, as reported in **Fig. 2.13**.

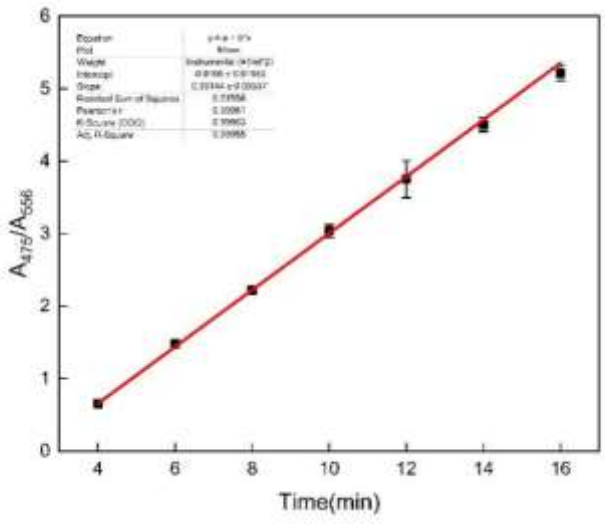

Fig 2.13. The fitting curve of the ratio of the absorption intensity of N-PBI at 475 nm and 556 nm and the illumination time

The results showed that the fluorescence intensity (at 525 nm) linearly correlated with the illumination time in the 0-10 min interval (**Fig. 2.14**). The fluorescence intensity increased 240 times within 10 minutes, and the detection limit of NO was calculated to be 13 nM. The detection limit is calculated by formula 3σ/K. The "σ" is the standard deviation of the fluorescence intensity of 10 μ M N-PBI at 525 nm, and "K" is the slope of the linear equation of fluorescence intensity varying with illumination time. (Fig.2.14) Thus, it can be inferred that N-PBI can quickly and sensitively detects NO.

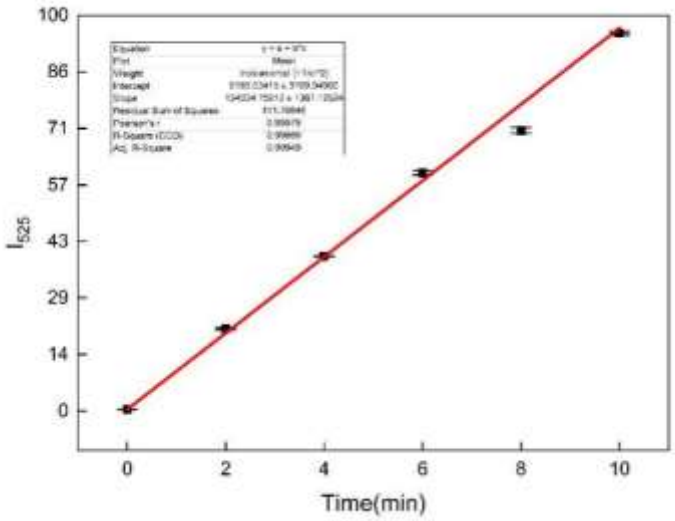

Fig 2.14. Linear relationship between fluorescence emission intensity and light time at 525 nm after N-PBI and NO

In order to better understand the real cause for the blue shift of the 550 nm absorption peak of N-PBI-1, density functional theory (DFT) calculations (B3LYP/6-31g(d) set) were performed to optimize the molecular models of N-PBI and N-PBI-1. Calculations revealed that the electron density of the highest occupied molecular orbital (HOMO) and the lowest unoccupied molecular orbital (LUMO) was distributed around the conjugate rings (**Fig. 2.15**). It was seen that the introduction of the amino group greatly increased HOMO energy level, thus making the molecule excitable at lower energy. After the reaction with NO, the HOMO energy of N-PBI-1 decreased to -6.58 eV, while the LUMO energy decreased much less. Therefore, a larger

energy gap between LUMO and HOMO was generated in N-PBI-1. The increase in the stability showed by N-PBI-1 justify the blue shift of the absorption. After the reaction with NO, the sample was illuminated with ultraviolet light in a dark chamber, and a bright yellow fluorescence was observed.

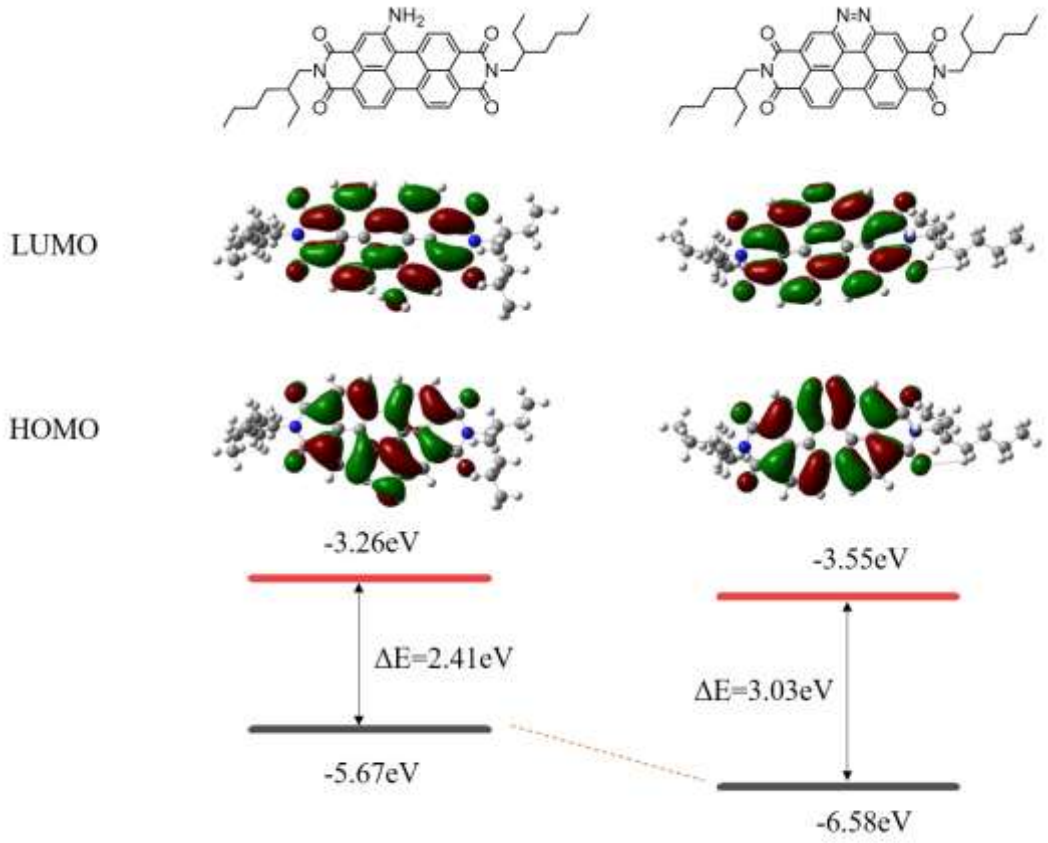

Fig 2.15. Calculated HOMOs and LUMOs of the molecular fluorophores at the B3LYP/6-31g(d) level. The HOMO and LUMO energy levels are also presented in the Fig.s. Note that the LUMO levels are obtained by subtracting the optical gap from the HOMO levels.

In order to further determine whether N-PBI can be used to detect NO in cells, the probe selectivity was tested, and the effect of reactive oxygen species and reactive nitrogen on N-PBI was investigated experimentally. The results are shown in **Fig. 2.16**, whereas it can be clearly seen that N-PBI displayed an excellent selectivity towards NO, and even peroxy-nitrite, which is also a Reactive Nitrogen Species (RNS), is almost undetectable by the probe.

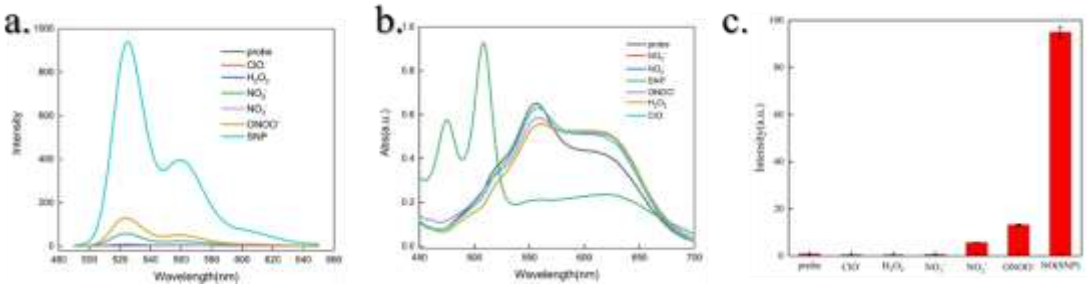

Fig 2.16. Selective fluorescence(a) and UV(b) spectra and histogram(c) of N-PBI

This fully confirms that N-PBI could have the ability to detect NO even in the complex environment of cells and can be applied to cell imaging. As many sensors display a pH dependence of their fluorescence emission, also pH stability of N-PBI was tested. As shown in **Fig. 2.17**, fluorescence is almost pH-independent in the range 3-7, whereas a decrease in the emission is observed in alkaline conditions, though without any wavelength shift. Therefore, N-PBI has the necessary pH stability to act as NO sensor even in weak acid environment, as the cellular one.

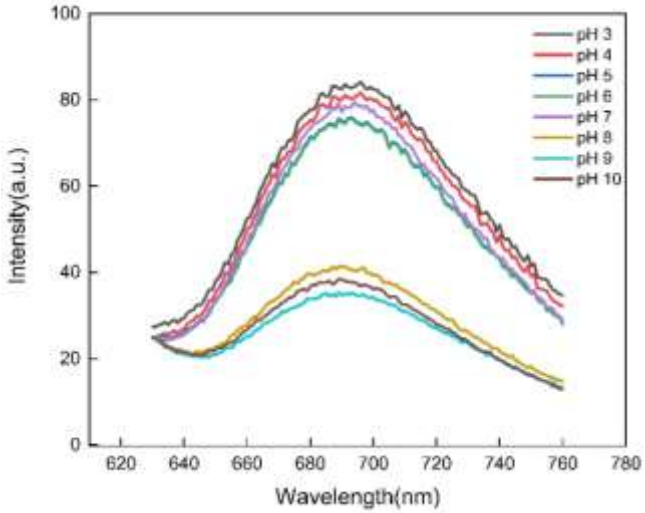

Fig 2.17. Fluorescence Spectra of N-PBI in different pH

Before testing N-PBI to detect intracellular NO, it was deemed relevant to check the cytotoxicity of the probe. **Fig. 2.18** indicates that N-PBI, alone or after the reaction with NO, did not show any cellular toxicity, at least at the highest concentration tested, *i.e.* 12.5 µM. This observation confirms the potential of N-PBI for NO imaging in cells.

We evaluated such a potential, incubating murine 4T1 breast cancer cells with N-PBI (5 μM) at 37℃ for 2 h.

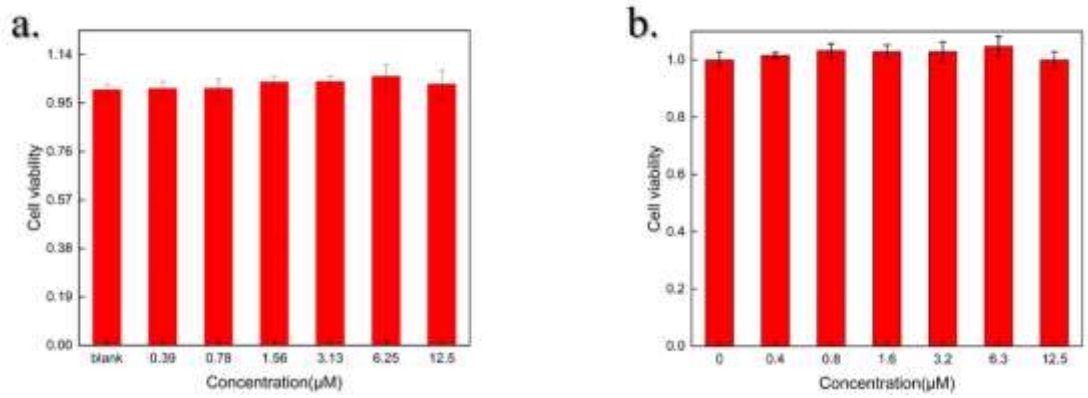

Fig 2.18. The MTS experimental of N-PBI(a) and N-PBI-1(b) was shown their cytotoxicity to cells.

In absence of NO, 4T1 cells showed a bright red fluorescence, with some regions characterized by a very weak green fluorescence (**Fig. 2.19b, c**). After the probe incubation and successive washing, 4T1 cells were co-incubated with SNP for 10 minutes, and the green emission increased significantly, while the intensity of the red channel almost disappeared (**Fig. 2.19e, f**). This is an indication that N-PBI can be successfully used to detect cell-internalized NO. In another experiment, cells were incubated first with the proinflammatory LPS, and then with N-PBI, obtaining a similar result of the previous experiment (green fluorescence and absence of red emission) (**Fig. 2.19h, i**). Finally, when the LPS-stimulated cells were treated with the NO inhibitor L-NAME and co-incubated with N-PBI, the strong green fluorescence was not observed, while the typical red emission of 4T1 cells incubated with N-PBI only was detected (**Fig. 2.19k, l**).

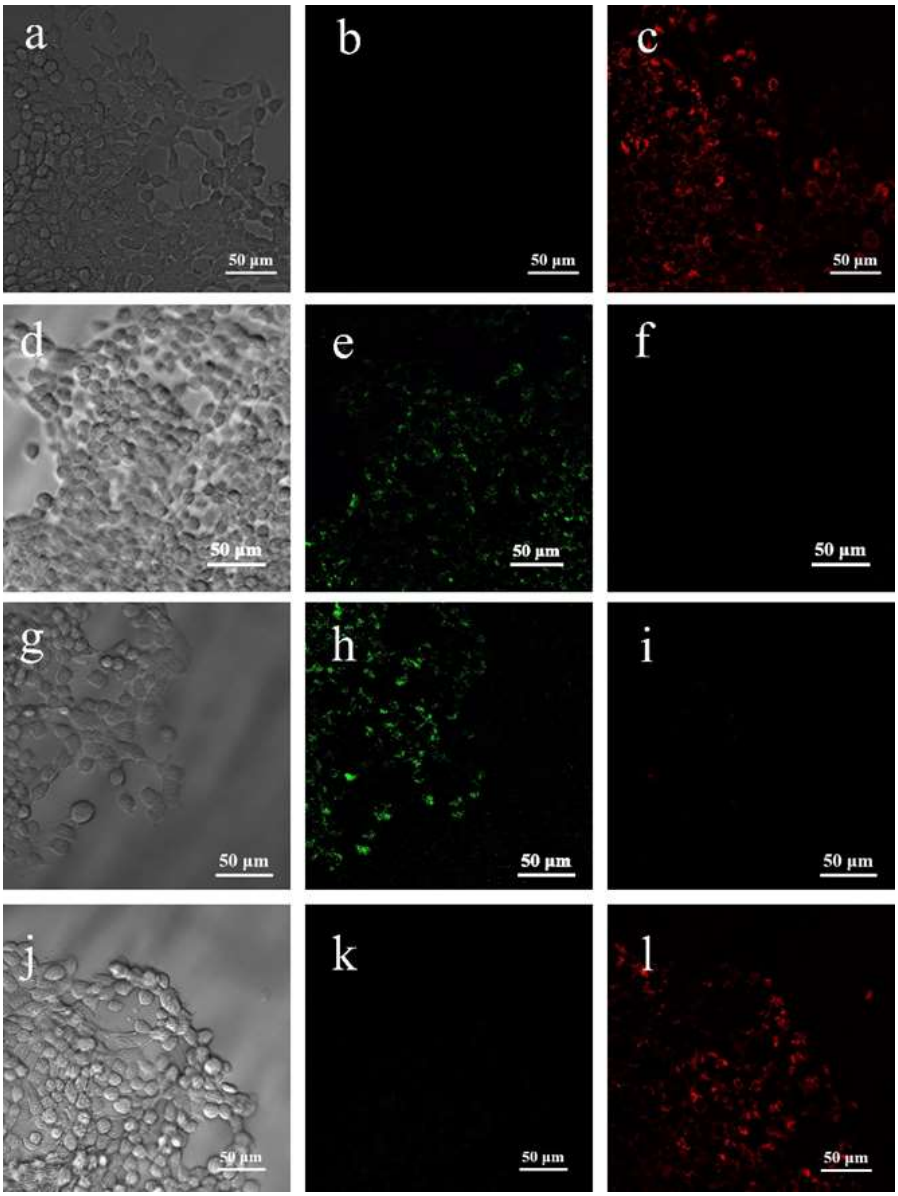

Fig 2.19. N-PBI and 4T1 cells were co-incubated for 2 h. Imaging of bright field (a), green channel (b), red channel (c); Imaging of cells after probe and SNP processing (d-f); Imaging of probe co-incubation with LPS stimulated cells for 48h (g-i); Fluorescence imaging (j-l) co-incubated with probe after adding NO inhibitor L-NAME.

The same results were observed in mouse macrophages (RAW 264.7 cell line) (**Fig. 2.20**). At the same time, N-PBI was uniformly distributed inside the cell, indicating that the probe has good membrane penetration. These findings highlight the great potential of N-BPI for NO cellular imaging.

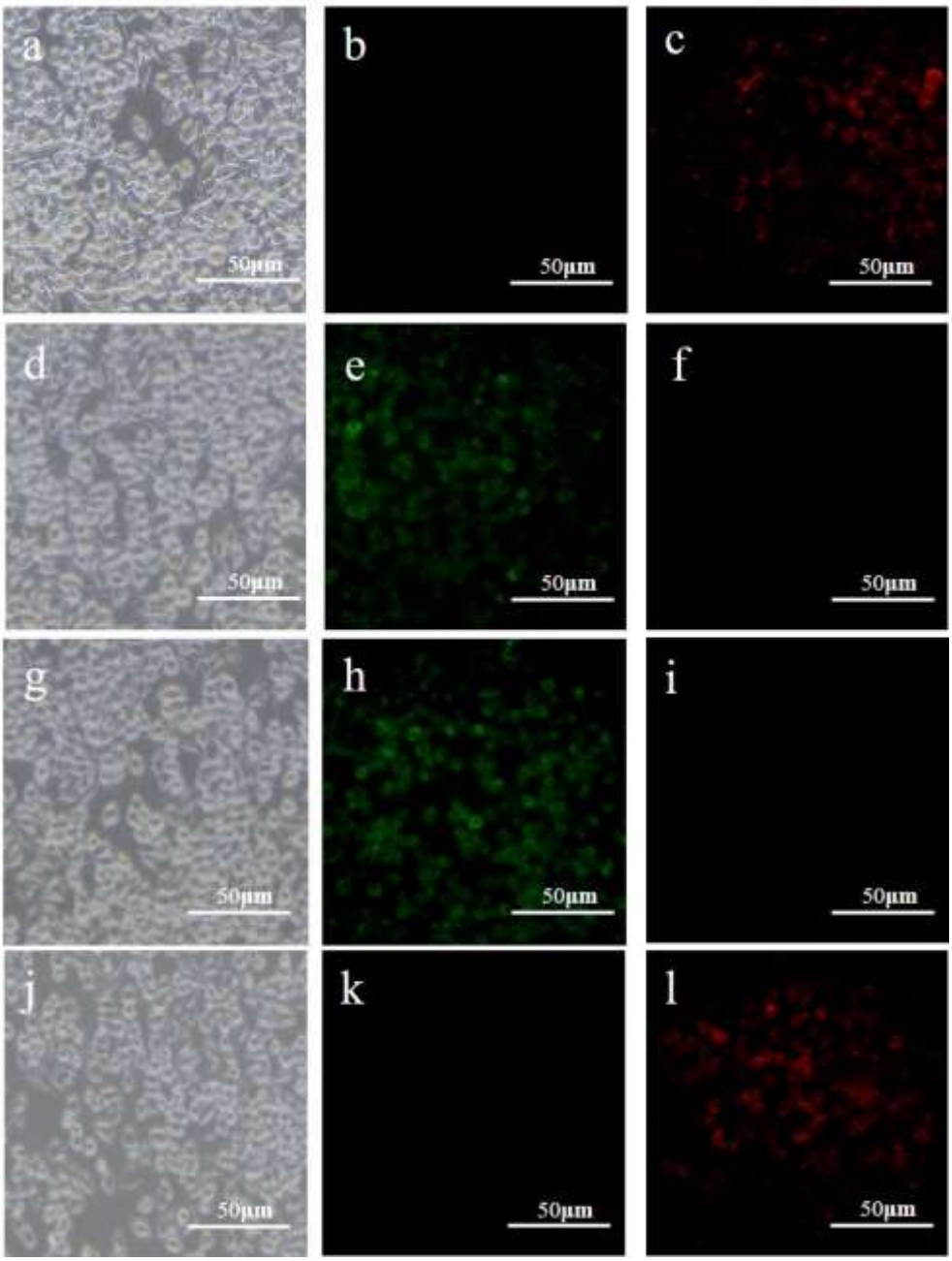

Fig 2.20. N-PBI and macrophages cells were co-incubated for 2h. Imaging of bright field (a), green channel (b), red channel (c); Imaging of cells after probe and SNP processing (d-f); Imaging of probe co-incubation with LPS stimulated cells for 48h (g-i); Fluorescence imaging (j-l) co-incubated with the probe after adding NO inhibitor L-NAME.

The detection of NO Is also very important in the external environment. Due to the observation that the reaction with NO causes a significant and eye-detectable color change, we fabricated N-PBI-based thin tablets to detect nitric oxide in air. **Fig. 2.21** demonstrates the strong ability of N-PBI thin slices to detect NO in air. When the slices were exposed to 5 % of NO, the color quickly changed from purple to red-brownish in less than 1 min. This experiment shows that N-PBI could also find applications as NO sensors in environmental safety.

Fig 2.21. N-PBI-based film sensitive to NO in air before (left) and after (right) exposure to 5 % NO.

2.4 Conclusion

In summary, we designed and synthesized an amino-modified PDI probe N-PBI for sensing NO in different environments (*e.g.* in cells and air). The probe had very good NO selectivity, large Stokes shift, good near-infrared emission, and excellent quantification potential. Furthermore, the probe displayed excellent sensitivity with a detection limit as low as 13 nM. The probe enabled the NO detection in cells as well as in air after its deposition in thin film. Summing up, all these observations confirm that N-PBI has an excellent ability to image NO, which could be of great significance for the detection of diseases caused by endogenous NO imbalance.

Chapter 3 A boron-nitrogen heterocyclic AIE probe for sensitive detection of picric acid

Abstract

This article describes the design and synthesis of a B-N bond-based sensor (BNOH) to detect picric acid (PA), which is easy to synthesize with a high yield. It exhibits aggregation-induced emission (AIE) effect, and its solid bright fluorescence makes it suitable for use as a sensor. As PA sensor, BNOH performs excellently with good selectivity and sensitivity (detection limits as low as 2.9 ppb). The PA response mechanism of BNOH to PA was explored through computational simulation methods. Interestingly, trace amounts of solid PA can be detected by wiping the BNOH paper sensor, achieving convenient and quick PA detection.

Key words: aggregation-induced emission, detect picric acid, fluorescence sensor, paper sensor, quick detection

3.1 Introduction

Picric acid(PA) is an organic compound widely present in military, explosives, dyes, pesticides, leather, pharmaceuticals and chemical industries. Its existence poses serious harm to humans and the environment. [122-126] picric acid is an organic strong acid with a chemical name of 2,4,6-trinitrophenol (PA). It has high destructive power and can cause huge damage to human beings and the environment. The health hazards of picric acid mainly manifest as irritation to the skin and eyes. It can also cause damage to internal organs such as the immune system, liver and spleen. In extreme cases it may even lead to respiratory distress or other serious consequences. Due to its strong water solubility, once entering water bodies it can contaminate groundwater and soil causing severe damage to farmland and natural environments.[127] Moreover, Picric acid may be abused by terrorists posing a potential threat of terrorist attacks which brings security risks for society. The destructive power of picric acid is even stronger than TNT; slight friction on PA powder could trigger explosions.

To detect the presence of picric acid timely and accurately various detection methods have emerged in modern markets such as Surface-Enhanced Raman Spectroscopy (SERS)[128, 129], X-ray Diffraction (XRD)[130], Gas Chromatography-Mass Spectrometry (GC-MS)[131-133], Nuclear Quadrupole Resonance (NQR)[134-138], Ion Mobility Spectrometry (IMS)[139-143],

Cyclic Voltammetry etc., but these methods all have certain limitations. SERS is a spectroscopic technique based on surface-enhanced effect that provides high sensitivity detection. However, the adsorption behavior of PA might be affected by substrate materials or environmental conditions leading to signal changes or instability. In addition, the low concentration detection of PA might be influenced by background interference reducing accuracy. XRD is used for determining material structure & composition, but crystal structures are difficultly obtained during PA detection. GC–MS, is commonly used for analysis and identification of organic compounds. However, due to high sample pre-treatment requirements in PA detection, complex extraction and purification steps may be needed which is time-consuming and laborious. In electrochemical analysis, PA might adsorb unstably on electrode surface leading to signal changes resulting in unreliable detection results.

Fluorescence detection technology has unique advantages in detecting explosives.[144-147] Using fluorescent substances such as emitting conjugated dendrimers[148], poly silanes[149], carbon quantum dots[150-154], metal nanoclusters[155-159], metal gels[160, 161], Metal-Organic Frameworks(MOF)[162-166],organic conjugated polymers[167], organic small molecules[168, 169], and nano-composite materials as probes, the high sensitivity detection of PA can be achieved by detecting their interactions with picric acid. Compared with traditional detection methods, the fluorescence method has many advantages. Firstly, it has high sensitivity that can detect the presence of picric acid at extremely low concentrations. Secondly, the response speed is fast, resulting in accurate and reliable results. Furthermore, the fluorescence method is non-destructive & pollution-free without causing additional harm or contamination to the object being tested. Therefore, the fluorescence method has broad application prospects in the field of picric acid detection providing a feasible modern strategy for protecting human health and environmental safety.

Aggregation-induced emission (AIE) is an emerging fluorescent phenomenon first proposed by Professor Benzhong Tang's team in 2001.[170]AIE refers to weak or quenched fluorescence emission under monomer state but strong fluorescence emission characteristics under aggregation state. Compared with traditional fluorescent probes, AIE has a series of obvious advantages. AIE molecules exhibit strong fluorescence emission under aggregation state with

excellent sensitivity enabling rapid detection at low concentration targets.[171-174] Due to its aggregate-emission feature, AIE easily overcomes the problem where traditional fluorescent probes are quenched due to agglomeration when placed into water. It does not require complex synthesis methods for improving molecular water solubility, enabling sensitive detection of the target in water. AIE molecules also have excellent photostability, able to withstand long-term light exposure without fluorescence attenuation, maintaining persistent signal output. Therefore, AIE technology has been widely favored in multiple fields. In biomedical field, AIE molecules can be used for cell imaging, tumor diagnosis and drug delivery etc., realizing real-time monitoring of biological processes through specific interactions with biological tissues. In environmental detection field, AIE molecules can be used for water quality monitoring, pollutant detection and food safety etc., Possessing advantages such as rapid response, high sensitivity and selectivity. Therefore, developing a new type of AIE probe for PA detection has significant significance and broad prospects.

Here, we have designed and reported a novel B-N bond-based AIE probe, BNOH, for a rapid, sensitive, and accurate detection of PA. BNOH is synthesized easily in one step with excellent purity and yield. The properties of BNOH were studied in detail by spectroscopy to explore the interaction between BNOH and PA. In addition, we optimized the molecular model using density functional theory (DFT) to explain the possibility of fluorescence quenching during the detection process. Finally, we prepared paper sensors using BNOH solution for portable detection. The paper sensor has excellent detection efficiency and limit with simple usage, just contact with powder under UV light, to observe results.

3.2 Experiment

3.2.1 Materials and methods

Unless otherwise noted, materials (including a 10μg/L PA solution in acetonitrile) were purchased from Sigma and used without further purification. For a series of organic molecules, potentially interfering with PA detection, such as benzoic acid, p-nitrophenol, nitrobenzene, and phenol, 10 mL of 1 M stock solutions in THF were prepared. Dichloromethane was distilled from CaH. Toluene was purified by refluxing sodium in nitrogen for several hours and then

distilled to remove trace of water. Deionized water was obtained by Milli-Q purification system (Millipore) with electrical conductivity of 18.2 s/m. Using tetramethylsilane (TMS) as the internal standard, 1H and 13C NMR spectra were recorded on a 14T Bruker Avance III spectrometer. Mass spectra were recorded on the Brook Electron spray Ionization Mass Spectrometer (ESI-MS). The UV-Vis absorption spectra were obtained on CARY50 biological spectrophotometer (Varian Inc., CA., USA). Fluorescence spectra were obtained on a Fluoromax-4 spectrofluorimeter (Horiba Jobin Yvon Inc., USA).

3.2.2 Synthesis of BNOH

Naphthalene-1,8-diamine (158 mg, 1 mmol) and (4-hydroxyphenyl)boronic acid (150 mg, 1.08 mmol) were dissolved in anhydrous toluene and refluxed for 10 hours under argon protection. The product was obtained by removing the solvent through rotary evaporator. Purification was achieved by extraction with deionized water and ethyl acetate (25 mL, four times), separating the organic phase, drying it with sodium sulphate, filtering it, and then subjecting the filtrate to pressure distillation. The product was purified by silica gel column chromatography using Dichloromethane as eluent. The resulting product (white solid, 220 mg) was obtained with a yield of 84.6 %. 1H NMR (600 MHz, MeOD) δ 7.70 (d, J = 7.9 Hz, 2H), 7.50 (s, 2H), 7.07 (t, J = 7.8 Hz, 2H), 6.92 (d, J = 8.1 Hz, 2H), 6.85 (d, J = 7.8 Hz, 2H), 6.52 (d, J = 7.3 Hz, 2H).13C NMR (151 MHz, MeOD) δ 159.00, 142.60, 136.59, 133.60, 127.23, 119.90, 116.25, 114.59, 104.74. MS (ESI) m/z for C16H12BN2O calculated 260.11 [$M+H^+$] found: 261.21. These observations fully agree with literature data. [175]

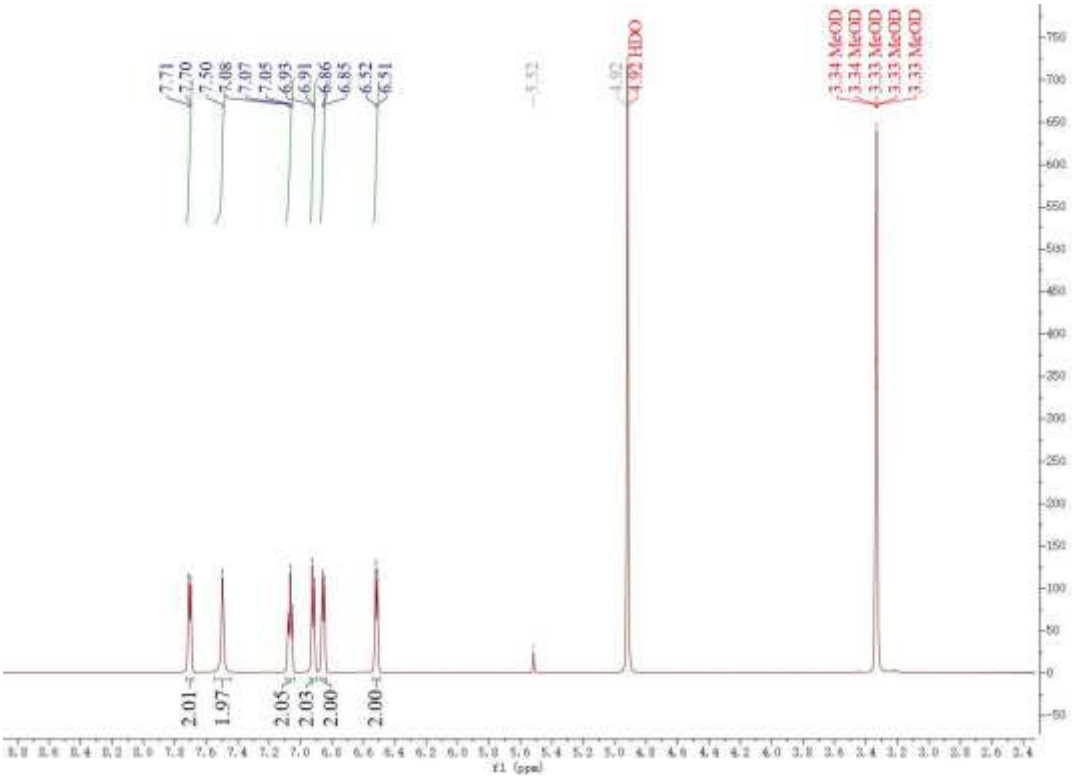

Fig. 3.1 ^{1}H spectrum of BNOH in MeOD

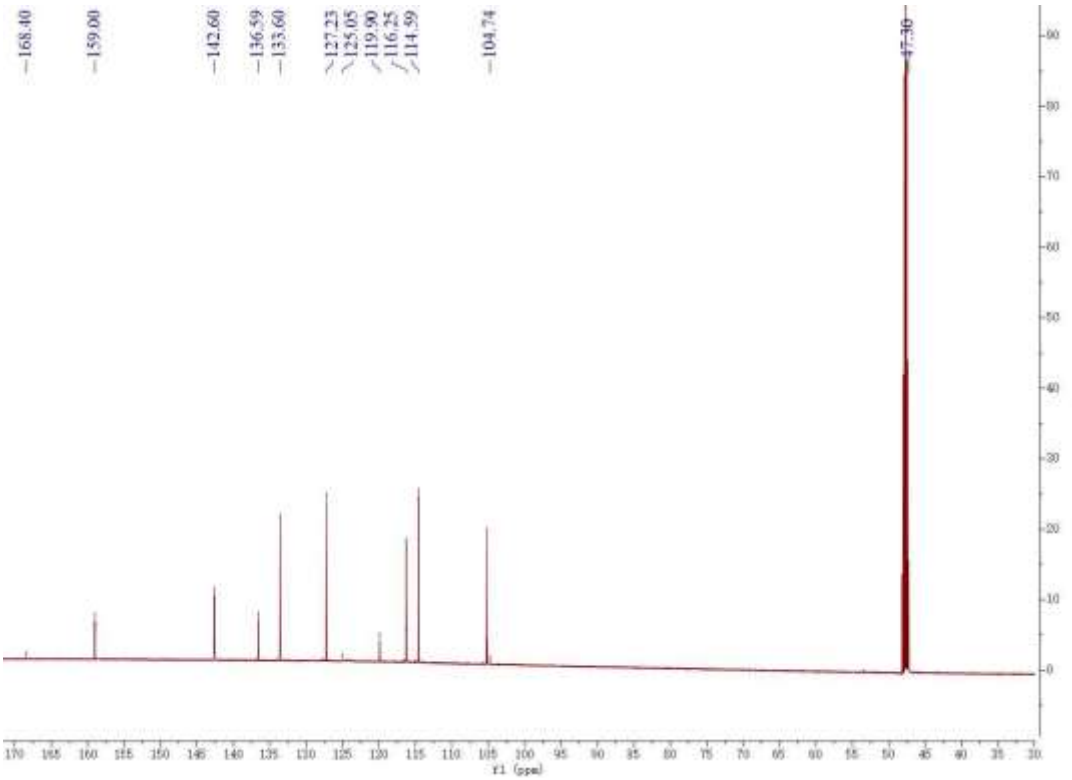

Fig. 3.2 ^{13}C spectrum of BNOH in MeOD

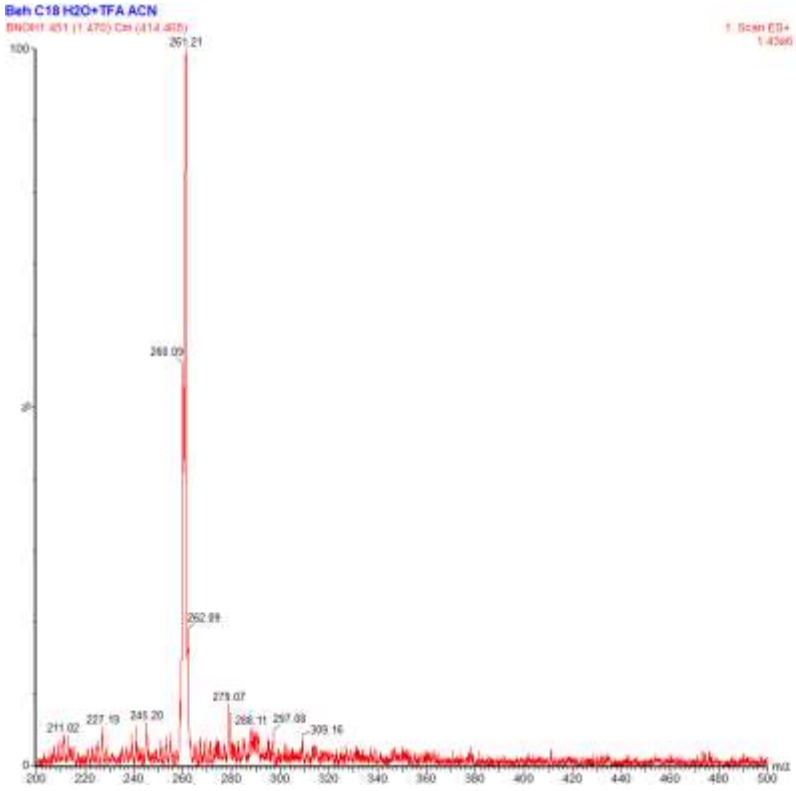

Fig. 3.3 Mass Spectrum of BNOH

3.2.3 Formation of BNOH aggregates

2.6 mg of solid BNOH were dissolved in 1 mL of methanol to obtain a 10 mM BNOH solution, which was stored in the dark at 4°C. At room temperature, 100 μL of the BNOH methanol solution were dropwise added into 48 mL of 1 mM PBS buffer (pH=6.8) and 1.9mL MeOH (96% PBS/MeOH), stirred overnight to obtain a homogeneous solution containing the aggregated BNOH with a concentration of 20 μM. Unless otherwise specified, this solution was used for characterizing the UV-VIS, fluorescence properties and the PA detection of BNOH. The response experiment with PA was conducted using the above described solution of aggregated BNOH. The excitation wavelength for BNOH was set to 330 nm (3 nm of slit width).

3.2.4 Spectrofluorimetry of BNOH

The fluorescence properties of BNOH were tested by 20 μM solution in different solvents: Dimethylformamide, Acetonitrile, Methanol, Tetrahydrofuran, Chloroform and n-Hexane.

3.2.5 Testing BNOH-PA interaction

Job's plot was used to characterize the interaction between PA and the BNOH sensor. In this

experiment, a series of solutions obtained by mixing different volumes of the aggregated BNOH solution and PA to a fixed volume of 1 mL were prepared. The fluorescence spectra of the resulting solutions were acquired at room temperature.

$F_{job} = (1-x)\ F_0-F$

x is the molar fraction of PA, F0 and F are the fluorescence intensity of solution in the absence and presence of PA. The total molar concentration of the two components should be kept at a fixed value while the molar fraction of any component is variable. In this experiment, the total concentration of BNOH and PA was 4×10^{-5} M, and the molar fraction of PA in the mixture was 0, 0.1, 0.2, 0.3, 0.4, 0.5, 0.6, 0.7, 0.8, 0.9, and 1.0.

3.2.6 Limit of detection (LOD) experiments

The PA detection limit (3σ/k) of the BNOH sensor was calculated by analyzing the fluorescence of BNOH at different concentrations of PA. In the detection limit equation, σ is the standard deviation, and k is the slope of the linear curve. The standard deviation (σ) was obtained from the bank test of the aggregated BNOH solution in the absence of PA. The slope (k) was obtained by plotting the concentration of PA versus the fluorescence intensity.

3.2.7 Computational methods

DFT calculations (ORCA 5.0.31) [59] were used to optimize the structure of the adduct formed between PA and BNOH in the non-aggregated monomeric form. Geometry optimization and frequency calculation were performed at the B3LYP-D3BJ/6-31G(D) theoretical level. To calculate interactions and eliminate the influence of Basis Set Superposition Error (BSSE), gCP correction was used in the calculation[176]. Molecular orbitals and electrostatic potential maps were obtained at the B3LYP-D3BJ/def2-TZPP level. BNOH and PA monomer molecules are optimized on gaussian09, and the results of molecular orbitals and electrostatic potential diagrams were obtained at B3LYP /6-31G(D) level.

3.2.8 Fabrication of a paper-based prototype of BNOH as PA sensor

A solution of 100 μM of BNOH in methanol was prepared. Filter paper was cut into appropriate sizes and immersed in the solution for 2 hours. The paper was then taken out, laid flat on a glass plate, and air-dried in a fume hood before use.

3.3. Results and Discussion

The synthetic route followed for obtaining BNOH is reported in Scheme 3.1. The compound was easily obtained by refluxing 2-aminonaphthalene with hydroxyphenylboronic acid in toluene. The Compound BNOH was characterized by 1H NMR, 13C NMR and Mass in (**Fig. 3.1-3.3**). Although the structure of BNOH has been already reported in literature,[175, 177, 178]these reports only improved the synthesis method of BNOH but did not effectively apply it to detect explosive PA systems. In the structure of BNOH there are two electron-rich functional groups, the B-N bond region and hydroxyl group, which may effectively interact with PA. Both chemical entities are likely to produce photoinduced electron transfer effects during light excitation resulting in different emission characteristics. Therefore, we determined the photo physical properties of BNOH and its capability to act as PA sensor using UV and fluorescence spectroscopies as well as DFT calculations.

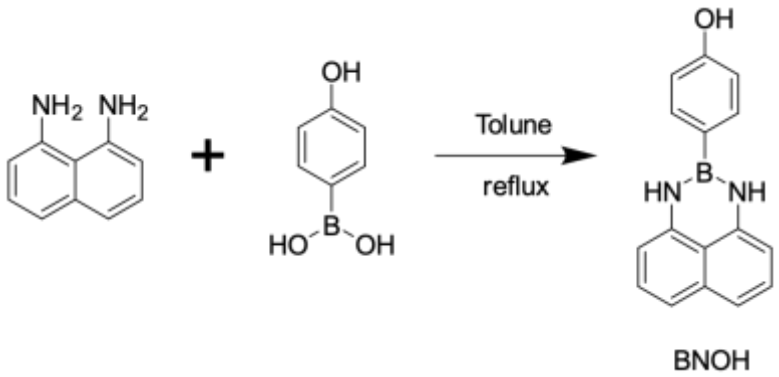

BNOH

Scheme 3.1. Synthesis route of BNOH

Firstly, we tested the basic spectral properties of BNOH. In MeOH, BNOH exhibited a broad UV absorption at 330 nm (**Fig. 3.4A)**. The fluorescence emission showed two peaks at 381 nm and 425 nm (**Fig. 3.4B**), which originate from the vibration of phenol and naphthylamine moieties, respectively. This emissive pattern is confirmed in the spectra acquired in different solvents (**Fig. 3.4C**), with a slight red shift with the increase of solvent polarity.

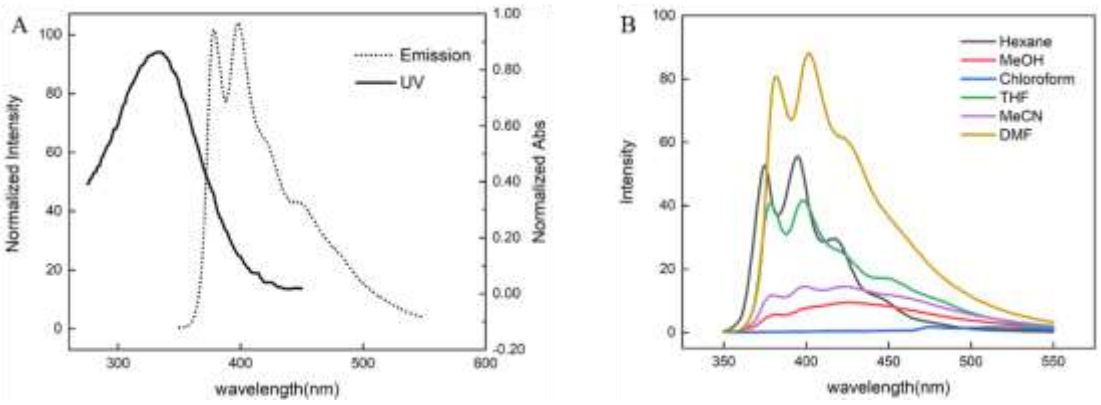

Fig. 3.4. (A) UV-Vis (solid line) and fluorescence (dashed line) spectra of BNOH in THF. (B) Emission spectra of BNOH in different solvents.

Table 3.1 reports the Stokes shift values of BNOH in different solvents. Although DMF is also a highly polar solvent, BNOH dissolves well in it, so its emission intensity is stronger than that in other solvents.

Table 3.1. Stokes shift of BNOH in different solvents

Solvent	λex(max)	λem(max)	Stokes shift
DMF	332nm	403nm	71nm
MeCN	331nm	400nm	69nm
MeOH	330nm	425nm	95nm
THF	330nm	399nm	69nm
$CHCl_3$	330nm	395nm	65nm
Hexane	330nm	395nm	65nm

We also tested the fluorescence emission intensity (at 425 nm) of BNOH in methanol solution at different concentrations (**Fig. 3.5**). Within 100 μM concentration range, the fluorescence intensity progressively increased with concentration; however, when the concentration reached 500 μM, fluorescence started to be quenched and at 1 mM the system was not fluorescent anymore. From this observation, to ensure sensitivity, a BNOH concentration of 20 μM for selected for the successive experiments..

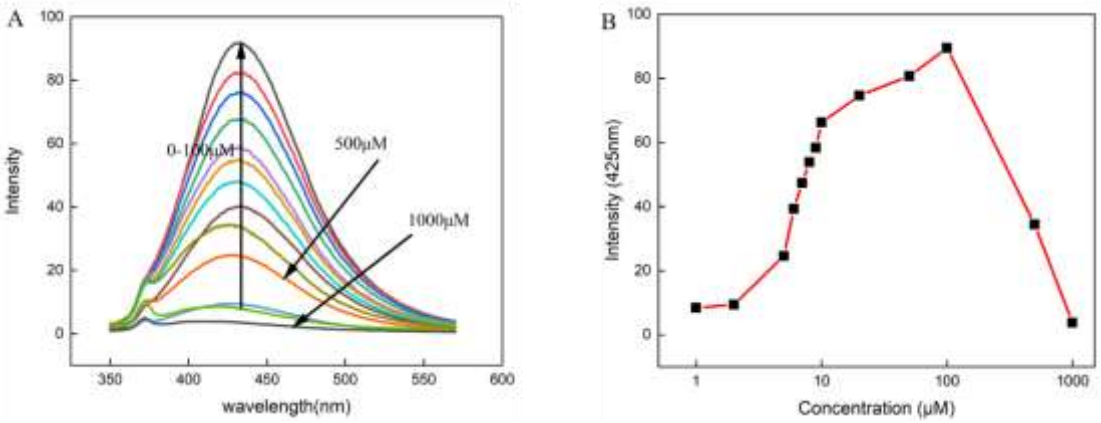

Fig. 3.5 (A) emission spectrum of S1 (A) BNOH at different concentrations (B) fluorescence curve of BNOH at 425nm with concentration

Next, we investigated the photoluminescence properties of BNOH in water (**Fig. 3.6a**). By varying the water/methanol ratio, we found that as the water content increased, the emission spectrum of BNOH gradually changed the pattern and evolved to a single emission peak (centered at 400 nm) in the solution with the maximum water fraction (96 %), indicating aggregation of BNOH in water. The plot reporting the emission intensity at 425 nm (**Fig. 3.6b**), showed that when the proportion of water reached 70%, the emission intensity of BNOH switched from quenching to AIE effect.

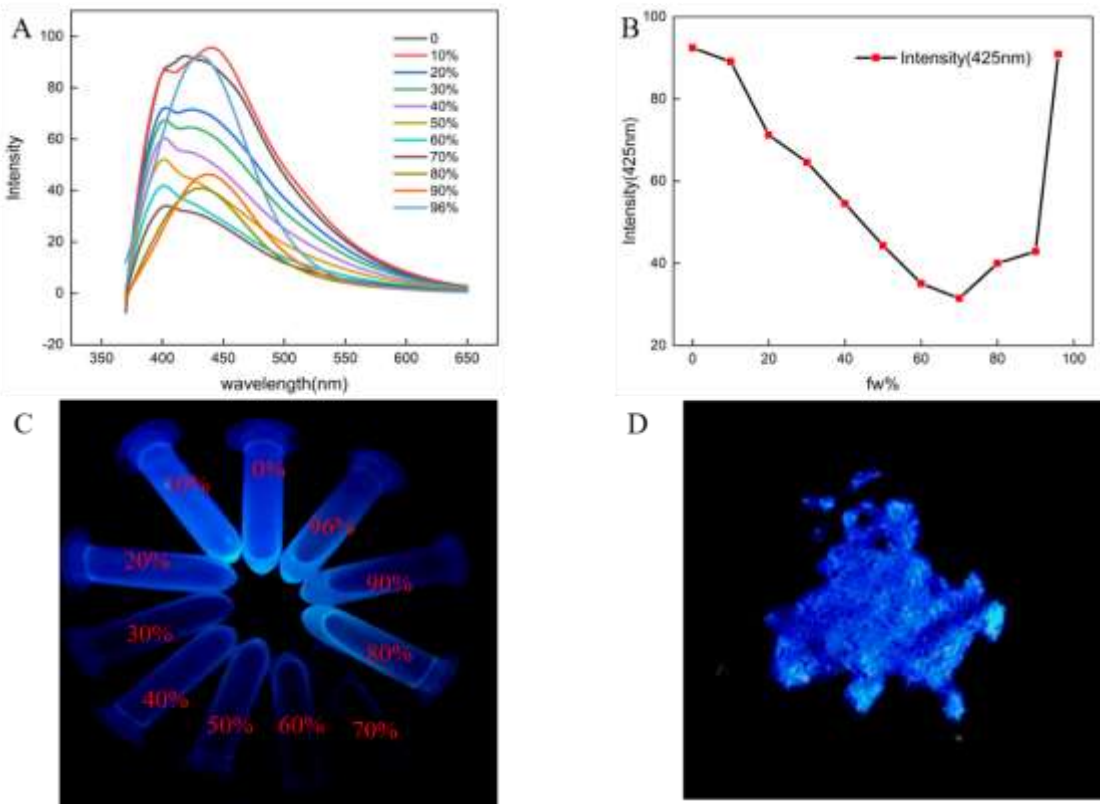

Fig. 3.6. (A) Emission spectra of BNOH in mixed solutions of water/methanol at different ratios. (B) Fluorescence intensity change curve of BNOH at 425 nm. (C) Optical color change of BNOH in different water/methanol percentage mixed solutions. (D) The luminescence of BNOH solid powder under ultraviolet lamp.

This suggests that at a ratio of 70%, BNOH started to aggregate. The UV spectra of BNOH are also displayed in **Figure 3.7**. from a ratio of 70% onwards, the fluorescence keeps increasing due to the gradual insolubility of BNOH in the mixed MeOH/water solution, which is exhibiting a typical AIE phenomenon due to the formation of aggregates, as confirmed by the dynamic light scattering (DLS) results. (**Fig. 3.8**)

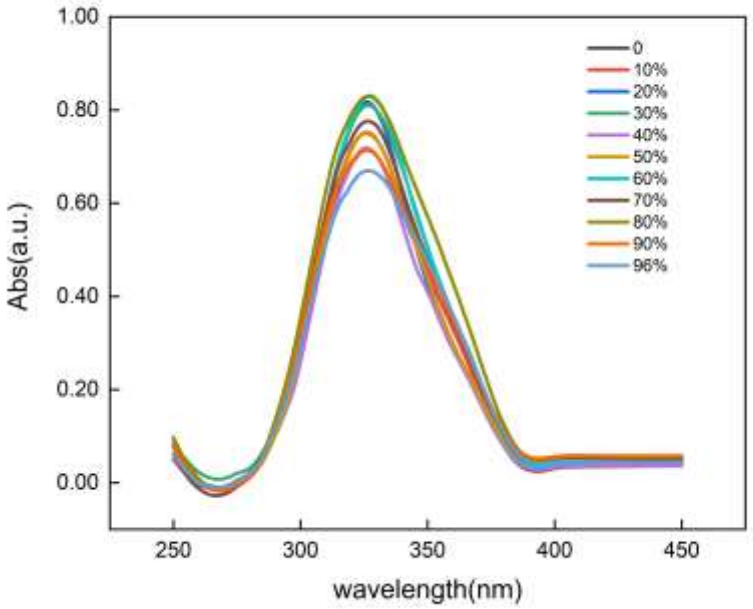

Fig. 3.7 UV spectra of BNOH in mixed solutions of water/methanol at different ratios.

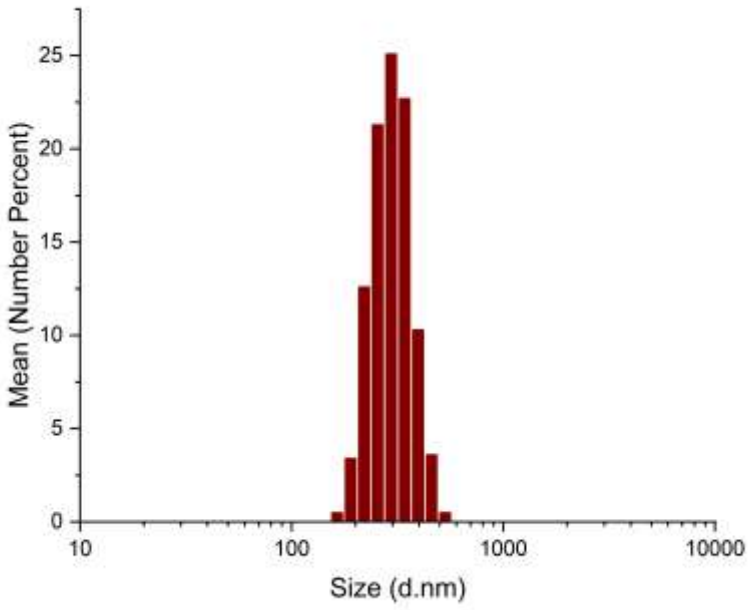

Fig. 3.8 Size of BNOH in mixed solutions of water/methanol at 96%.

The BN bond will behave like a carbon-carbon double bond in the structure, [179, 180] as the

aggregation proceeds, the vibration of the naphthalene ring connected by the B-N bond is suppressed, and the rotation of the benzene ring connected to the boron atom is also suppressed, and this part of the energy is used for light emission, resulting in AIE. Such behavior provides the rationale for using BNOH as fluorescent sensor in aqueous environments.

According to this hypothesis, we evaluated the ability of BNOH to detect picric acid. By adding different concentrations of PA (0-100 μg/mL range) to a solution containing 20 μM BNOH (**Fig. 3.9A**), we found that as the concentration of PA increased, the fluorescence of BNOH was quenched and the final fluorescence intensity differed by a factor of 526 compared to the starting solution with no PA added. The quenching efficiency $[(I_0\text{-}I)/I_0]$ at 100 μg/mL was 98.1%. The quenching was linear with the PA concentration only in the 0-10 μg/mL range (**Fig. 3.9B**), where the probe was very sensitive to the analyte (R-Square 0.98), resulting in a limit-of-detection (LOD) as low as 2.9 ppb. **Fig. 3.9A** indicates that upon increasing the PA concentration, the fluorescence experienced a red shift, which can be attributed to a photoinduced electron transfer (PET) between PA and BNOH. To delve deeper into the quenching dynamics, we computed the Stern−Volmer constant, revealing a value of $5.88\times10^{8}M^{-1}$.

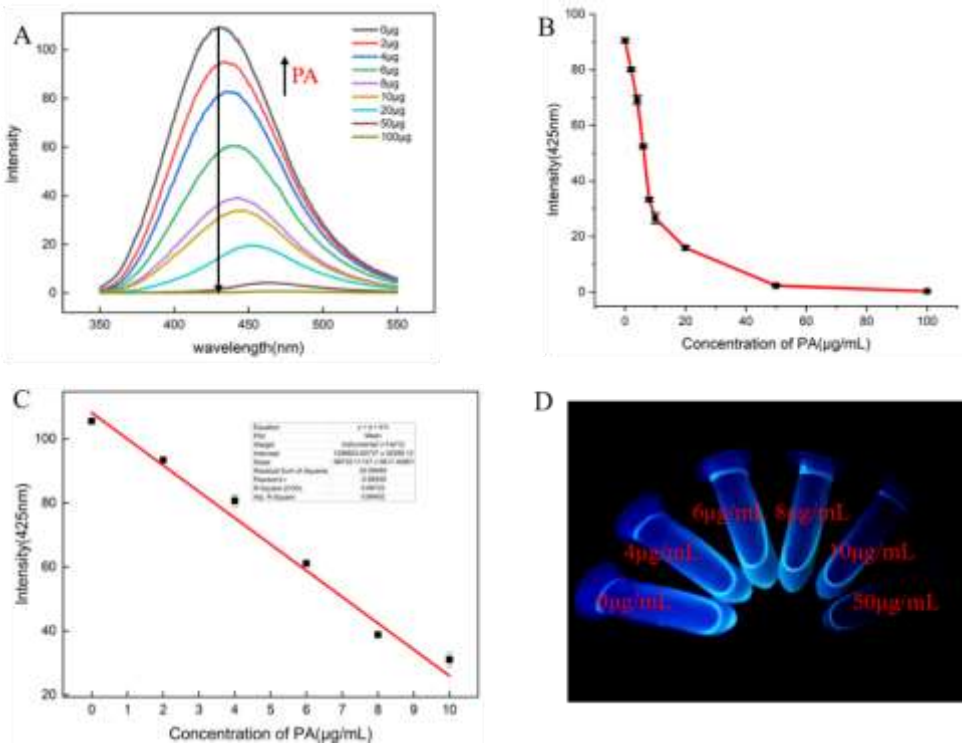

Fig. 3.9. (A) Fluorescence spectra of BNOH solution with different concentrations of PA. (B)

Changes in fluorescence intensity of BNOH at 425nm, (C) the linear relationship between fluorescence intensity at 425nm and PA concentration, (D) The optical color of BNOH solution changes after adding different concentrations of PA

To probe deeper into the sensitivity of PA detection using BNOH, Stern-Volmer plots were generated. As depicted in **Fig. 3.10**, at higher PA concentrations, the curve exhibited an upward bend, suggesting an over-amplified burst effect.[181] In contrast, at lower PA concentrations (0-20μg/mL), the Stern-Volmer plot displayed linearity. The Stern−Volmer equation takes the form:

$I/I_0 = 1 + K_{SV}[Q]$

Here, I_0 represents the initial fluorescence intensity, while I signify the final intensity subsequent to the introduction of the analyte, and [Q] denotes the concentration of the analyte.

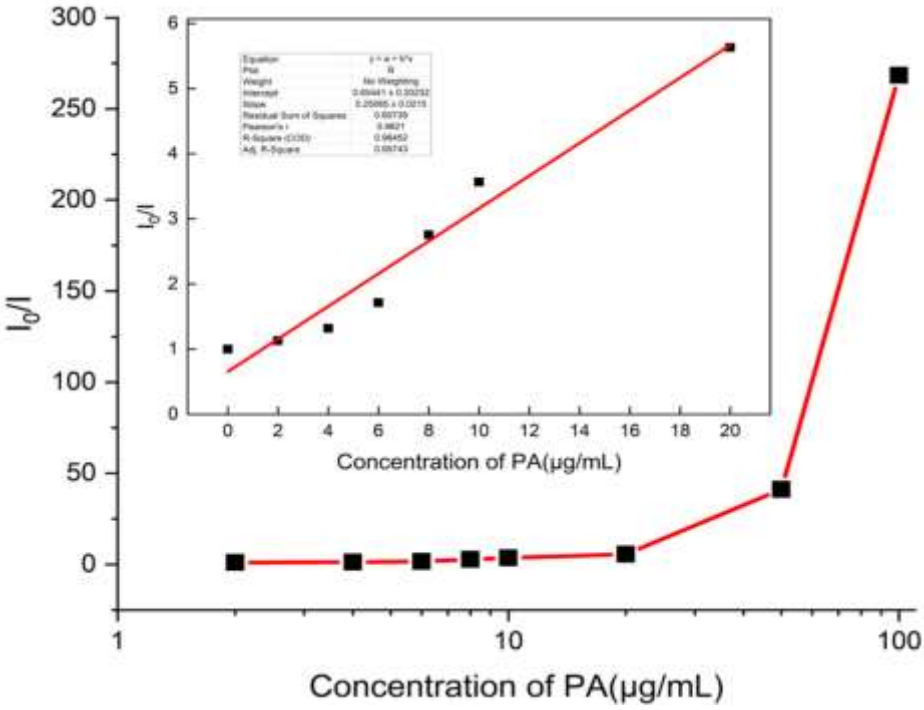

Fig. 3.10. Stern–Volmer plot in response to PA (inset: Stern–Volmer plot obtained at lower concentration of PA).

To understand the binding mode and assess the stoichiometry of the interaction between BNOH and PA, we measured the fluorescence intensity at 425 nm of 1 mL solutions containing a different molar fraction of PA (xPA) and BNOH (Job plot, **Fig. 3.11**). The result obtained is a

clear indication that the maximum change in intensity occurs when xPA is 0.46, indicating that a 1:1 complex is formed between the two interacting partners. However, even when more PA (1 to 2 equivalents) is added, the quenching is still observed.

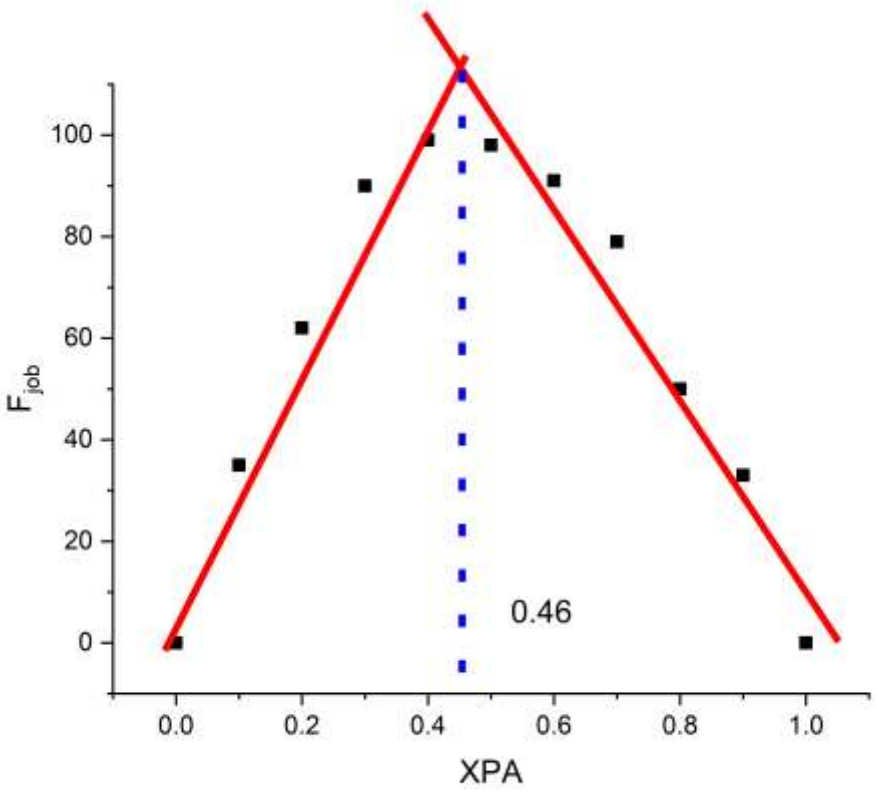

Fig. 3.11. Job plots of BNOH with PA in PBS

Mass spectrometric analysis revealed distinctive changes when PA was introduced in varying quantities. Upon adding 0.2 equivalents of PA, a notable reduction in the molecular peak of BNOH at 260 was observed, accompanied by the emergence of a unique new peak at 429. Subsequent gradual addition of PA up to 0.6 equivalents resulted in the formation of a complex peak at 484. Further addition of PA to reach 1 equivalent led to the complete disappearance of peak 429, leaving behind only the newly emerged peak at 485.(**Fig. 3.12**).

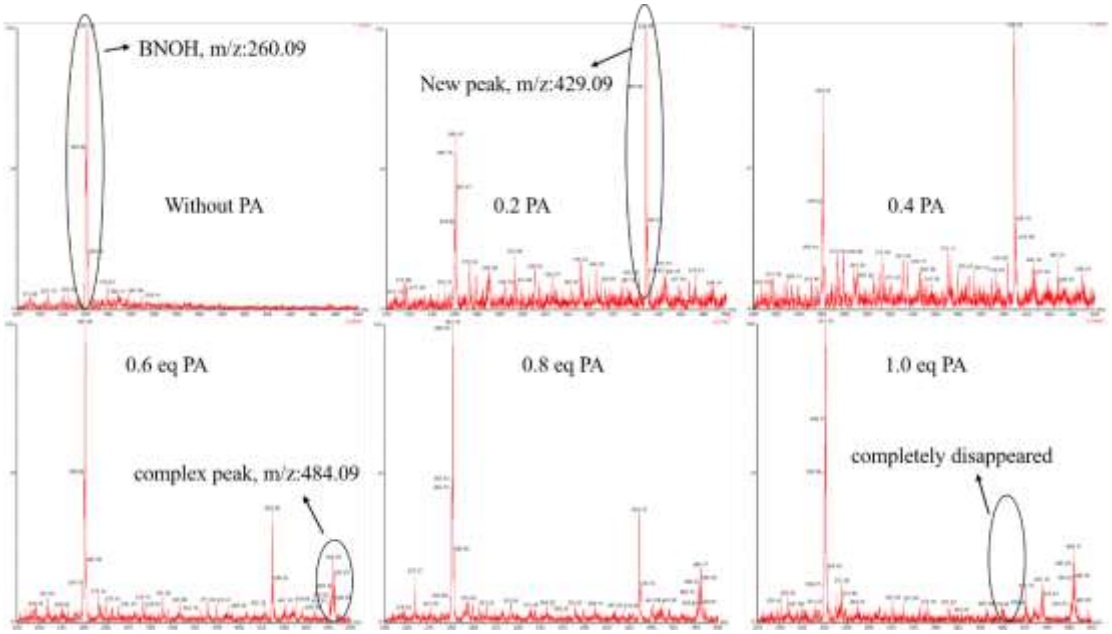

Fig. 3.12 Mass titration of C1 upon gradual addition of PA(0-1eq)

We attempted to explain this phenomenon by optimizing the molecular model using density functional theory (DFT). The molecular structures of BNOH and PA were optimized using DFT (B3LYP/6-31G(D)) method, while the molecular structure of the BNOH/PA adduct was calculated using B3LYP-D3BJ/6-31G(D) method to ensure the comprehension of the quenching process. The results showed that PA and BNOH formed a planar arrangement (**Fig. 3.13**), which facilitates the recognition of PA by BNOH. During this process, BNOH forms π-π stacking with PA, and the NH hydrogens connected with boron can reinforce the interaction through hydrogen bonds with PA.

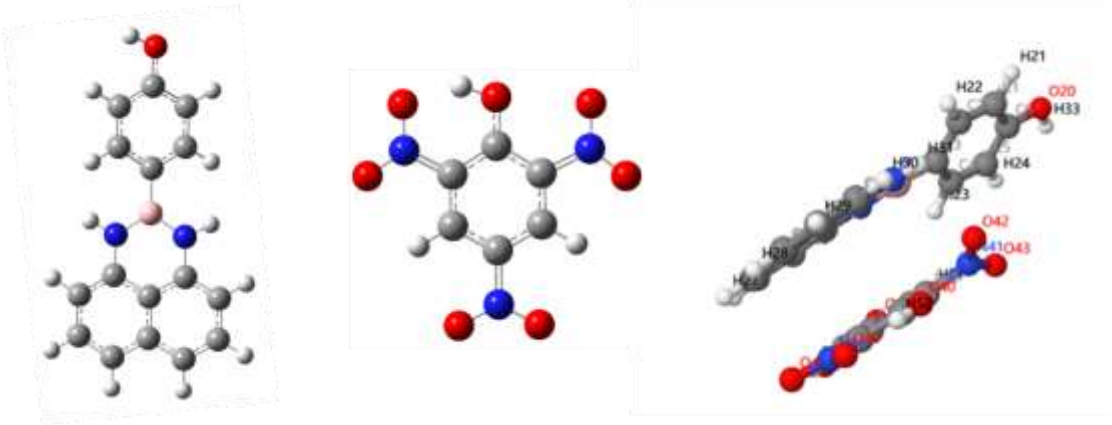

Fig.3.13 molecular structure optimization through computational simulation, from left to right

in turn, BNOH,PA, the complex of the two.

Molecular orbital energy level calculation **(Fig. 3.14)** also showed different electronic arrangements. In the single molecules, the orbital distribution of BNOH was clear, with HOMO located in naphthalene part and LUMO almost distributed throughout the molecule, with an energy difference of 4.08 eV. The orbital distribution of PA was simpler, with an energy difference around 4 eV. It is worth noting that the HOMO energy of PA is much lower than that of BNOH, so it is relatively more stable than BNOH. The LUMO energy of PA is between HOMO and LUMO energies of BNOH, only differing from HOMO by 0.69 eV; such low gap can easily promote the transfer of their joint excitation energy onto PA, thus resulting in fluorescence quenching feedback phenomenon.

The results obtained from the joint-optimization of both molecules are close to our guesswork: HOMOs orbitals still arrange at naphthylamine moiety in composite molecule without significant change compared to individual ones; however its total potential energy is reduced due to the influence of PA, which is -5.4 eV. The introduction of the PA molecule in the composite system has a significant impact on the LUMO orbital distribution of the BNOH monomer molecule, which is now predominantly distributed on the PA molecule. Additionally, the LUMO energy values of the complex molecules closely resemble that one of PA, with values of -3.68 eV and -3.93 eV, respectively. This represents a remarkable change compared to the BNOH monomer. Furthermore, the energy difference (△E) between the excited state and the ground state in the complex is significantly reduced from 4.08 eV to 1.72 eV. This reduction indicates that, upon excitation, BNOH absorbs energy and the electrons that would typically transition to the S1 orbital of BNOH now transition to the S1 orbital of PA. Subsequently, these electrons return to the ground state, resulting in a photoinduced electron transfer process. As a consequence of this transfer, the fluorescence of BNOH is effectively quenched.

	BNOH	PA	PA+BNOH
LUMO	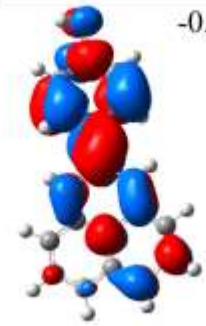 -0.54eV	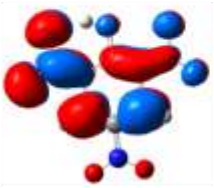 -3.93eV	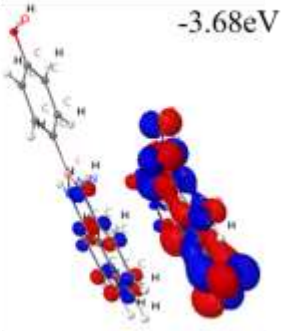 -3.68eV
HOMO	 -4.62eV	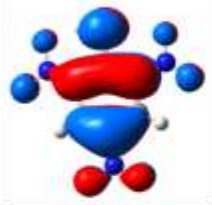 -8.30eV	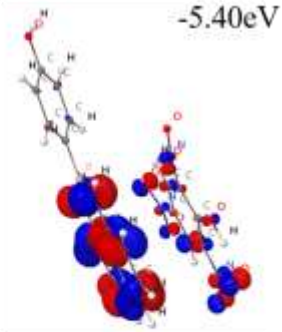 -5.40eV
△E	4.08eV	4.37eV	1.72eV

Fig. 3.14. Molecular orbital energy level distribution of BNOH, PA and their complex.

The molecular electrostatic potential map (ESP) of BNOH and PA, as well as their complex, were calculated (**Fig. 3.15**). Red and blue represent the negative and positive potentials, respectively. The ESP maps obtained for BNOH and PA suggest that the drive-force of the formation of the adduct is the occurrence of non-covalent bonds with interaction energy calculated at -5.14 kcal/mol, supported by low-energy interactions.

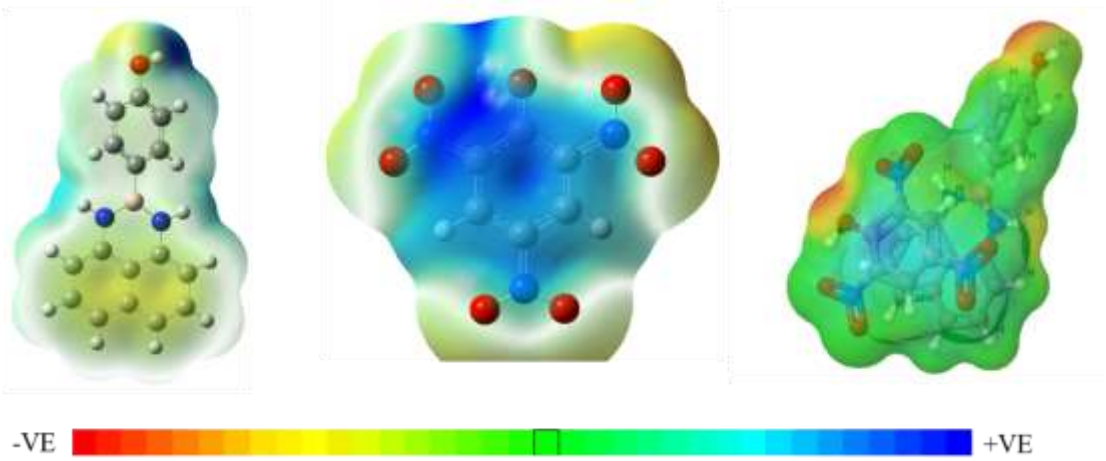

Fig. 3.15 The DFT computed molecular electrostatic potential map of BNOH, PA, and complex.

We believe that one the key factors in the formation of the adduct is the nitro functional group of PA, because the electron-deficient feature of this group can favor PET effects. To confirm the role of the nitro group, the fluorescence intensity of BNOH was measured in presence of different aromatic compounds (**Figs. 3.16,3.17**). We found that the presence of a single nitro group (NB), as well as a single carboxylic group (BA), or a single hydroxyl group (PH) did not quench the fluorescence. Quenching was effective in presence of both one nitro and one hydroxyl groups (NP), though the quenching effect was much lower than PA, suggesting the role of the number of the two substituents. This observation is relevant to highlight the excellent selectivity of BNOH to act as PA sensor.

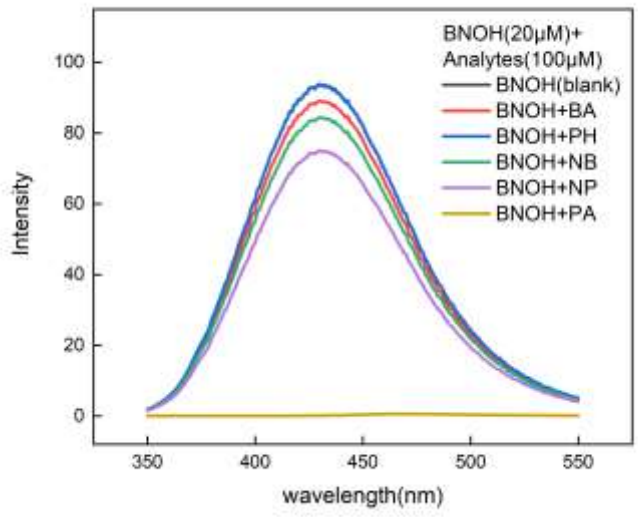

Fig. 3.16. BNOH with fluorescence emission spectra of different aromatic compounds. Benzoic acid(BA), Phenol(PH), Nitrobenzene(NB), p-Nitrophenol(NP), Picric acid(PA).

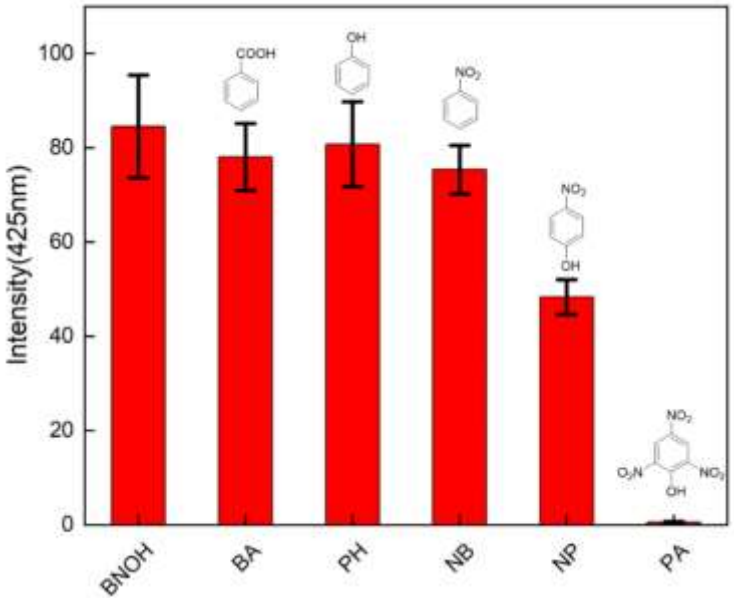

Fig. 3.17. Comparison of fluorescence emission intensity between BNOH and different aromatic compounds at 425nm.

We also conducted some stability tests on BNOH. First, we assessed the stability of BNOH in water solution at different pH values (**Figs. 3.18,3.19**). Due to the presence of phenolic group, whose pKa value is usually between 10-12, BNOH is deprotonated in an alkaline environment and its electron conjugation structure is destroyed, resulting in fluorescence disappearance.

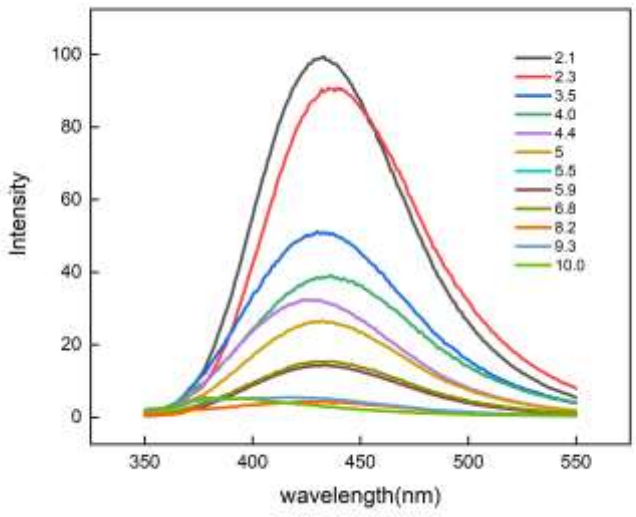

Fig. 3.18. Fluorescence Emission Curves of BNOH in different pH

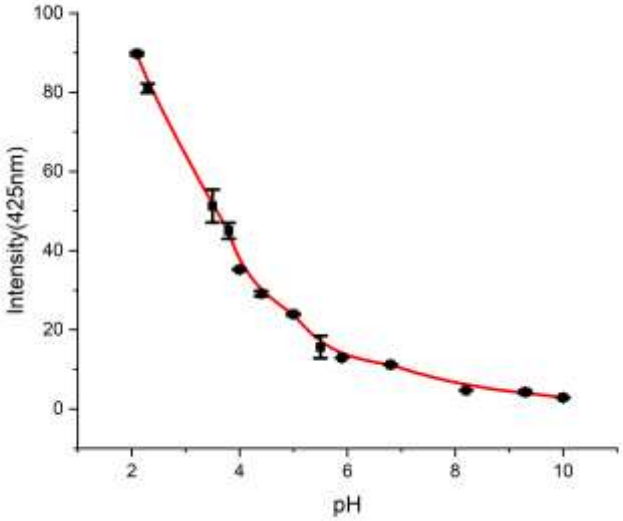

Fig. 3.19. Variation of fluorescence emission intensity of BNOH with pH at 425nm

Subsequently, we tested the photostability of BNOH (**Fig. 3.20**). Under continuous UV irradiation at 330 nm for 2 hours, there was almost no change in UV absorption intensity, while a slight decrease was observed in the fluorescent emission intensity at 425 nm, which demonstrated an excellent photostability.

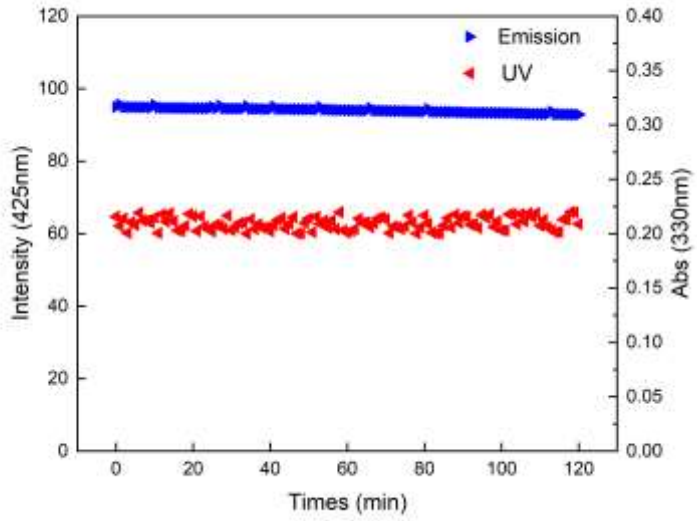

Fig. 3.20. Changes of UV (red) absorption intensity and fluorescence (blue) emission intensity of BNOH after continuous UV irradiation

On this basis, BNOH appears to be a promising system to act as PA sensor. Currently, the detection of PA and, in general, explosives requires complex, costly, and time-consuming operations. Explosives can pose significant hazards when they come into contact with human skin or certain materials; even slight friction can cause explosions that may also contaminate water sources. Therefore, the development of rapid and convenient detection methods has a great significance.

To move a bit forward in this direction, we have developed a paper-based PA sensor based on BNOH by immersing paper strips for 2 hours into a methanol solution containing 100 μM of BNOH, followed by drying the strips in a cool place. Then, we dipped the paper strip into acetonitrile solution containing PA or touched the strips with powdered PA to observe changes in the paper under UV light conditions (**Fig. 3.21C**). The fluorescence spectrum of BNOH-coated paper strips for detecting PA under 330nm excitation was observed. **Fig. 3.21A** illustrates that with escalating PA concentrations, the fluorescence emission of the paper sensor diminishes consistently, exhibiting a linear correlation within the 10-50 μg/mL range of PA concentrations (**Fig. 3.21B**). where the part of the paper that was in contact with PA reduced the fluorescence significantly, forming a clear contrast with the unreacted part. Since explosives often leave traces on clothing and bags, we also tested the performance of the strip-based sensor on trace amounts of solid PA. **(Fig. 3.21D)** We dropped different concentrations of PA solution onto a glass plate and dried it in a fume hood before wiping it with the paper-based sensor and observing under UV light. A quenched spot was clearly observed in the area of the strip that reacted with PA, highlighting the potential of this approach in detecting traces of solid PA.

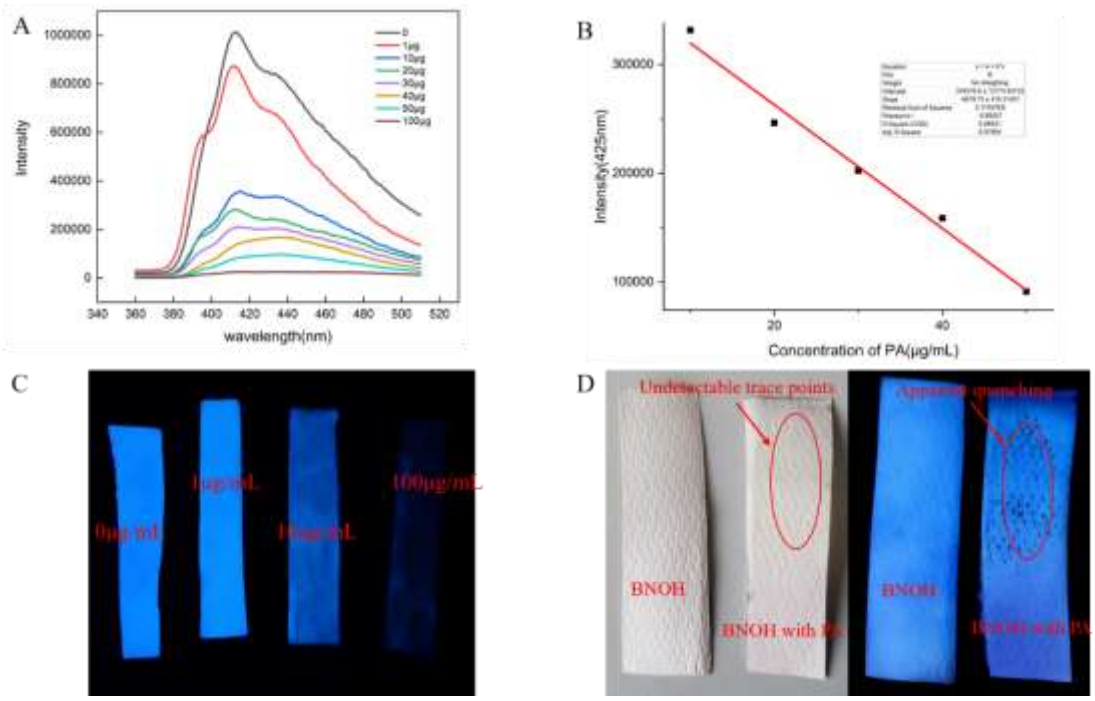

Fig. 3.21. (A) Emission of BNOH paper stripes to detect PA in different concentrations. (B)Linearity of fluorescence intensity at 425 nm with PA concentration (10-50μg/mL) for BNOH paper sensor. (C)Photo of BNOH paper stripes to detect PA in different concentrations solution of PA under UV irradiation. (D) and solid PA under sunlight(left) or UV irradiation(right).

3.4. Conclusion

In summary, we have synthesized and tested a fluorescent probe (BNOH) containing B-N bond and hydroxyl group for sensing the explosive picric acid. In aqueous environments, the probe produces a bright fluorescence caused by the AIE effect. The interaction between the BNOH aggregates and PA significantly quenches the emission with a high selectivity and sensitivity. The quenching results from the formation of a 1:1 adduct between BNOH and PA, stabilized by π-π stacking and generates photoinduced charge transfer upon light excitation, as demonstrated by DFT calculation. To preliminarily demonstrate the potential of this probe "on-field", solid paper strips where pre-treated with BNOH and exposed to light after contact with the analyte, demonstrating an excellent sensitivity to detect PA both in solution and as powder. The results herein presented highlight the great potential of this probe for electronic sensing in real explosives, water pollutants, soil sensors, etc., playing a positive role in homeland security

and explosive detection.

Chapter 4 Development of a versatile optical pH sensor array for discrimination of anti-aging face creams

Abstract

The authentication of cosmetic products has always been a prominent concern. Here, we have developed a pH sensor and applied it in the field of cosmetic safety. Initially, we designed two probes, CH with aggregation-induced emission (AIE) effect and the near-infrared fluorophore derivative CYTYR. By encapsulating them with DSPE-PEG2000-NH2, we obtained the CYCH nano-micelles with fluorescence resonance energy transfer (FRET) response. By combining them into a sensor array called pC, we achieved sensitive detection of a wide pH range, ranging from 5.25 to 9.05. To validate the performance of the pC sensor array, we employed a multi-channel mode and applied it to differentiate commercial anti-aging creams. Through linear discriminant analysis and 3D fingerprint analysis, the pC sensor array successfully distinguished anti-aging creams from different countries, providing a rapid and accurate method for cosmetic safety identification. The results of this study demonstrate the potential of the pC sensor array for quick authentication of cosmetic products, offering significant support and application prospects in safeguarding consumer health.

Key words: Cosmetic products; pH sensor; Fluorescence resonance energy transfer (FRET); Anti-aging creams; Consumer health

4.1 introduction

Anti-aging products are becoming increasingly popular in the market.[182] Recently, with the increasing level of globalization, the phenomenon of counterfeit cosmetics has become more prevalent.[183-185] Some manufacturers, driven by profit, produce and sell counterfeit and inferior products. One of the most common types of fraud is the adulteration of products claiming to be natural, often by adding cheaper ingredients and harmful chemicals (such as industrial-grade glycerin) along with other additives.[186-190] Another deceptive practice involves counterfeiting and labeling low-quality and inexpensive anti-aging products with expensive brand names, or producing the same product with different prices on the same production line. The fight against cosmetic fraud is becoming increasingly important.

The pH value plays a crucial role in cosmetics, especially in anti-aging creams, where it is

considered an essential factor. [191, 192]The pH value of a cream is crucial for its efficacy, stability, and compatibility with the skin. Anti-aging creams offer various benefits to humans, such as reducing wrinkles, increasing skin elasticity, and enhancing skin radiance, thereby keeping the skin youthful. These results are closely related to the pH environment of the cream. Typically, the pH range of anti-aging creams falls between 5 and 8, which is close to the natural acid-alkaline balance of the skin.[193-195] A correct pH value helps the active ingredients in the cream to exert their optimal effects. For example, many anti-aging ingredients, such as antioxidants and peptides, are vital for maintaining the youthful state of the skin. However, these active ingredients remain stable within a specific pH range. By precisely controlling the pH value of the cream, the stability of these active ingredients can be ensured, thereby providing the best anti-aging effects. Furthermore, the pH value of the cream also affects the compatibility with the skin. The pH value of the skin is typically maintained around 5.5, which is slightly acidic[196]. Creams that have a pH value similar to that of the skin are more easily absorbed and cause less irritation and discomfort. This is particularly important for individuals with sensitive skin. If the pH value of the cream is too high or too low, it may damage the skin barrier, leading to dryness, irritation, and discomfort. Therefore, ensuring an optimal pH value of anti-aging creams can maintain the skin in healthy condition and maximize the benefits of anti-aging products.[182, 188]

Fluorescent sensing arrays, often referred to as "artificial noses," excel in substance identification. These sensors manifest distinct luminescent characteristics when exposed to various substances, enabling swift and accurate identification through linear discrimination. Their applications span a broad spectrum, demonstrating remarkable proficiency in discerning drugs[197], explosives[180], and vapors within the realm of hazardous materials. Environmental applications showcase effective differentiation of minerals[198] and organics in water resources[199]. In the realm of food safety, these arrays have successfully identified complex mixtures, including the nuanced aroma of coffee[200]. Notably, while fluorescent sensing arrays have found diverse applications, their utilization in evaluating skin care products remains an unexplored domain.

Over the past few decades, various methods for identifying counterfeit cosmetics have been

developed, including mass spectrometry, ultraviolet-visible (UV-vis) spectroscopy, infrared (IR) spectroscopy, and gas chromatography. [201-205]Although these techniques have been proven to be successful to some extent, certain drawbacks, such as expensive equipment and preliminary procedures for sample purification, hinder their widespread application in rapid identification. [206-213] Therefore, there is a need for the development of simple and rapid methods for discerning the authenticity and quality of cosmetics.

4.2 Experiment

4.2.1 Materials and methods

Unless otherwise specified, materials were obtained from Sigma-Aldrich and used without further purification. DSPE-PEG2000-NH2 (25 mg/mL in chloroform solution) was purchased from Sigma. Deionized water was obtained by Milli-Q water purification system (Millipore) with electrical conductivity of 18.2 s/m. Using tetramethylsilane (TMS) as the internal standard, 1H and 13C NMR spectra were recorded on 14 T Bruker Avance III spectrometer. Mass spectra were recorded on the Brook Electron spray Ionization Mass Spectrometer (ESI-MS). The UV-Vis absorption spectrum was collected by CARY50 biological spectrophotometer (Varian Inc., CA., USA). Fluorescence spectra were measured on Fluoromax-4 fluorescence spectrophotometer (HoribaJobinYvon Inc., USA). Spectra were recorded at 25 °C, with excitation and emission slits of 3 nm. The 8 anti-aging creams used in this study were unopened samples provided by the manufacturers at the time of purchase. All samples were within their expiration dates, ensuring their freshness and effectiveness.

4.2.2 Synthesis of CH

Compound CH was synthesized using a method described in previously published literature.[40] Under argon gas protection, compound **1,** 2-(3,5,5-trimethylcyclohex-2-en-1-ylidene)malononitrile (0.2 g, 1.07 mmol) and 4-hydroxybenzaldehyde (**2**, 0.22 g, 1.5 mmol) were dissolved in 3 mL acetonitrile. Then piperidine (0.5 mL, 5.06 mmol) was added to the solution and the mixture was heated to reflux at 85°C for 16 h. The reaction was monitored until reactant **1** disappeared. Subsequently, the solution was extracted using ethyl acetate (3 × 25 mL) and water. The organic layer was washed with 1 N HCl (30 mL) and saturated salt water, before being dried with anhydrous sodium sulfate to obtain red crude solid. Column

chromatography separation (dichloromethane: methanol = 60:1 to 10:1) resulted in 162 mg (orange solid) with a yield of 51%.^{1}H NMR (600 MHz, DMSO-d_6) δ 8.10 (s, 2H), 7.81 (d, J = 7.6 Hz, 2H), 7.66 (d, J = 7.7 Hz, 2H), 7.47 (d, J = 16.1 Hz, 1H), 7.28 (d, J = 16.2 Hz, 1H), 6.92 (s, 1H), 2.63 (s, 2H), 2.56 (s, 2H), 1.01 (s, 6H)., ^{13}C NMR (151 MHz, DMSO) δ 170.96, 156.33, 138.08, 137.96, 135.16, 130.59, 127.37, 123.63, 114.42, 113.59, 77.15, 42.91, 40.65, 40.53, 40.39, 40.26, 40.12, 39.98, 39.84, 39.70, 38.74, 32.27, 28.02, 27.65. MS (ESI): calculated for $C_{19}H_{19}BN_2O_2$ $[M+H]^+$: 318.15, found 318.15.

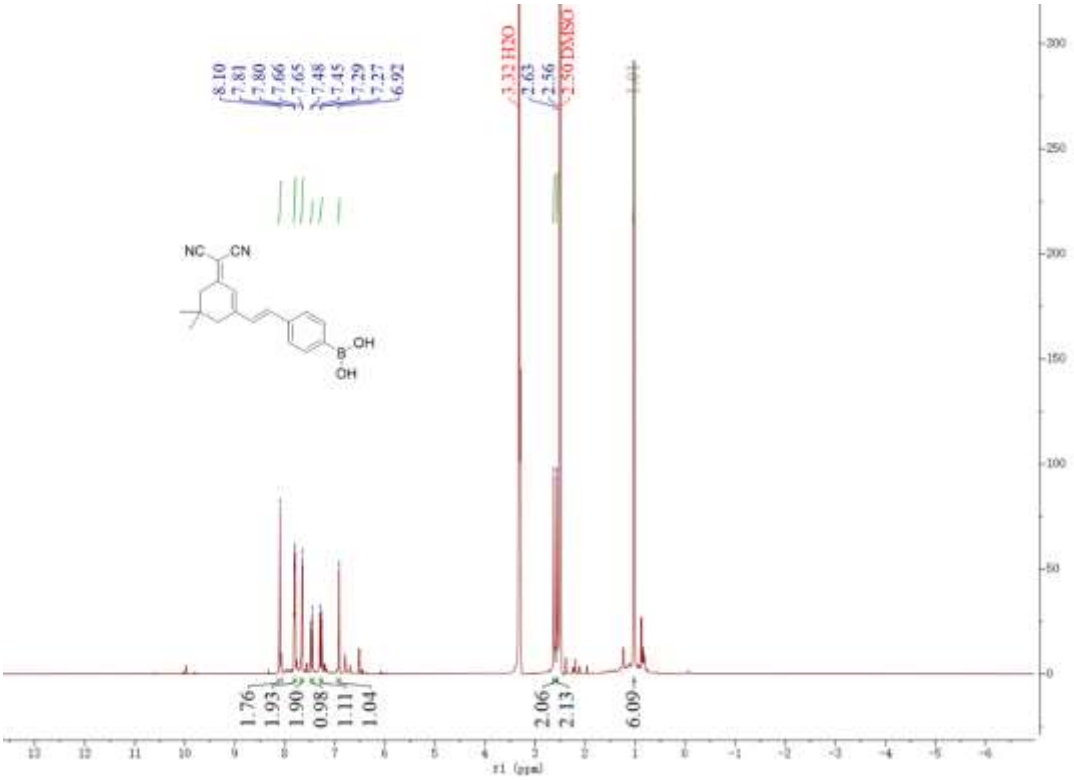

Fig. 4.1. ^{1}H NMR spectrum of CH in deuterated DMSO.

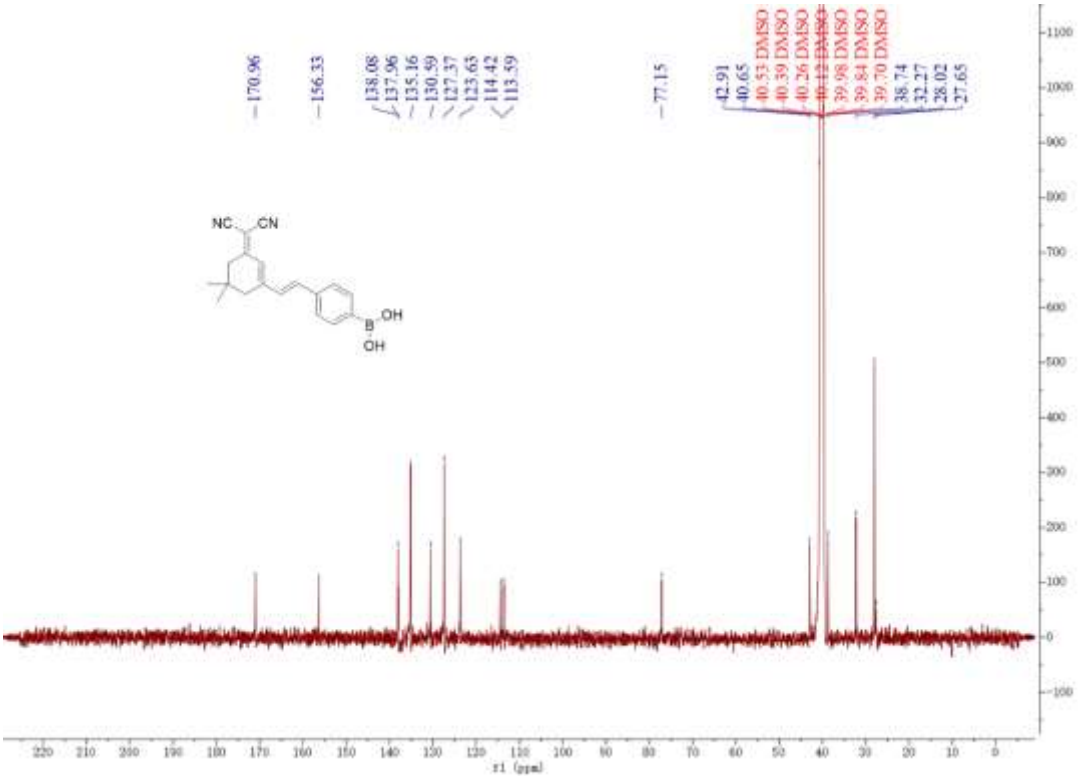

Fig. 4.2. ^{13}C NMR spectrum of CH in deuterated DMSO

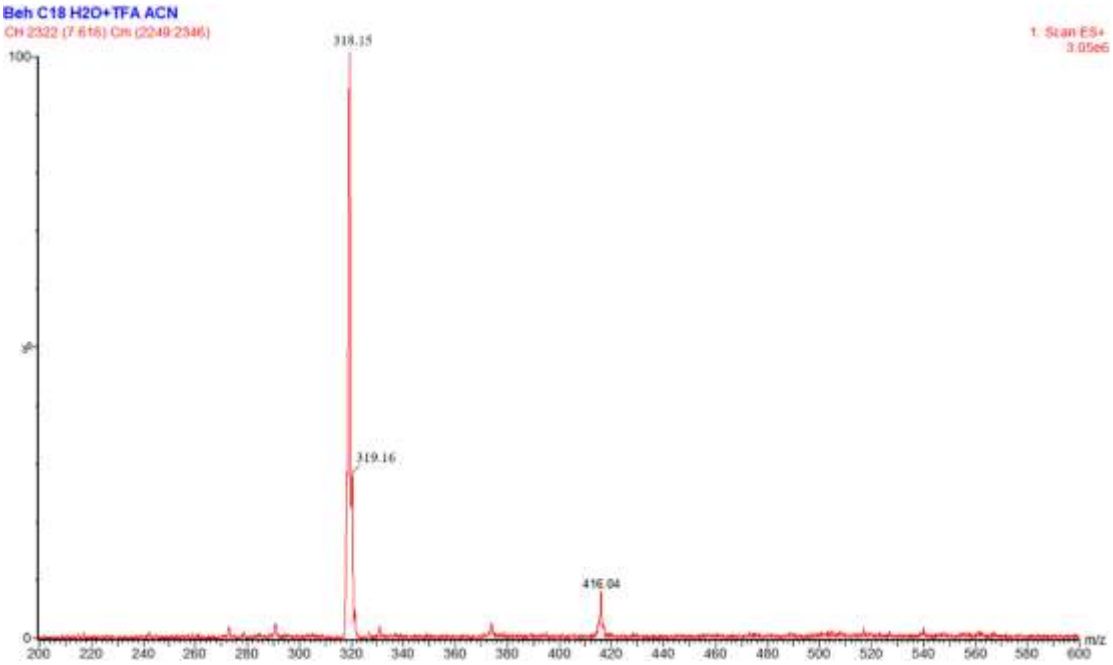

Fig. 4.3. Mass spectrum of CH.

4.2.3 Synthesis of CYTYR

CYTYR was synthesized in a one-step reaction from IR783(2-[2-[2-Chloro-3-[2-[1,3-dihydro-3,3-dimethyl-1-(4-sulfobutyl)-2H-indol-2-ylidene]-ethylidene]-1-cyclohexen-1-yl]-

ethenyl]-3,3-dimethyl-1-(4-sulfobutyl)-3H-indolium hydroxide). IR783 and tyramine (**3)** were dissolved in 1 mL of DMF and reacted at 85°C for 3 hours. The solvent was then removed by vacuum distillation. Column chromatography separation (dichloromethane: methanol = 3:1 to 1:1) resulted in 36 mg blue solid with a yield of 61%.^{1}H NMR (600 MHz, Methanol-d_4) δ 7.68 – 7.61 (m, 2H), 7.35 (d, J = 7.4 Hz, 2H), 7.31 (t, J = 7.8 Hz, 2H), 7.09 (qd, J = 7.2, 4.7, 2.8 Hz, 8H), 6.78 (dd, J = 16.2, 8.0 Hz, 4H), 4.05 (t, J = 6.8 Hz, 2H), 3.98 (d, J = 6.9 Hz, 4H), 3.01 (d, J = 9.8 Hz, 4H), 2.89 (q, J = 7.3 Hz, 8H), 2.51 (t, J = 6.5 Hz, 4H), 1.75 (p, J = 7.9, 7.1 Hz, 2H), 1.61 (s, 12H), 1.32 (d, J = 13.7 Hz, 2H).^{13}C NMR (151 MHz, MeOD) δ 169.85, 165.81, 158.33, 145.46, 142.23, 140.38, 133.33, 132.20, 131.72, 131.65, 130.79, 130.55, 130.34, 129.29, 124.77, 123.91, 122.80, 117.67, 117.62, 111.07, 96.71, 70.05, 53.24, 52.99, 50.35, 50.21, 50.07, 49.92, 49.78, 49.64, 49.50, 44.68, 43.17, 41.12, 38.17, 37.87, 34.72, 32.56, 31.06, 30.03, 27.68, 27.10, 25.89, 25.56, 24.94, 24.60, 23.55, 15.31, 12.32. MS (ESI): calculated for $C_{46}H_{56}N_3O_7S_2^-$ $[M+H]^+$: 826.36, found 826.19.

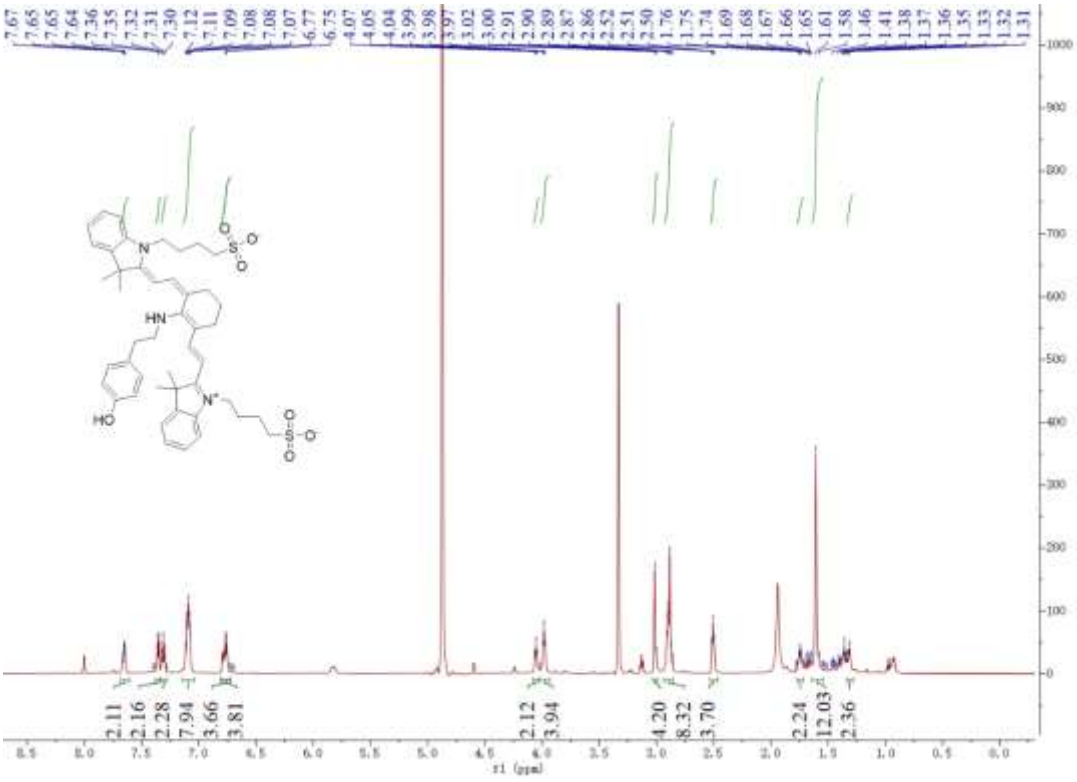

Fig. 4.4. ^{1}H NMR spectrum of CYTYR in deuterated methanol

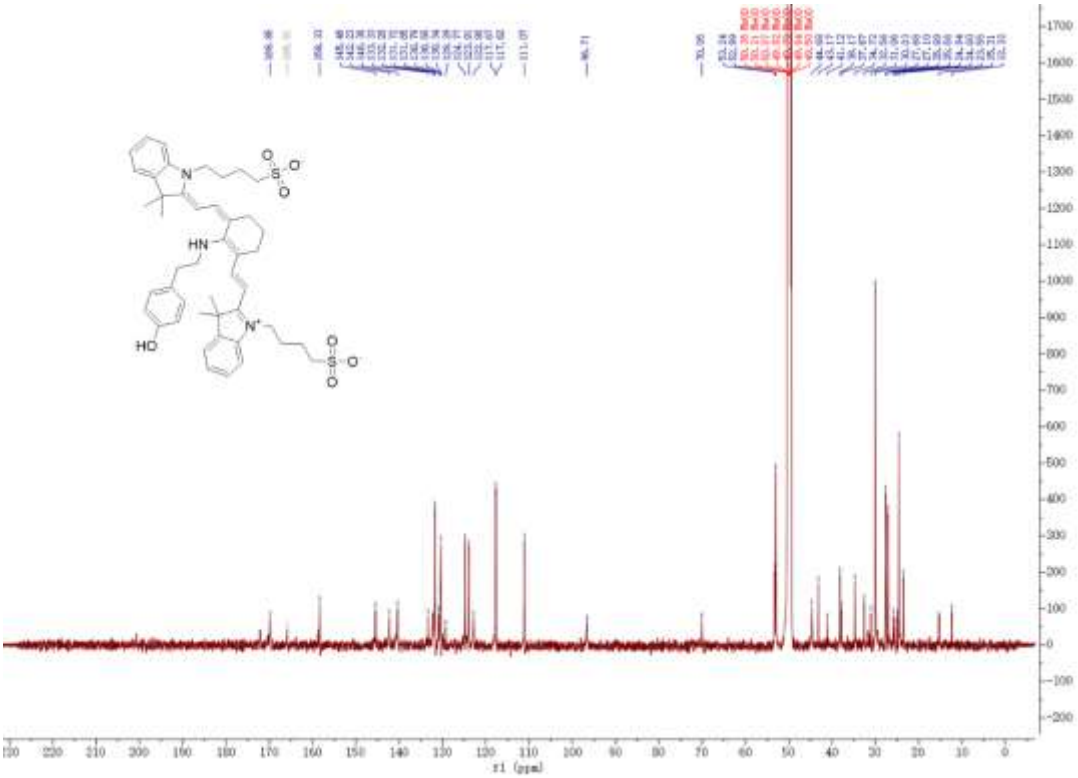

Fig. 4.5. ^{13}C NMR spectrum of CYTYR in deuterated methanol

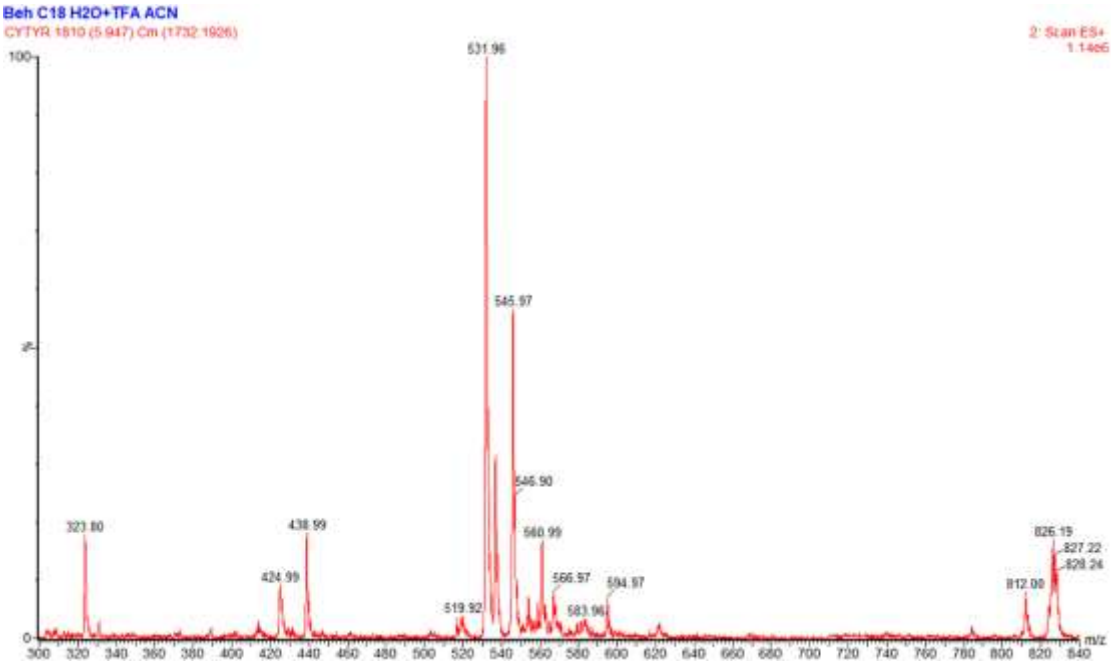

Fig. 4.6. Mass spectrum of CYTYR

4.2.4 Preparation of phospholipid-based sensors

CH-lipo and CYTYR-lipo sensors were prepared using the modified film hydration technique. Initially, CH was dissolved in THF and CYTYR was dissolved in methanol to create a stock solution with a concentration of 1 mM for both chemicals. A mixture of 0.01 mL CH or CYTYR

(10 μmol) from the stock solution and 0.03 mL of DSPE-PEG2000-NH_2 (25 mg/mL in $CHCl_3$) was prepared at a mass ratio of approximately 1:100. The organic solvent was then removed using vacuum rotary evaporation, resulting in a dry lipid film containing the dye. The dried film was hydrated with 1 mL of deionized water and sonicated for 1 minute to obtain a clear stock solution of the two sensors with a dye concentration of 20 μM, which was used for absorbance and emission measurements.

For the CHCY-lipo sensor, the following general methods were employed. CH and CYTYR stock solutions were mixed at a molar ratio of 1:10 (10 μL CH 1 mM in THF + 100 μL CYTYR 1 mM in MeOH) and combined with DSPE-PEG2000-NH_2 (25 mg/mL in $CHCl_3$) at a mass ratio of approximately 1:15. The organic solvent was then removed by vacuum rotary evaporation, resulting in a dry lipid film containing the dyes. The dried film was hydrated with 1 mL of deionized water and subjected to sonication for 1 minute to obtain a clear stock solution of sensors with a CH/CYTYR dye concentrations of 10 μM/100 μM. To prepare the test sensors solution, 0.2 mL of the stock sensors solution was mixed with different pH buffers (0.8 mL), resulting in a test sensors solution with a CH/CYTYR dye concentrations of 2 μM/20 μM for absorbance and emission measurements. Other CHCY-lipo sensors were prepared differing in the CH/CYTYR molar ratios: 1:1, 1:4, 1:6 and 1:8.

4.2.5 FRET efficiency

The efficiency of FRET effect (E) was calculated according to the following equation:

$$E=1-(F_{DA}/F_D) \quad \text{S4.1}$$

where FDA is the fluorescence intensity of the donor (CH) in the presence of the acceptor (CYTYR), and FD is the fluorescence intensity of the donor in the absence of the acceptor.

.

4.2.6 Assessment of pH responsiveness of the sensors

Using CH as a typical example, the probes were incubated with various ionic solutions at a concentration of 10 mM. The fluorescence spectra were measured to evaluate the response reliability. The $ONOO^-$ was prepared using the method described in the published literature.[44]

A buffer solution (10 mM) was prepared by dissolving citric acid and sodium citrate in water to test a broad pH range from 2.0 to 11.0. CH-lipo, CYTYR-lipo, and CHCY-lipo were added

to the appropriate pH buffer solutions to obtain a concentration of fluorescent dyes of 20 μM. Fluorescence readout were recorded using a Microplate reader using the following excitation and emission wavelengths:

CH-lipo: Excitation at 500 nm, Emission at 650 nm.

CYTYR-lipo: Excitation at 645 nm, Emission at 760 nm.

CHCY-lipo: Excitation at 500 nm, Emission at 760 nm..

4.2.7 pC to distinguish anti-aging creams

To obtain a 1 mg/mL solution, the 8 investigated face creams were dispersed in water. The resulting solutions were then distributed evenly in a 96-well plate in a 8x3 arrangement. Next, the pH sensors were added to the wells, obtaining a solution with a concentration of 20 μM of fluorescent material. The plate was carefully handled to ensure proper mixing of the sensor with the face cream solution in each well. The plate was then placed in a microplate reader equipped with UV fluorescence detection capabilities. The reader was set to record the UV fluorescence data at the appropriate excitation and emission wavelengths for the sensors used. The test for the unknown cream was carried out similarly to the experiment above. The parameters of the six detection channels are：

Channel 1 and Channel 2 are for CH-lipo, Excitation at 500 nm, Emission at 650 nm.

Channel 3 and Channel 4 are for CYTYR-lipo, Excitation at 645 nm, Emission at 760 nm.

Channel 5 and Channel 6 are for CHCY-lipo, Excitation at 500 nm, Emission at 760 nm.

4.3 Result and Discuss

This work aimed at designing a fluorescence pH sensing array, named pC, capable of detecting pH in a broad range of values and testing it on commercially available anti-aging face creams. The pC array consisted of three nanosized components (CH-lipo CYTYR-lipo, and CHCY-lipo) based on CH and CYTYR dyes.

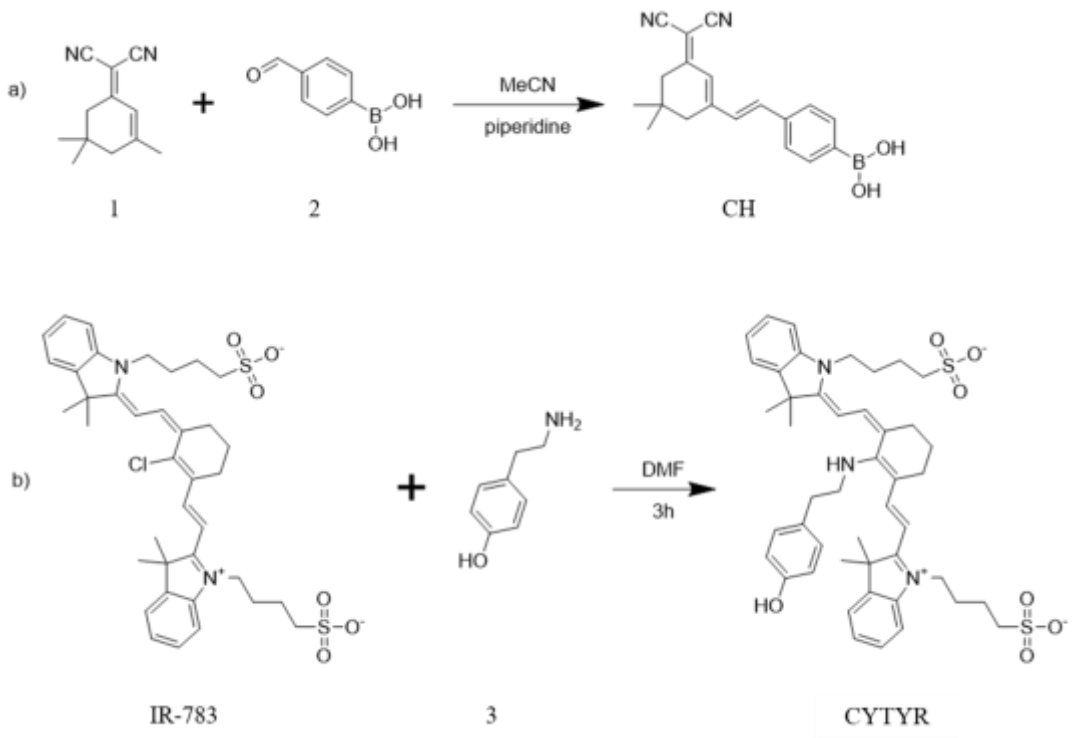

Fig. 4.7. Synthetic routes of CH (a) and CYTYR (b).

CH and CYTYR were synthesized through two simple synthetic steps (**Fig. 4.7**). CH molecule was obtained by the Knoevenagel condensation reaction of malononitrile-modified isoflurane and p-formylphenylboronic acid under argon protection, whereas CYTYR was synthesized with high yield by heating IR783 compound and tyramine in DMF. The choice of the two dyes was based on the expected pH dependence of their spectral properties.

Boronic acid moieties undergo deprotonation in alkaline solutions (pK_a 9-10), resulting in changes in their molecular properties, whereas malononitrile derivatives possess strong electron-withdrawing capabilities. On this basis, the connection between malononitrile and phenylboronic acid through a carbon-carbon double bond forms a large acceptor-acceptor (A-A) conjugated structure. However, under alkaline conditions, boronic acid undergoes deprotonation, and the molecular structure transforms into a donor-acceptor (D-A) system, leading to significant spectral changes. Although CH dye has been already reported in literatures, it has never been investigated as pH sensor.[214] The CYTYR dye was selected for the peculiar pH dependence of its spectral pattern, which is the result of the protonation of the meso-amino group, whose pK_a was reported to be in the 3-6 range,[35] thus extending the pH

detection range of the array to the acidic side. Moreover, the spectral properties of CH and CYTYR are very suitable to promote a FRET system, where CH acts as donor and CYTYR as acceptor.

To enable FRET mechanism and overcome the low water solubility of the dyes, CH and CYTYR were formulated, individually and in combination, with 1,2-distearoyl-sn-glycero-3-phosphoethanolamine (DSPE-PEG2000-NH2) to form nanomicelles in water,[215-217] which also improves the stability of the pC array. The absorption and fluorescence properties of CH-lipo, CYTYR-lipo, and CHCY-lipo can exhibit different and distinct pH profiles, and their combination enables a wide range of pH detection and discrimination. As energy acceptor, the tyrosine-modified cyanine dye CYTYR was considered. At low pH values, CH dye exhibits weak fluorescence, and its emission wavelength does not match the absorption of CYTYR, resulting in no FRET effect. However, when pH increases, CH undergoes deprotonation, resulting in a red shifted emission and FRET coupling with the CYTYR acceptor. Therefore, the combination of the spectral features these dyes may allow the extension of the pH sensing region across both acidic and alkaline regions, in the 4.7-9.2 range (**Fig. 4.8**).

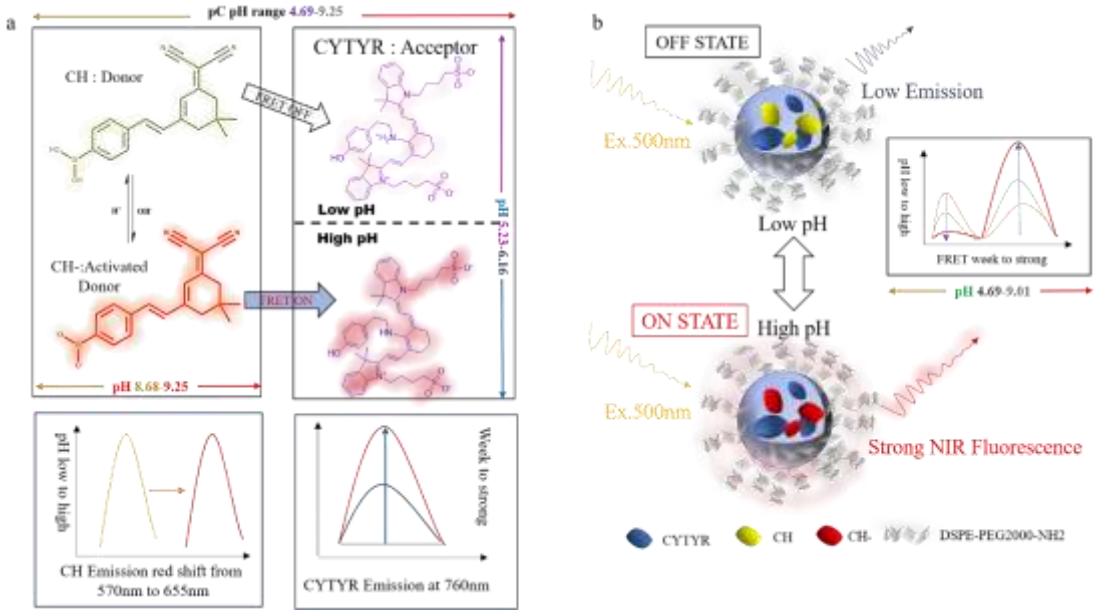

Fig. 4.8. a) Chemical structures of the pre-donor CH, donor CH-, and pH-activated acceptor CYTYR. b) Illustration of the pH response of CHCY

.

First, the spectral characteristics of CH and CYTYR dyes were evaluated in THF and methanol, respectively (**Fig. 4.9**). The maximum absorption and emission wavelengths pairs were 400/490 nm for CH, and 645/760 nm for CYTYR.

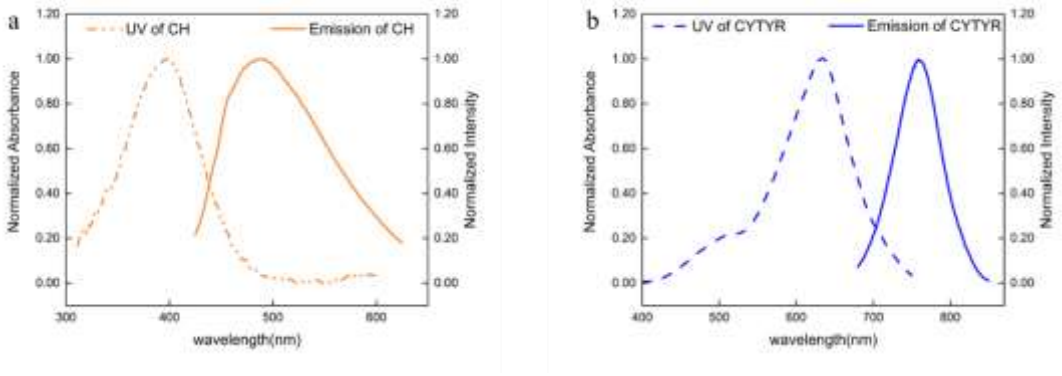

Fig. 4.9. a) Normalized UV and fluorescence spectra of CH in THF solution. b) Normalized UV and fluorescence spectra of CYTYR in methanol

Interestingly, under alkaline conditions (pH 11), CH deprotonated with a consequent red shift of the absorption/emission pair and increase of the Stokes shift (450 nm/650 nm). Interestingly, in this condition the emission wavelength of the deprotonated CH dye matched well the absorption of CYTYR dye, thus enabling an energy transfer (**Fig. 4.8a, Fig. 4.10**). CH and CYTYR dyes also exhibited a solvent-dependent fluorescence (**Fig. 4.11**).

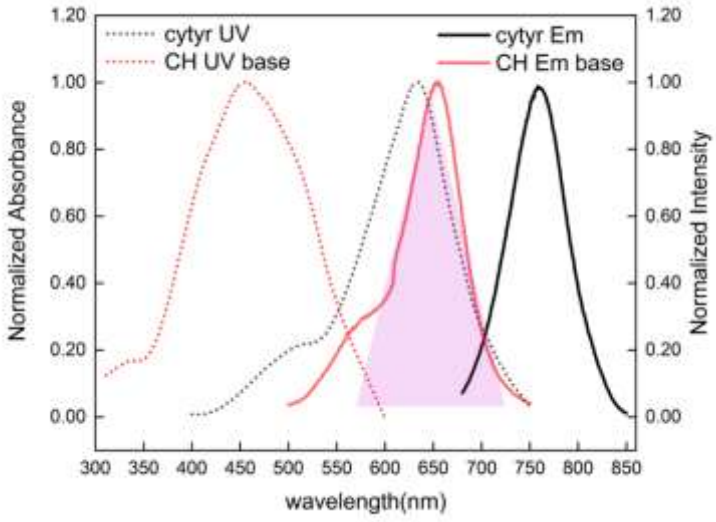

Fig. 4.10. Normalized UV and fluorescence spectra of CH and CYTYR in pH 11 buffer

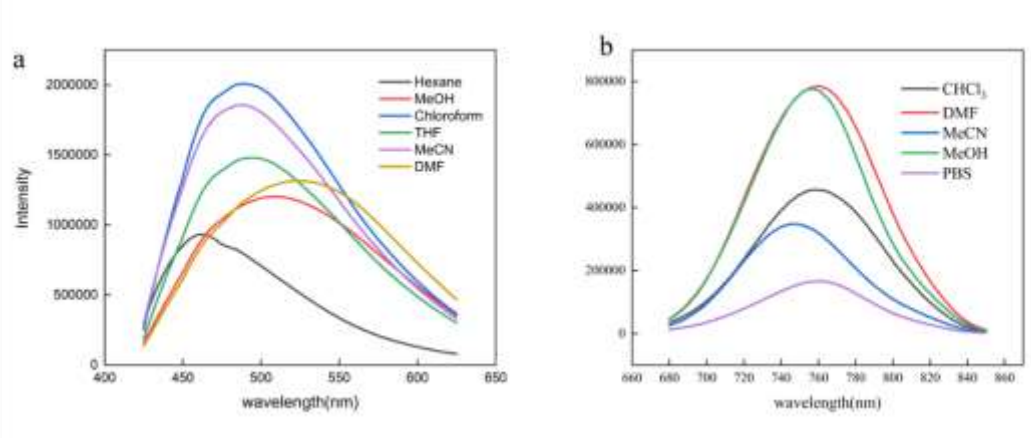

Fig. 4.11. a) Fluorescence emission curves of CH in different organic solvents. b) Fluorescence emission curves of CYTYR in different organic solvents

Compared to THF, the emission of CH was reduced in hexane (associated with a blue shift), in methanol and DMF (associated with a red shift in both solvents) and increased in acetonitrile and chloroform. Compared to methanol, the fluorescence intensity of CYTYR was reduced in acetonitrile (blue shift) and chloroform (no shift) and was similar in DMF. All these observations are in good agreement with the solubility of the dyes in the different solvents and the effect of solvent polarity on the spectral pattern.

The concentration dependence of the fluorescence emission was determined for both the dyes. The emission of CH in THF showed a linear behavior up to a concentration around 10 μM, after which the fluorescence quenched and decreased for a concentration higher than 50 μM, likely due to collisional quenching effects (**Fig. 4.12**).

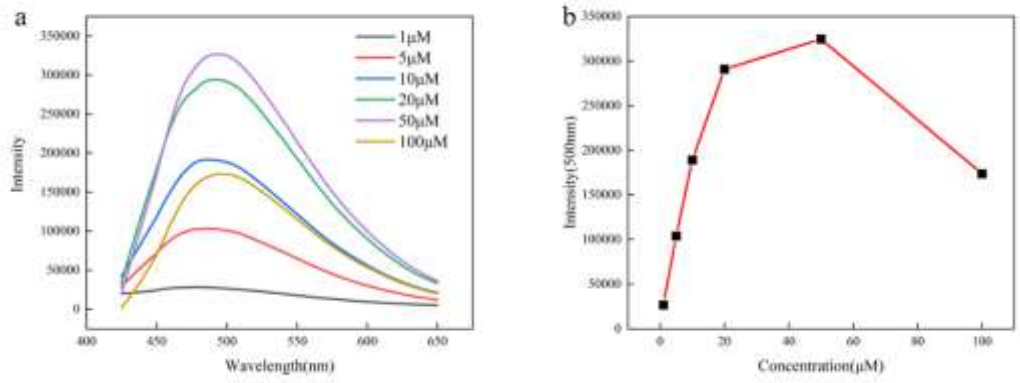

Fig. 4.12. a) Fluorescence emission spectra of different concentrations of CH in THF b) Fluorescence emission intensity of CH at 500nm as a function of concentration

Also the concentration dependence for CYTYR in methanol exhibited a linear correlation up to 10 μM, and a limited quenching at higher concentrations (**Fig. 4.13**).

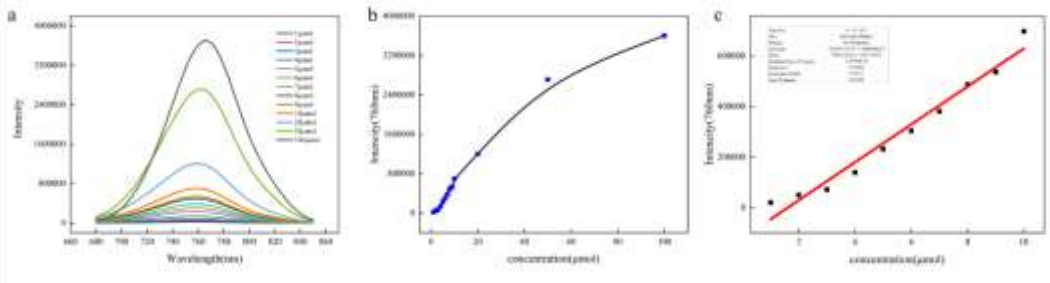

Fig. 4.13. a) Fluorescence emission spectra of different concentrations of CYTYR in methanol. b) Fluorescence emission intensity of CYTYR at 760nm as a function of concentration

It is worth noting that upon addition of water in a 10 mM THF solution of CH, the typical pattern resulting from the occurrence of aggregation-induced emission (AIE) effects. In fact, upon increasing the water fraction, the emission of the dye at 500 nm progressively decreased with a consequent appearance of a redshift emission at 570 nm, which is the only emission detectable when the water fraction reached 98% (**Fig. 4.14a**).

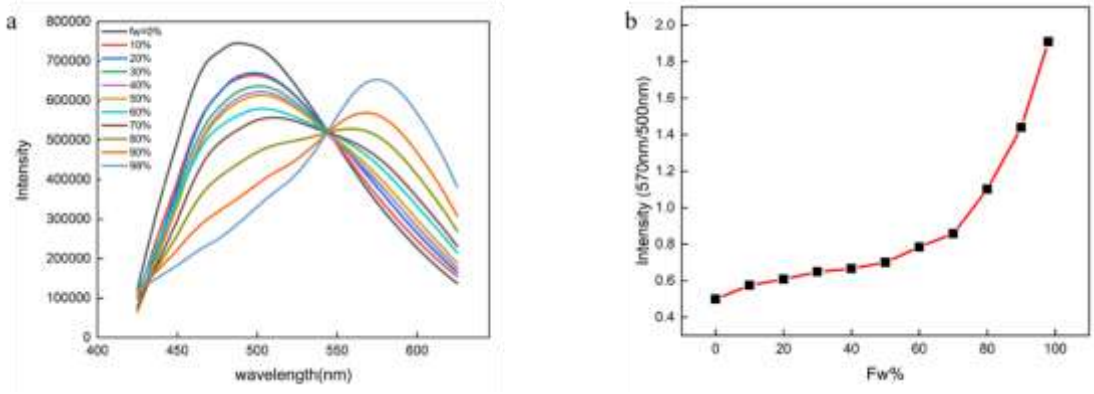

Fig. 4.14. a) Fluorescence emission curves of CH in THF solutions containing different proportions of water. b) The curve of the ratio of the fluorescence emission intensity at 570nm to 500nm as a function of the volume fraction of water in the solution

Plotting the fluorescence intensity 570/500 ratio, a steep increase of the red shift emission due to the AIE effect was detected water content larger than 70% (**Fig. 4.14b**).

To overcome the limited water solubility of the dyes and promote a pH dependent FRET mechanism, the CH/CYTYR pair were formulated in nanoaggregates using DSPE-PEG2000-NH_2 phospholipid (7.5 mol%) as surfactant (CHCY-lipo). Formulations containing the individual dyes CH (CH-lipo) and CYTYR (CYTYR-lipo) were also prepared.

The nanoparticle features of the formulations were evaluated by Dynamic Light Scattering measurements, which allowed the determination of the average hydrodynamic size, polydispersion index, and the zeta-potential of the aggregates at pH 4.4, 7.4, and 11.6 (Table 4.1).

Table 4.1. Dynamic light scattering particle size and Zeta potential of CH-lipo, CYTYR-lipo and CHCY-lipo in difference pH.

	pH	PDI	Size(nm)	Zeta-potential(mV)
CH-lipo	4.4	0.293	186	-7.57
CH-lipo	7.4	0.231	185	-1.47
CH-lipo	11.6	0.069	604	-36.1
CYTYR-lipo	4.4	0.315	298	-2.89
CYTYR-lipo	7.4	0.333	91	-3.79
CYTYR-lipo	11.6	0.261	203	-15.4
CHCY-lipo	4.4	0.473	326	2.61
CHCY-lipo	7.4	0.296	102	-9.52
CHCY-lipo	11.6	0.047	645	-35.4

The aggregates spanned a quite broad size range, from 90 nm to 600 nm, and size dispersion (0.05 to 0.5), without a clear dependence on pH and dye composition. As expected, the zeta-potential generally displayed high negative values at pH 11.6, and more positive values as pH decreased, likely reflecting the deprotonation of the terminal amino group of the phospholipid used in the formulation.

The mixed CHCY-lipo sample was also formulated as a function of the CH/CYTYR molar ratio

from 1:1 to 1:10. The emission spectra of these samples (excitation at 500 nm) at pH 11.6 are displayed in Figure 4.15. FRET effect started to be detectable in the formulation with the 1:4 molar ratio and reached the maximum efficiency (E = 96.4 %) for the 1:10 formulation.

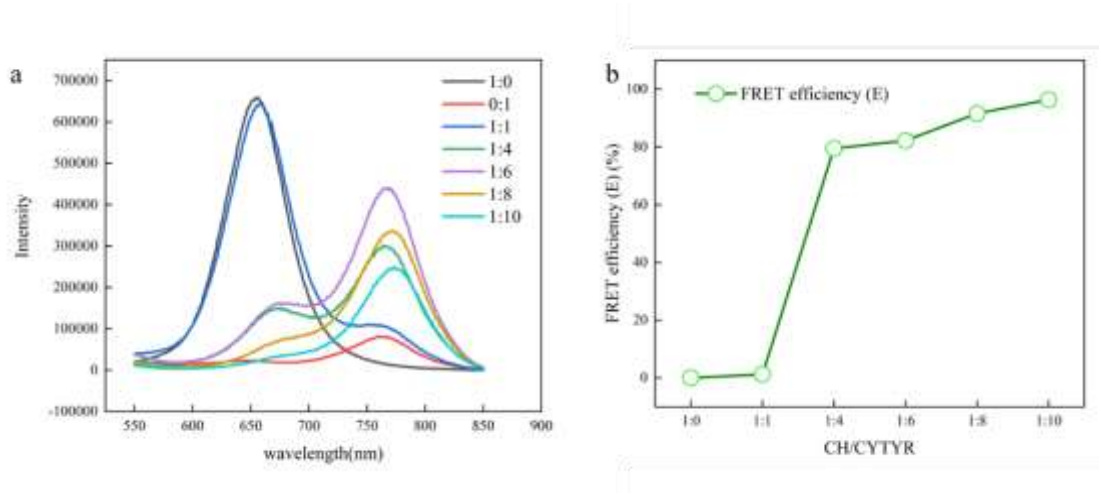

Fig. 4.15. a) Fluorescence emission curves of CH/CYTYR at different ratios. Excited by 500nm b) The FRET efficiency (E) with the ratio of probes

The FRET process is promoted by the incorporation of the dyes in the nanoaggregates and upon addition of TritonX-100 for disassembling the nanoparticles, the emission of the CH dye was recovered (**Fig. 4.16**).

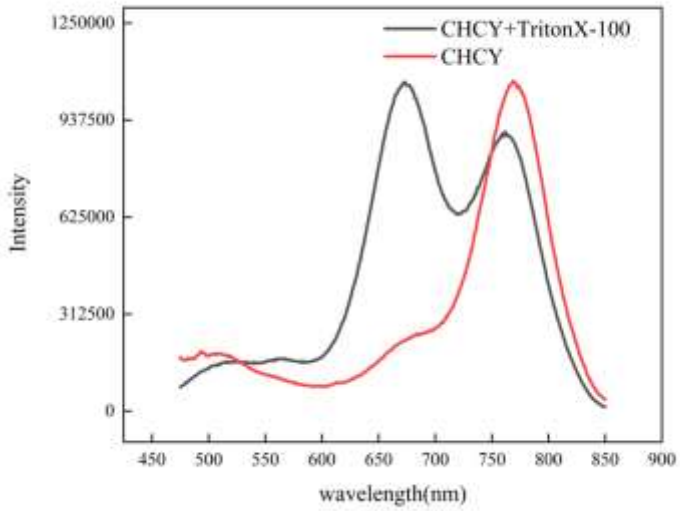

Fig. 4.16. Fluorescence emission curves of CHCY-lipo with and without Triton X-100

Next, the spectral properties and pH responsiveness of CH-lipo, CYTYR-lipo, and CHCY-lipo was assessed.

The absorption spectra of CH-lipo over the 2-10 pH range displayed a pattern fully consistent with the presence of an acid-base equilibrium with a maximum absorption around 410 nm at acidic pH and a broader red shifted signal around 500 nm at the basic side (**Fig. 4.17a**).

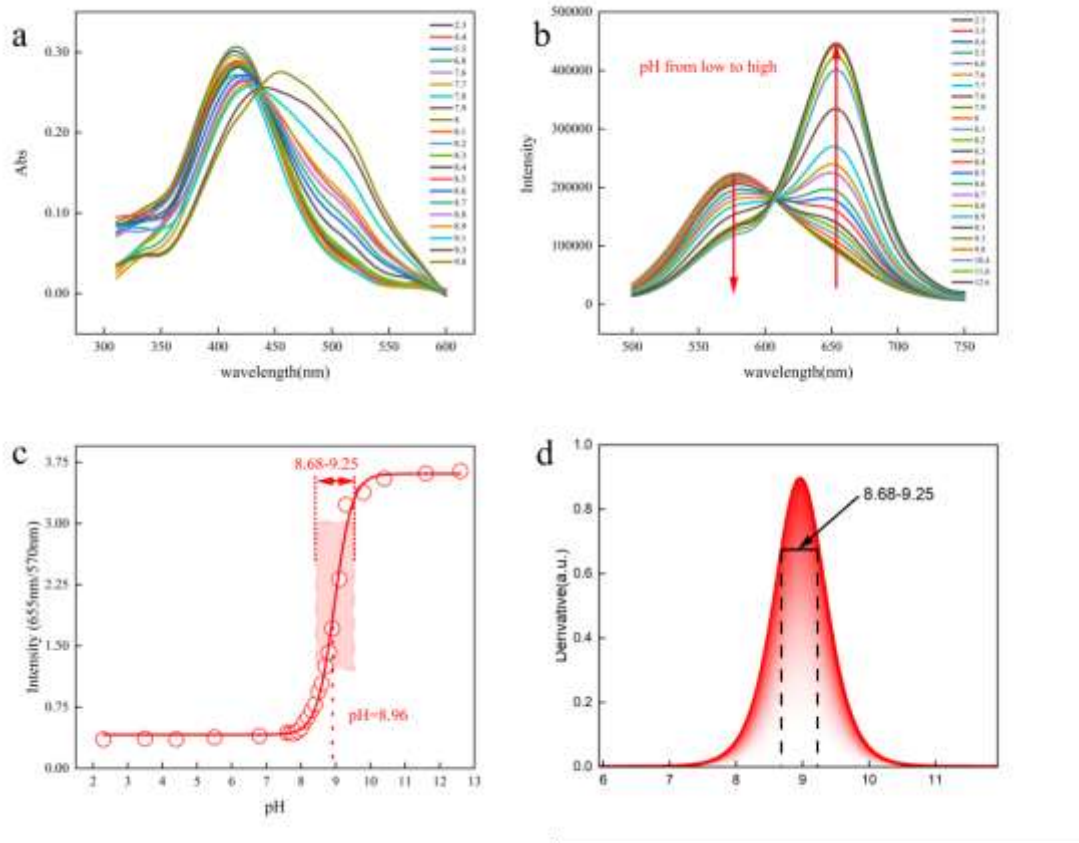

Fig. 4.17. a) UV absorption spectra of CH-lipo in different pH buffer solutions. b) Fluorescence emission spectra of **CH-lipo** in different pH buffer solutions at a concentration of 20 μM. Excitation wavelength: 500 nm, slit width: 3 nm. c) Sigmoidal Boltzmann function fitting curve of the ratio of fluorescence intensities at 655 nm and 570 nm as a function of pH. d) Derivative curve of the fitting function in Figure 1c, where 75% of the maximum value is taken as the pH-sensitive response range.

By plotting the pH dependence of the absorption 500/410 nm ratio, a clear inflection point at *ca.* pH 9 was observed, in agreement with the expected pK_a for a phenylboronic moiety (**Fig.**

4.18a). The fluorescence emission of CH-lipo (excitation at 500 nm) reflected the absorption pattern, with a signal at 570 nm for the protonated dye, and a red shifted emission at 655 nm for the deprotonated molecule (**Fig. 4.17b**). The values of the fluorescence intensity 655/570 ratio were fitted with an S-shaped Boltzmann function, and a pK_a values of 8.96 (in good agreement with the deprotonation of the phenylboronic acid moiety) was obtained from the inflection point (**Fig. 4.17c**). A pH detection range between 8.68 and 9.25 (ΔpH = 0.57) was determined for this system (**Fig. 4.17d, Fig.4.18b-c**).

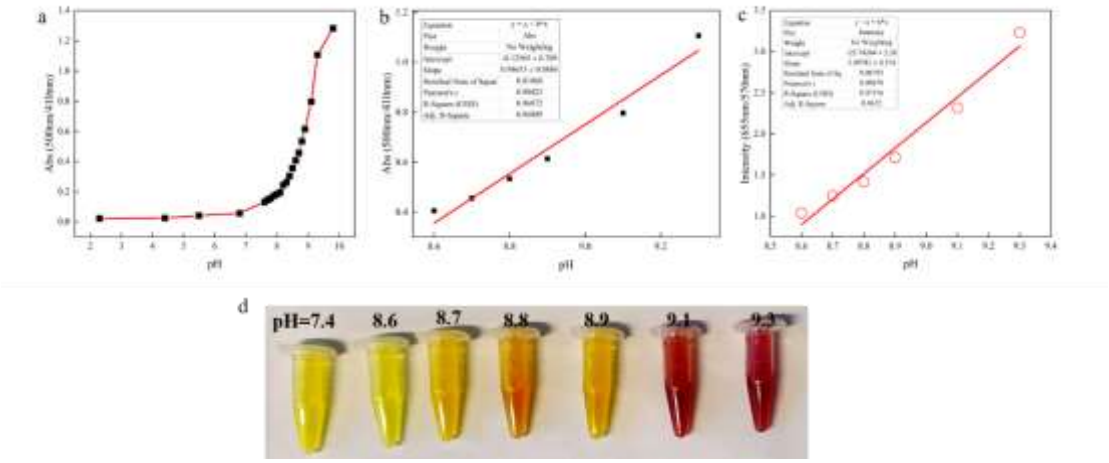

Fig. 4.18. a) 500nm/410nm UV intensity ratio versus pH. b) The linear relationship between the absorption intensity ratio and pH. c) The linear relationship between the emission intensity ratio and pH. d) Pictures of optical changes in pH from low to high (left to right) CYTYR-lipo

CYTYR-lipo sample exhibited a different behavior. In acidic environment, the dye displayed an absorption peak around 500 nm, whose intensity decreased under alkalization, while a red shifted absorption around 630 nm appeared and reached the maximum intensity at pH 7.8. The blue shifted absorption in acidic condition can attributed to the protonation of the amino group located at the *meso* position of the polymethine chain of the dye as already reported for other similar systems.[218, 219]Therefore, in neutral and alkaline conditions, the meso-amino group deprotonates, and the absorption spectrum displays the typical pattern associated with a cyanine dye (**Fig. 4.19a**). Similarly, the fluorescence emission (excitation at 645 nm) displayed a pH dependence in excellent agreement with the presence of acid/base pair with a pK_a of 5.7 (**Fig. 4.19b-d**). Consequently, the pH detection range of this system was found to be 5.23-6.16 (ΔpH

= 0.93)

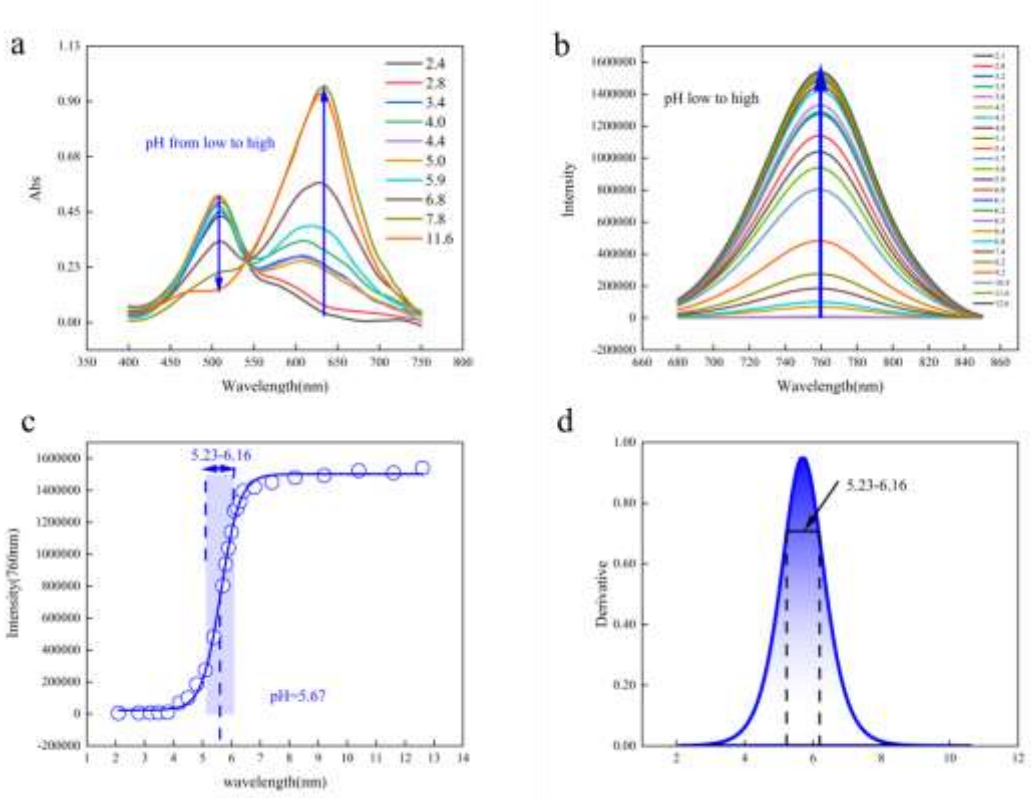

Fig. 4.19. a) UV absorption spectra of CYTYR in different pH buffer solutions. b) Fluorescence emission spectra of CYTYR-lipo in different pH buffer solutions at a concentration of 20 μM. Excitation wavelength: 645 nm, slit width: 3 nm. c) Sigmoidal Boltzmann function fitting curve of the ratio of fluorescence intensities at 760 nm as a function of pH. d) Derivative curve of the fitting function in Figure 2c, where 75% of the maximum value is taken as the pH-sensitive response range.

The spectral pattern of the mixed formulation CHCY-lipo (CH/CYTYR 1:10 molar ratio) is shown in **Fig. 4.20**.

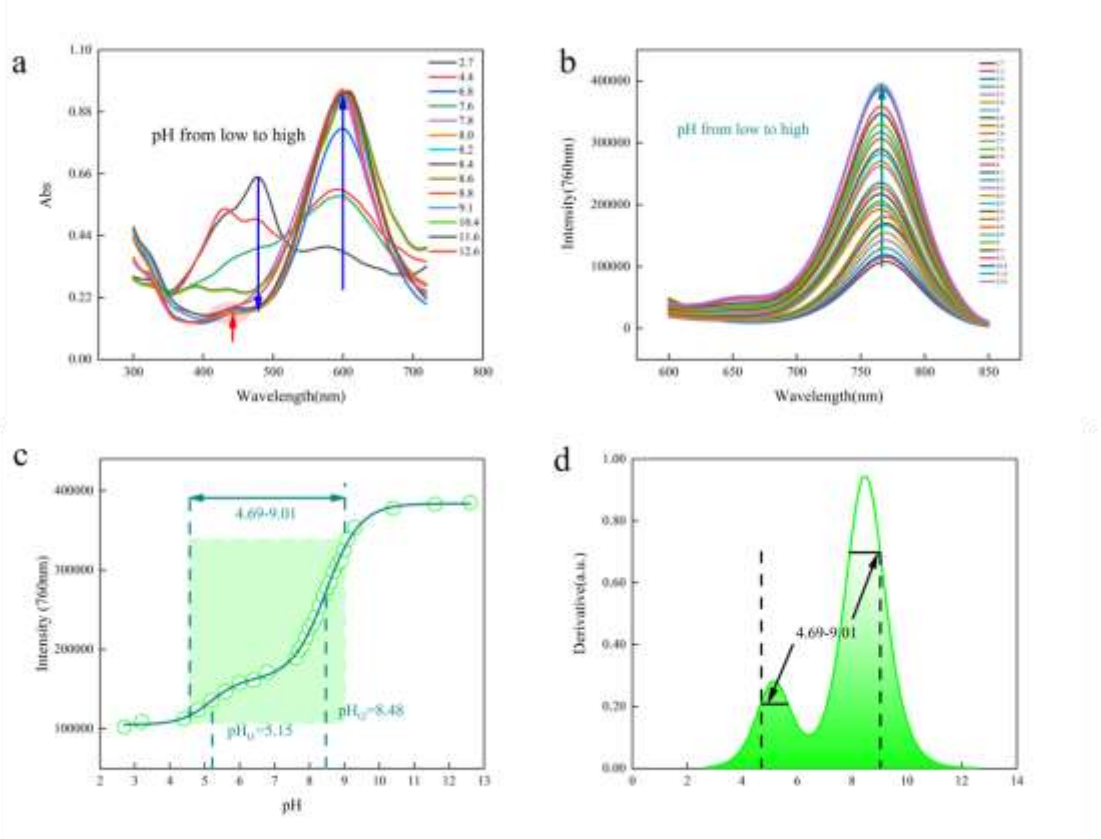

Fig. 4.20. a) UV absorption spectra of CHCY in different pH buffer solutions. b) Fluorescence emission spectra of CHCY-lipo in different pH buffer solutions at a concentration of 20 μM. Excitation wavelength: 500 nm, slit width: 3 nm. c) Sigmoidal double Boltzmann function fitting curve of the ratio of fluorescence intensities at 760 nm as a function of pH. d) Derivative curve of the fitting function in Figure 3c, where 75% of the maximum value is taken as the pH-sensitive response range.

The absorption spectra displayed a quite complex pattern in the 400-500 nm range with a general reduction in the signal intensity from acidic to alkaline environments, with an opposite signal intensity *vs.* pH trend in the spectral region around 600 nm. Alkaline conditions produced a new absorption peak at 450-500 nm (**Fig. 4.20a**). The emissive pattern of this sample (upon excitation at 500 nm) was predominantly characterized by a single emission at 760 nm arising from the CYTYR dye, whose intensity progressively increased over the 3-12 pH interval (**Fig. 4.20b-c**).

The combined effect (deprotonation of CYTYR + deprotonation of CH and resulting FRET

effect) of the two dyes in the nanoaggregates upon excitation at 500 nm allowed the extension of the pH responsiveness of this system that spanned over more than 4 pH units (4.69-9.01).

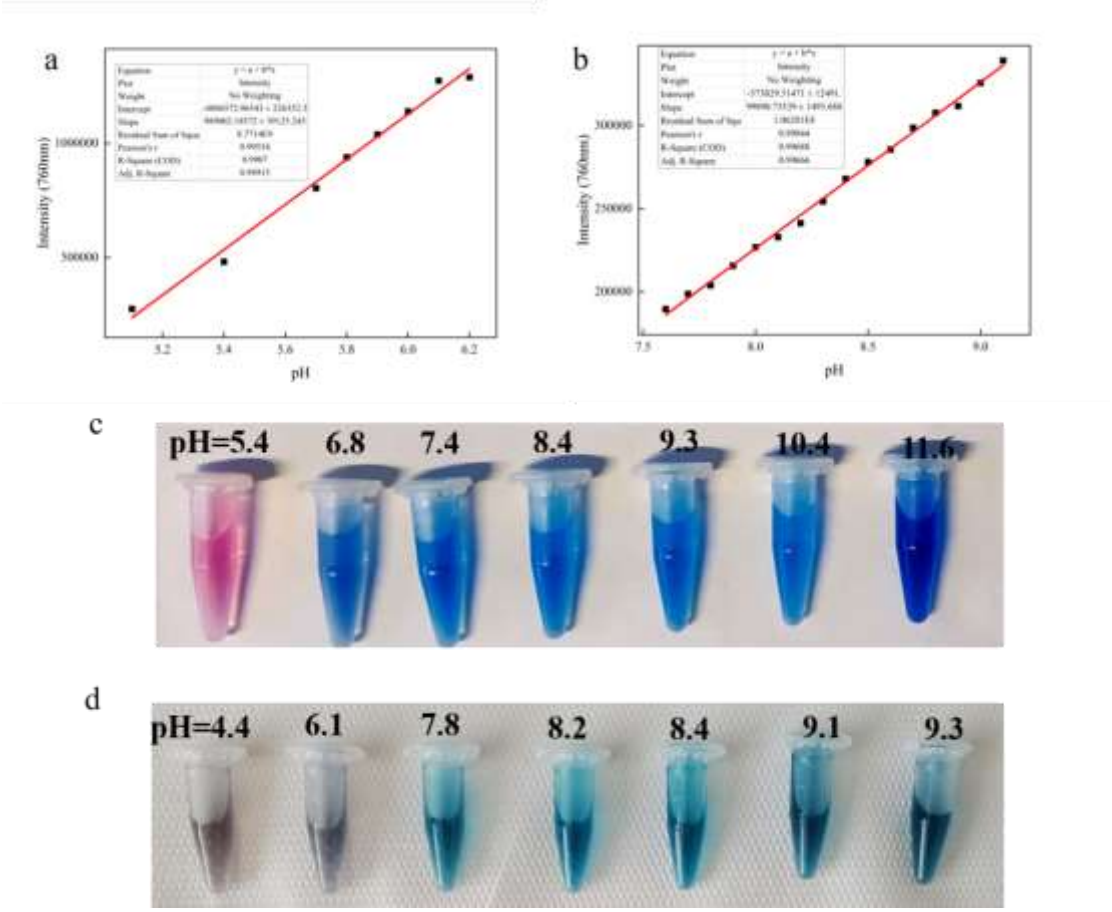

Fig. 4.21. a)The linear relationship of the fluorescence emission intensity of CYTYR-lipo at 760nm with pH 5.23-6.16. b)The linear relationship of the fluorescence emission intensity of CHCY-lipo at 760nm with pH 7.6-9.3. c) Pictures of optical changes in pH from low to high (left to right) CYTYR-lipo.d) Pictures of optical changes in pH from low to high (left to right) CHCY-lipo.

With the aim of assessing the potential of the nanoaggregates for pH sensing purposes of anti-aging creams, their photostability and possible interferences with metal ions were evaluated. CH-lipo exhibited excellent photostability during multiple acid-base cycles (pH 3.4 and 12.6), while CYTYR-lipo and CHCY-lipo showed a slight reduction in the fluorescence emission in the same challenge (**Fig. 4.22a-c**).

Concerning potential interference with the presence of metal ions, the results reported in **Fig.**

S11d demonstrate that the emission of the three systems is almost unaffected by the presence of nine metal ions selected for this experiment.

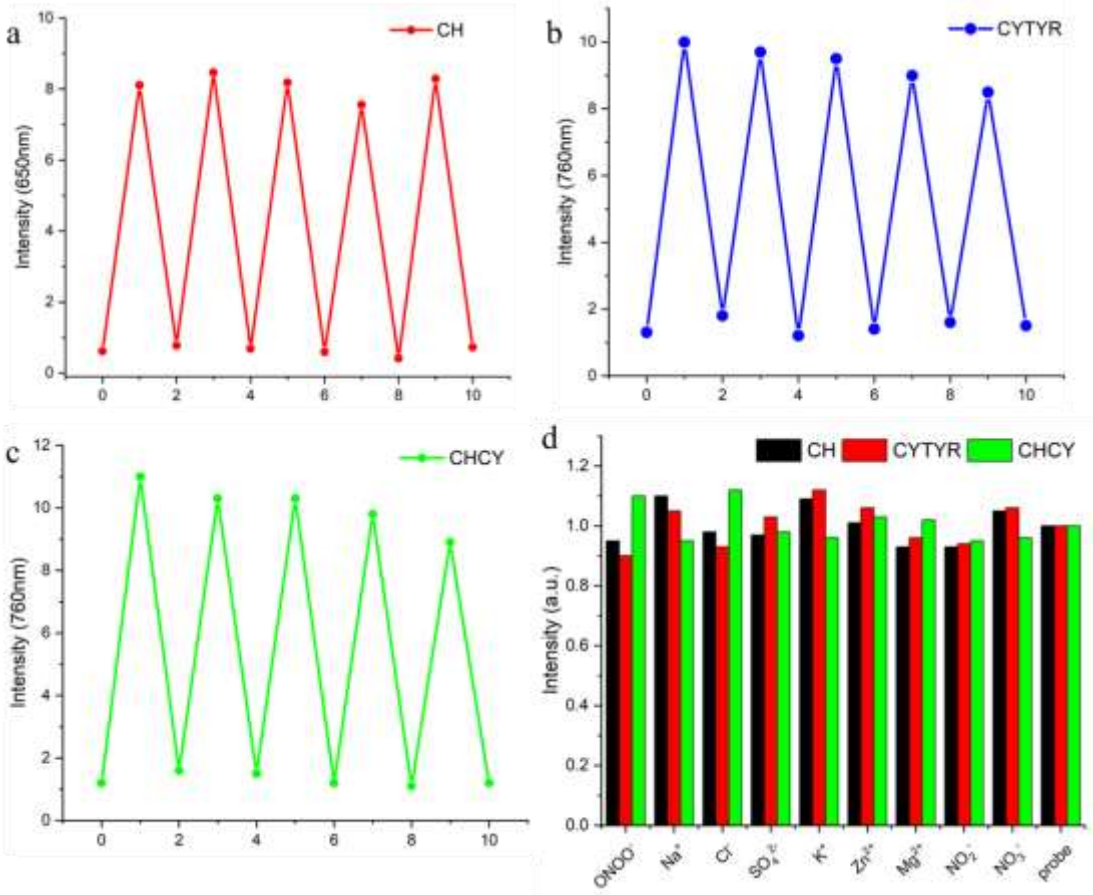

Fig. 4.22. Comparison curve of emission intensity of a) CH-lipo b) CYTYR-lipo and c) CHCY-lipo with multiple pH changes (pH 3.4-12.6) d) Comparison of fluorescence emission intensity after co-incubation of CH-lipo ,CYTYR-lipo and CHCY-lipo and ions

Based on these promising observations and the distinct pH sensing properties of CH-lipo, CYTYR-lipo, and CHCY-lipo, we established the pC pH sensing array (**Fig. 4.23**).

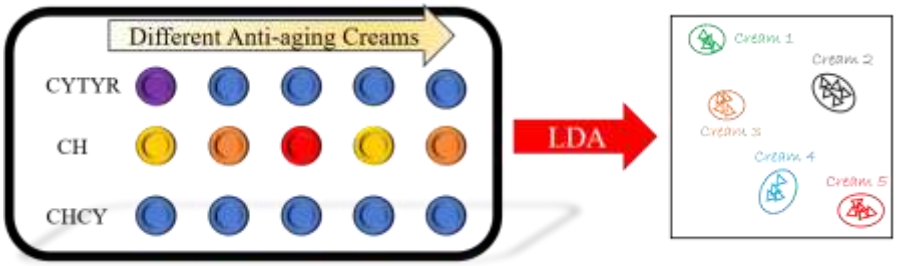

Fig. 4.23 Explanation of the application of the pC sensor array in differentiating various anti-

aging creams.

The sensing array was conceived with six channels utilizing the UV-vis absorption and fluorescence emission of CH-lipo, CYTYR-lipo, and CHCY-lipo for detection. Each probe was mixed with buffers at different pH values, and the final concentration of dyes was set to 20 μM. The absorption and fluorescence intensities were recorded after 3 minutes. As shown in **Fig. 4.24a**, pC array exhibited different quenching effects at the different examined pH values. The quenching ratio (calculated as $(I - I_0)/I_0$ or $(A - A_0)/A_0$) for all sensing channels were measured within the range of -1 to 1.5, with pH 7.4 in PBS solution as reference. Linear discriminant analysis (LDA) was used to generate a fingerprint pattern for the pH sensing of the array (**Fig. 4.24b**). The first two principal components (83.2% and 15.3%) were sufficient to easily differentiate the pH values, as better highlighted in the 3D fingerprint pattern (**Fig. 4.24c**).

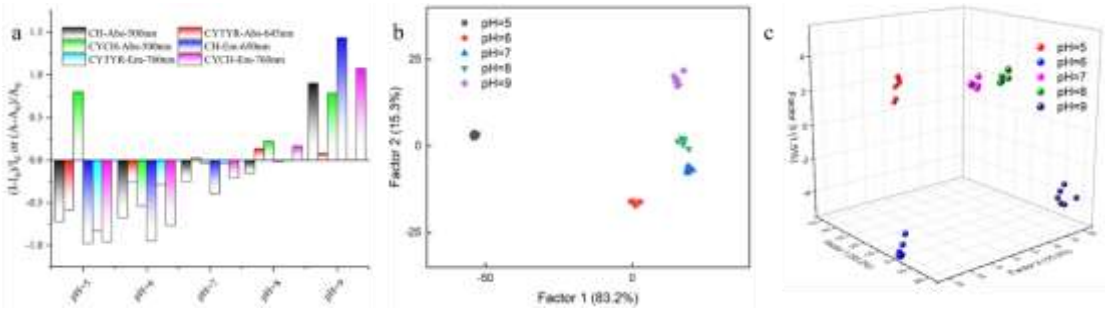

Fig. 4.24. a) Quenching ratios of pC at different pH values. b) Two-factor linear discriminant analysis fingerprint plot of pC for pH sensing. c) Three-factor linear discriminant analysis spatial fingerprint plot of pC for pH sensing.

Then, we applied the pC array to test a series of eight popular anti-aging worldwide produced face creams available in the market. High-quality products often use natural ingredients to protect the skin, while counterfeit products may add chemicals to achieve a deceptive appearance, leading to irreversible damage with long-term use. For example, polyphenols can act as antioxidants in skin care products.

However, polyphenolic compounds, flavonoids in particular, can interact with proteins both through nonspecific forces (*e.g.*, hydrogen bonding and hydrophobic effects) and by covalent

bond formation, forming complexes that impact protein function, solubility, stability.[220] Some unscrupulous businessmen will get this effect by adding phenol, but excessive phenol can cause skin discomfort. Excess phenol can affect the pH of skin care products, and we can use pC to identify it. The declared pH values of the anti-aging face creams ranged between 5.4 and 8.1 (Table 4.2).

Table S2 Anti-aging face cream product information of 8 brands from 8 countries

	Brand	Product	Region	pH
1	Herborist	Herborist Rejuvenating Cream	China	5.4
2	La Mer	La Mer Cream	U.S.	6.3
3	Lancôme	Lancôme Absolue Premium Bx Cream	France	7.7
4	La Prairie	La Prairie Cellular Cream Platinum Rare	Switzerland	6.8
5	Dr. Hauschka	Dr. Hauschka Regenerating Day Cream	Germany	7.4
6	Shiseido	Shiseido Future Solution LX	Japan	8.1
7	Acqua di Parma	Acqua di Parma Barbiere Revitalizing Face Cream	Italy	6.9
8	Sulwhasoo	Sulwhasoo Concentrated Ginseng Renewing Cream	South Korea	8.0

Solution of face cream at a concentration of 10 mg/mL was mixed with the pC array, resulting in a final dye concentration of 20 μM, and absorbance and emission were measured in the six channels (**Fig. 4.25**). A different quenching ratio was measured for each channel for the different creams, with face creams 1 and 2 that exhibited a more significant quenching, and creams 5 and 6 that showed a similar quenching pattern. The 2D fingerprint pattern successfully separated six of the face creams, but it was unable to differentiate face creams 4 and 7 as well as 6 and 8, which showed some overlapping (**Fig. 4.25b**). By incorporating a third factor in the LDA analysis (Factor 1: 74.2%, Factor 2: 23.7%, Factor 3: 1.7%), and analyzing the 3D spatial fingerprint pattern, all the creams were well differentiated (**Fig. 4.25c**).

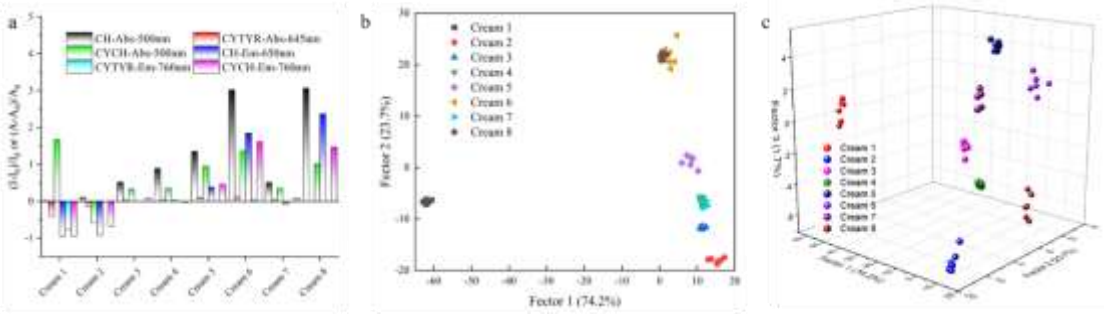

Fig. 4.25. a) Quenching ratios of pC at different creams. b) 2D analytical fingerprints of pC with eight face creams. c) Three-factor linear discriminant analysis spatial fingerprint plot of pC for creams sensing.

We further challenged the pC array with a solution of two randomized cream mixtures at a concentration of 10 mg/mL. The results indicated that pC performed well in the test. The two-dimensional fingerprint pattern successfully separated multiple blends of creams, with only individual overlaps when Cream 1 and Cream 3 were mixed with the other creams (**Fig. 4.26**).

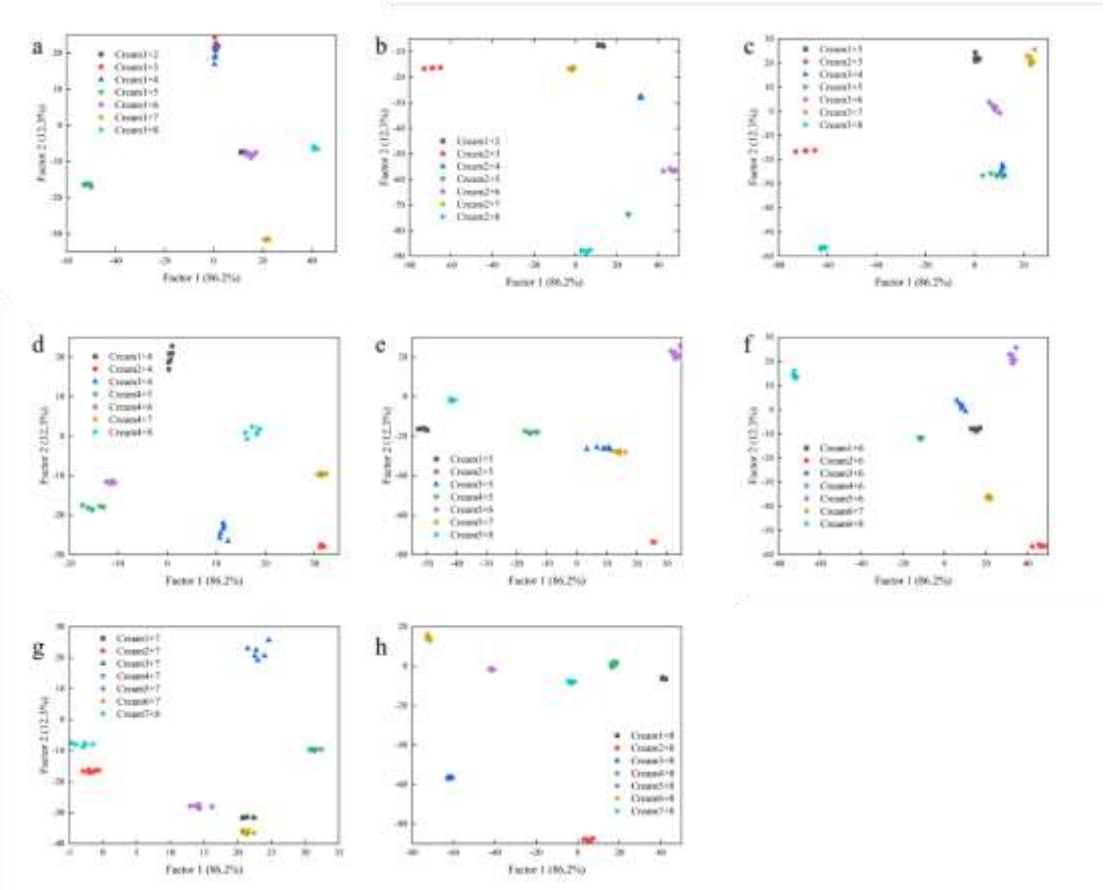

Fig. 4.26. 2D analytical fingerprints of pC with eight mix face creams

However, by adding a third factor, the three-dimensional spatial fingerprint pattern successfully analyzed all mixture solutions, with each mixture of creams having its own unique fingerprint pattern, suggesting that pC array has also a great potential for mixture identification (**Fig. 4.27**).

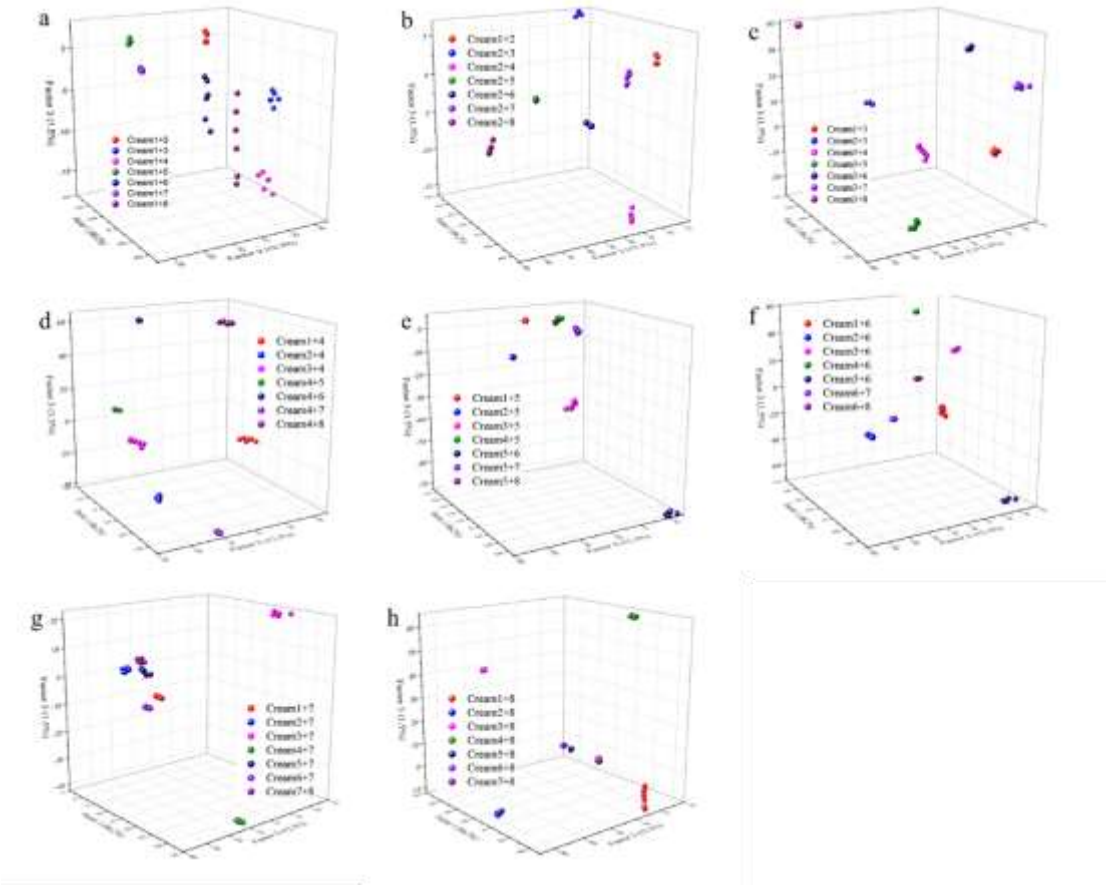

Fig. 4.28. 3D analytical fingerprints of pC with eight mix face creams

To further validate the accuracy of the pC array, we randomly selected a supplementary package of one face cream as an unknown sample for testing, and the results showed that the method successfully identified Cream X as the supplementary package of Cream 7 (**Fig. 4.29a**). In the ongoing exploration of the discriminative performance of pC array against counterfeit creams, we intentionally introduced various substances (formaldehyde, phenol, mercury ions, hydrogen peroxide, and acetone) into the selected eight creams. These substances represent common industrial compounds extensively utilized in the production of fraudulent cosmetics. The 3D fingerprint of cream 1 added with the “counterfeiting” substances revealed a distinct

identification of the modified cream (**Fig. 4.29b**), likely attributable to pH alterations and/or changes in the physico-chemical properties of the dyes induced by the added substances. Encouragingly, analogous positive outcomes were achieved for the remaining creams as well (**Fig. 4.30**). Notably, the entire identification process for each set of samples was completed within 15 minutes, demonstrating the rapid, accurate, and convenient characteristics of the test.

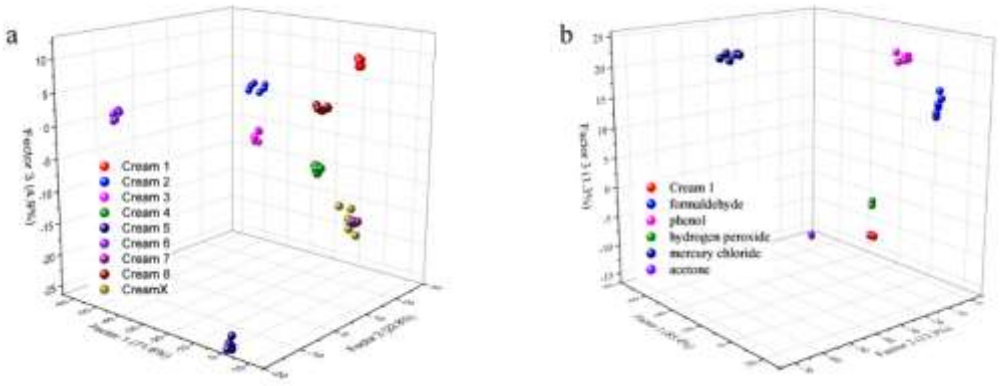

Fig. 4.29. a) 3D fingerprinting of unknown cream X identified by pC. b) 3D fingerprinting of cream 1 with pC identification of added and unadded industrial compounds

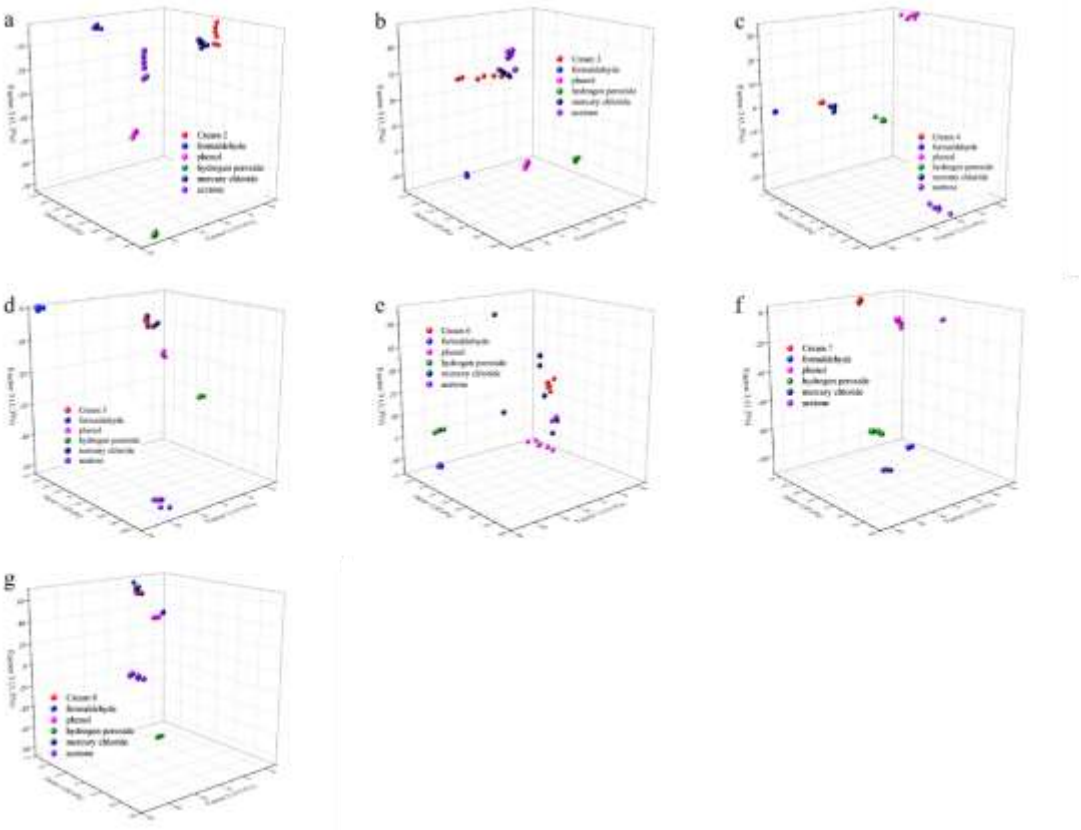

Fig. 4.30. 3D fingerprinting of creams 2-8 with and without added industrial compounds identified by pC.

4.4 Conclusion

In summary, this work reports the synthesis and characterization of two novel dyes, CH and CYTYR, with peculiar pH responsiveness properties. CH exhibits aggregation-induced emission (AIE) effect in water and undergoes a red shifted fluorescence emission under alkaline conditions that matches the absorption of CYTYR, thus allowing an efficient FRET effect. The dyes were combined with a phospholipid to form nanoaggregates, whose spectral patterns were utilized to design a six-channel pH sensing array with a pH detection interval between 4.7 and 9.25. The performance of this array was tested to evaluate the quality of eight commercially available anti-aging face creams. Linear discriminant analysis of the 3D fingerprint patterns demonstrated the ability of the array to effectively distinguish the different brands of the anti-aging products. Moreover, the array was challenged to analyze artificially sophisticated creams, further confirming the great potential to assess the quality of the products and identify possible frauds. The characterization of the products was completed within 15 minutes, showcasing the potential of the method in quality control tests in cosmetics industry.

Chapter 5 A nanoliposome with FRET properties for ratiometric detection of hypochlorous acid

Abstract

Two probes, Se-TPA and CYLYS, have been synthesized, characterized, and formulated in liposomes (CST-lipo) to promote a FRET effect for the detection of hypochlorous acid. Under 460 nm excitation, the ratio of the emission intensity of CST was proportional to the concentration of hypochlorous acid at 610 nm and 760 nm, with up to a 20-fold change in the ratio in the presence of the analyte. The detection range was 0-30 μM and the detection limit was as low as 17.5 nM. DFT calculations and mass spectral characterization confirmed the response mechanism. In addition, we tested the selectivity and stability of Se-TPA, CYLYS and CST-lipo and obtained promising results that suggest that CST has great potential for hypochlorite detection and rheumatoid arthritis imaging.

Key words: FRET; AIE; ratiometric detection; hypochlorous acid

5.1 Introduction

Hypochlorous acid (HClO)is a powerful oxidant and a key component of the immune response for neutrophils and macrophages.[221-224] When the body is attacked by bacteria, viruses, or other pathogens, the immune system releases hypochlorous acid to fight off the infection. In addition, hypochlorous acid can regulate immune responses and help the body fight inflammation and infection.[225-228] Hypochlorous acid is one of the most important reactive oxygen species (ROS), which is produced by the reaction of hydrogen peroxide and chloride ions in living systems catalyzed by myeloperoxidase (MPO).[8, 229-233] Excessive production of HClO is related to a variety of diseases, including cancer, atherosclerosis, neurodegenerative diseases and chronic inflammation. Rheumatoid arthritis (RA) is a chronic autoimmune inflammatory disease. It is understood that it is related to early The overproduction of HClO in RA is closely related, although the cause has not been fully elucidated. There are many methods to detect and imaging HClO, such as X-ray, MRI, and ultrasound imaging, but these methods

often have certain limitations in use, [224, 234-240] therefore there is still a need to develop new fluorescent probes to selectively and sensitively detect HOCl. Near-infrared (NIR) fluorescent probes are more conducive to in vivo imaging due to their deep tissue penetration, less light damage, non-invasiveness, and high sensitivity and selectivity. [221-223, 241-251] Here, two near-infrared emitting probes, Se-TPA and CYLYS, have been designed and developed. Se-TPA can produce AIE effects in water, whereas CYLYS was designed based on the cyanine dye IR783. This series of derivatives has strong penetration depth and good water solubility, making it very suitable for *in vivo* imaging. By embedding a mixture of the two probes in a liposome (CST-lipo), a FRET system was obtained for a highly selective and sensitive detection of HClO. CST-lipo has good stability and high selectivity and it can detect trace amounts of hypochlorous acid.

5.2 Experiment

5.2.1 Materials and methods

Unless otherwise noted, materials were obtained from commercial supplier's Sigma and used without further purification. DSPE-PEG2000-NH2 was purchased from Sigma as a 25 mg/mL chloroform solution. Nitric oxide was provided by sodium nitroprusside and $ONOO^-$ was prepared according to the literature method.[252] Deionized water was obtained by Milli-Q water purification system (Millipore) with electrical conductivity of 18.2 s/m. Using tetramethylsilane (TMS) as the internal standard, ^1H and ^{13}C NMR spectra were recorded on Bruker Avance III spectrometer at 600 MHz frequency. The mass spectrometry was recorded on the Brook Electron spray Ionization Mass Spectrometer (ESI-MS). The UV-Vis absorption spectrum was collected by CARY50 biological spectrophotometer (Varian Inc., CA., USA). The fluorescence spectrum was measured on Fluoromax-4 fluorescence spectrophotometer (HoribaJobinYvon Inc., USA). The spectrum was recorded at 25 °C, and the excitation and emission slits are 3nm. The 8 anti-aging creams used in this study were unopened samples provided by the manufacturers at the time of purchase. All samples were within their expiration dates, ensuring their freshness and effectiveness.

5.2.2 Synthesis of Se-TPA

Se-TPA was synthesized according to published literature methods. [253]

5.2.3 Synthesis of CYLYS

CYLYS can be synthesized in a one-step reaction from IR783. IR783 and 5 were dissolved in 1 mL of DMF and reacted at 85°C for 3 hours. The solvent was then removed by vacuum distillation. Column chromatography separation (dichloromethane: methanol = 3:1) resulted in 38 mg blue solid with a yield of 62%. MS (ESI): calculated for $C_{46}H_{56}N_3O_7S_2^-$ $[M+H]^+$: 819.34, found 819.34

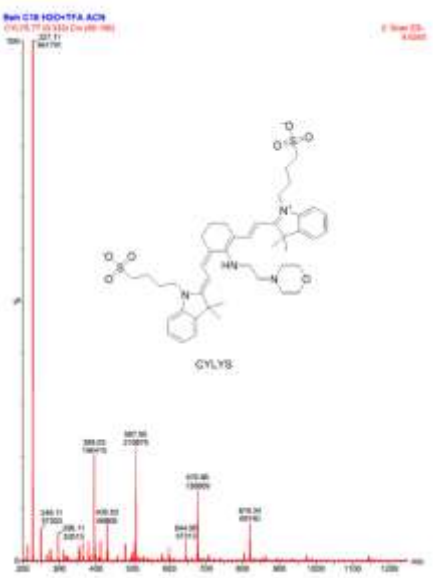

Fig. 5.1 Mass spectrum of CYLYS

5.2.4 Synthesis of CST

For the CST-lipo sensor, the following general methods were employed. The Se-TPA and CYLYS were mixed at a molar ratio of 1:4. A Se-TPA stock solution (10 μL, 1 mM in THF) and a CYLYS stock solution (40 μL, 1 mM in MeOH) were combined with 5%DSPE-PEG2000-NH2 (25 mg/mL in $CHCl_3$) and 2% 1-hexadecanoyl-2--(9Z-octadecenoyl)-sn-glycero-3-phosphocholine; POPC; . The organic solvent was then removed by vacuum rotary evaporation, resulting in a dry lipid film containing the dyes. The dried film was hydrated with 1 mL of deionized water and subjected to sonication for 1 minute to obtain a clear stock solution

of sensors with a dye concentration of 10 μM /40 μM. To prepare the test sensors solution, 0.2 mL of the stock sensors solution was mixed with different pH buffers (0.8 mL), resulting in a test sensors solution with a CST-lipo dye concentration of 2 μM / 20 μM for absorbance and emission measurements. CST-lipo samples with different Se-TPA/CYLYS ratio (1:1, 1:2, 1:3) were also prepared.

5.2.5 Selectivity study

Using Se-TPA as a typical example, the probe was incubated with various 10mM ionic. The fluorescence spectra were measured to evaluate the response reliability.

5.2.6 The sensor of CST to pH

A buffer solution (10 mM) was prepared by dissolving citric acid and sodium citrate in water to achieve the desired pH range from 2.0 to 11.0. Se-TPA, CYLYS, and CST-lipo were added to the appropriate pH buffer solutions to obtain fluorescence buffer solutions at a concentration of 20 μM. The data for their respective response wavelengths were recorded using Microplate reader. The excitation and emission wavelengths used were as follows:

Se-TPA: Excitation at 475 nm, Emission at 645 nm.

CYLYS: Excitation at 645 nm, Emission at 760 nm.

CST-lipo: Excitation at 475 nm, Emission at 760 nm.

5.2.7 Density Functional Theory (DFT) Calculations.

To understand the difference in spectral and chemical properties between the new functionalized compound Se-TPA and CYLYS, the calculations have been performed on them using the Gaussian 09 program package. The ground state geometries were optimized with B3LYP/6-31G (d). The HOMO (highest occupied molecular orbital) and LUMO (lowest unoccupied molecular orbital) of the molecules were visualized with Gauss View 05.

5.3 Result and discuss

In order to develop hypochlorous acid probes with high sensitivity and selectivity, we introduced a fluorescent sensor named CST-lipo, which offered rapid, sensitive, and highly selective detection of hypochlorous acid. CST-lipo was composed of four key components: Se-TPA and CYLYS dyes, 2%POPC, and 5%DSPE-PEG2000-NH_2. It is worth noting that Se-TPA

and CYLYS were easily synthesized with high yields, as detailed in **Scheme 5.1**.

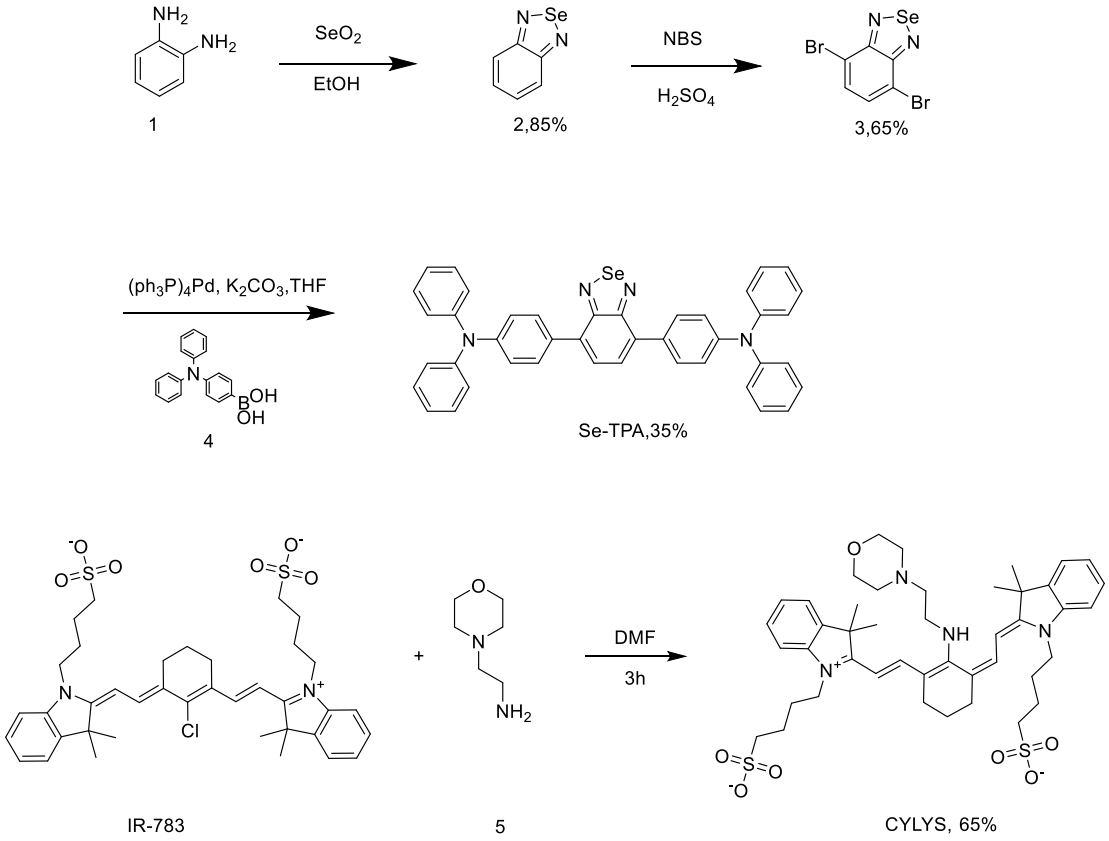

Scheme 5.1 Synthetic routes of Se-TPA and CYLYS

Se-TPA had been synthesized following a well-established procedure documented in the literature. The boronic acid derivatives of triphenylamine and dibrominated benzoselenothiazoles had been readily coupled through the Suzuki reaction to yield Se-TPA under mild reaction conditions. CYLYS was prepared via the reaction of IR783 with the corresponding amine in DMF. When commercially available DSPE-PEG2000-NH2 and POPC are combined with a mixture of Se-TPA and CYLYS, it was self-assembled into nanoliposome in an aqueous milieu, enabling Förster resonance energy transfer (FRET).

The benzoselenothiazole derivatives in Se-TPA possessed a formidable electron-withdrawing ability. By linking benzoselenethiazole and triphenylamine through a Suzuki reaction, a large donor-acceptor-donor (D-A-D) conjugated structure was crafted. This structure exhibited excellent aggregation-induced emission (AIE) properties, with aggregates in an aqueous

medium emitting vibrant fluorescence. Consequently, Se-TPA was employed as the FRET energy donor, while the diethylaminomorpholine-modified anthocyanine dye, CYLYS, was introduced as the energy acceptor.

In the presence of hypochlorous acid, CYLYS underwent oxidation, inducing a transformation in its molecular structure. The originally conjugated double bond was oxidized to form ethylene oxide, resulting in quenching the CYLYS emission, preventing FRET effect, and recovering Se-TPA fluorescence. (**Scheme 5.2**)

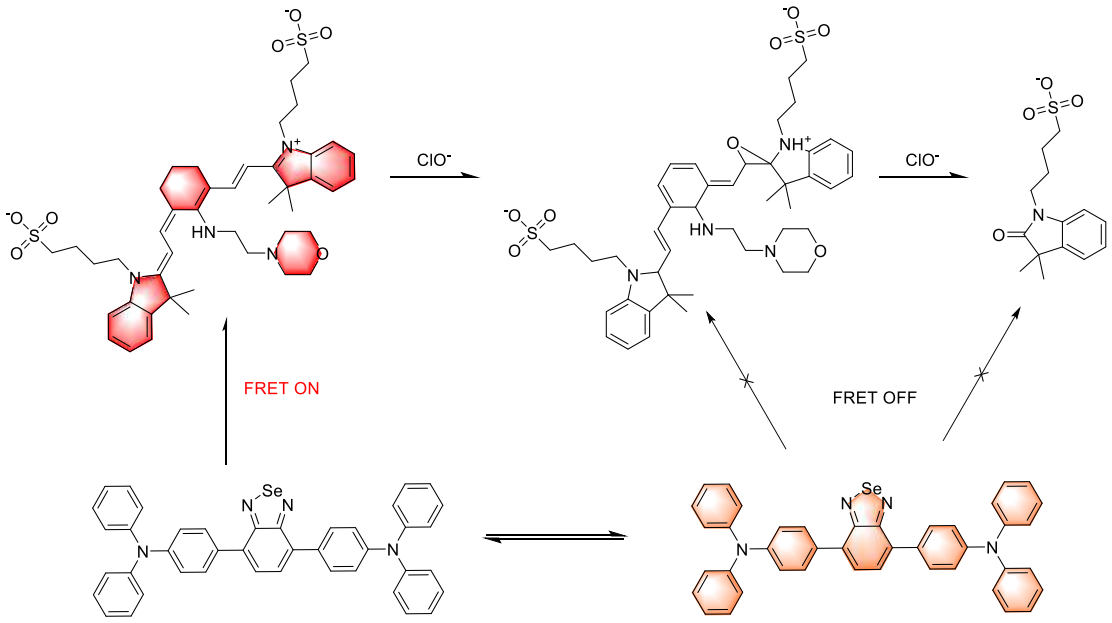

Scheme. 5.2 The mechanism of CST detection of hypochlorous acid.

Fig. 5.2 shows the spectral characteristics of Se-TPA and CYLYS. The maximum absorption and emission wavelengths for Se-TPA was 475 nm and 650nm, respectively, whereas the same absorption/emission pair for CYLYS are 645 nm and 760 nm. The excellent overlapping between the emission of Se-TPA and the absorption of CYLYS makes these dyes perfect candidates for promoting an efficient FRET effect. It is worth noting that these spectra were acquired in water. Although Se-TPA is insoluble in water, its unique AIE properties make its fluorescence emission in water still strong, while CYLYS showed a much better water solubility primarily caused by the presence of the two sulfonic moieties.

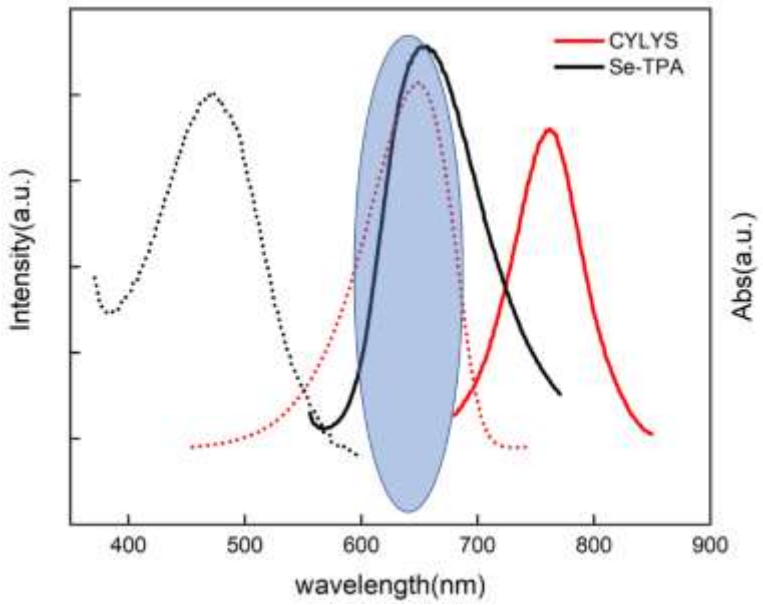

Fig. 5.2, Normalized spectra of Se-TPA and CYLYS, where the solid line is the emission spectrum and the dashed line is the absorption spectrum.

To investigate potential disparities in the optical properties of Se-TPA and CYLYS across different solvent environments, a series of dissolution effect experiments were conducted. Remarkably, substantial disparities in the emission intensity were observed for Se-TPA upon changing the solvent polarity. In fact, As the solvent polarity increased, the maximum emission wavelength of Se-TPA exhibited a pronounced redshift, albeit accompanied by a concomitant decline in emission intensity (**Fig. 5.3A**). Particularly noteworthy was the nearly negligible fluorescence emission intensity observed in ethanol, the most polar solvent, when compared to hexane. **Fig. 5.3B** portrays the emission spectra of CYLYS in several solvent systems. The emission spectra displayed a slight redshift concomitant with increasing solvent polarity. It is worth noting that the most prominent redshift for CYLYS was observed in a PBS solution, while concurrently exhibiting the lowest emission intensity at the same concentration.

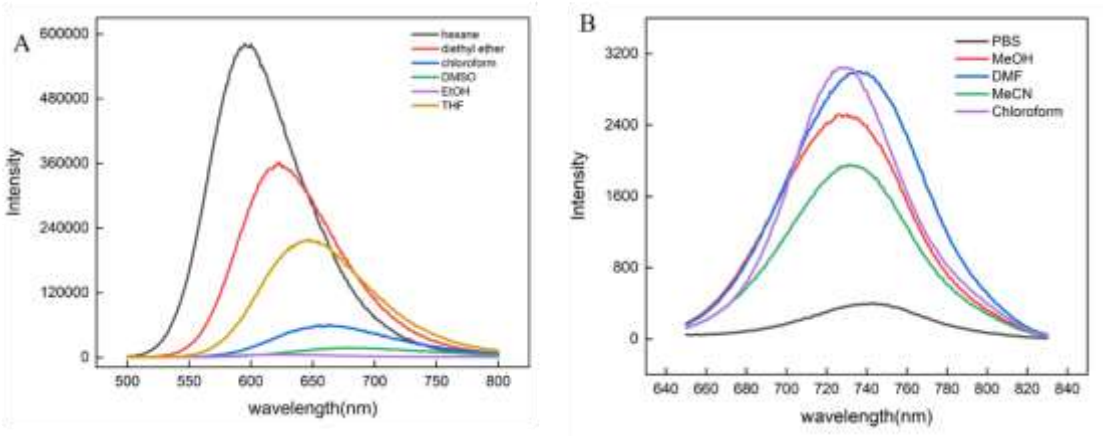

Fig. 5.3 A) Emission spectrum curves of Se-TPA in different solvents. B) Emission spectrum curves of CYLYS in different solvents.

In **Fig. 5.4A**, the emission of Se-TPA in a THF solution at 645 nm was scrutinized as a function of the dye concentration. The fluorescence intensity was linearly correlated to the concentration up to 50 mM. Beyond this concentration, the emission intensity started quenching and approached a plateau at the highest concentration investigated (500 μM). The inset graph illustrates the linear correlation between concentration and emission intensity, substantiating our choice of 10 μM as the optimal test concentration.

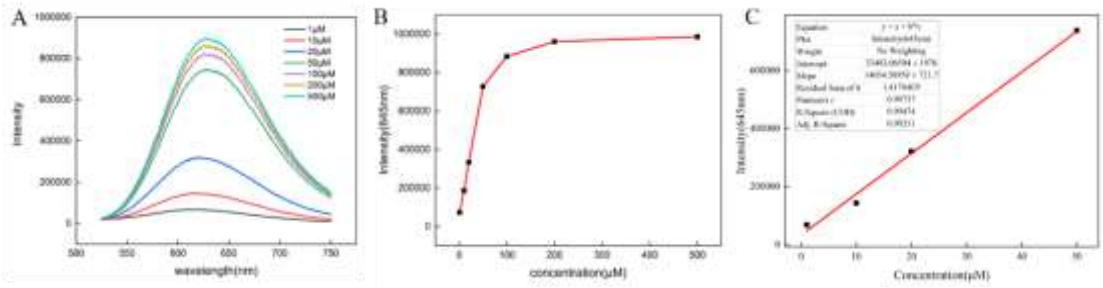

Fig. 5.4 A)Fluorescence emission curves of Se-TPA in THF as a function of concentration. B) Trend of fluorescence intensity of Se-TPA at 645 nm. C) The linear relationship of fluorescence intensity at 645 nm as a function of concentration 0-50 μM

Fig. 5.5A portrays the emission profile of different concentrations of CYLYS (peak at 760 nm) in PBS buffer. **Fig. 5.5B** shows that the fluorescence is linearly correlated with the concentration up to 20 mM. A further increase in concentration led to a fluorescence quenching,

a phenomenon attributable to a π-π stacking of the CYLYS molecules. The diminished fluorescence due to high concentration is analogous to π-π stacking of planar macromolecules. Such stacking is common in planar molecules such as pyrene and perylene. [6] The production of massive stacking leads to mutual depletion of intermolecular energy and fluorescence quenching.

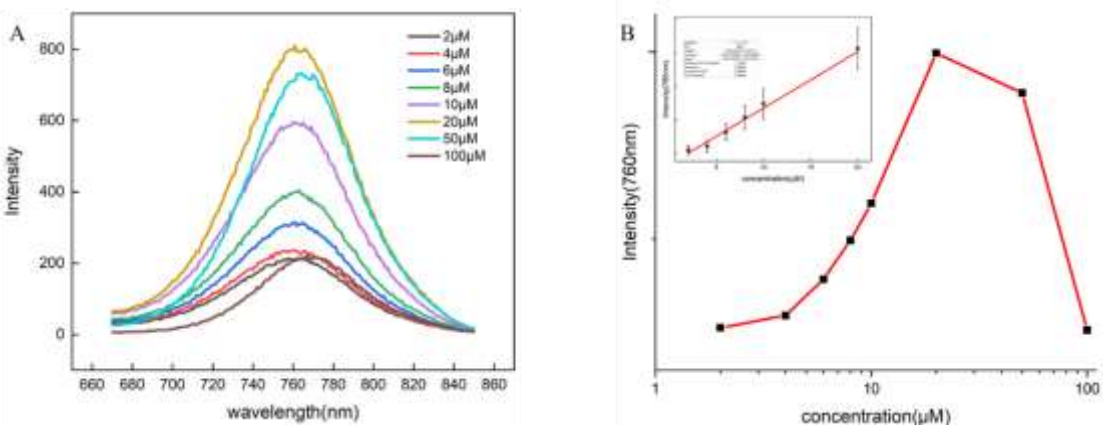

Fig. 5.5A) Fluorescence curves of CYLYS as a function of concentration in PBS. B) Emission intensity change at 760nm, inset is the linear relationship between concentration and emission intensity.

We also investigated the AIE properties of Se-TPA dyes by varying the water content in the mixture of water-soluble organic solvent (THF) and water. **Fig. 5.6B** shows that the emission intensity of Se-TPA in THF/H_2O mixtures with water contents ranging from 0 to 80 vol% decreased with increasing the water content. When the water content was further increased to 50%, an intense emission peak was observed at 610 nm, and this new emission peak continued to enhance with increasing water content.

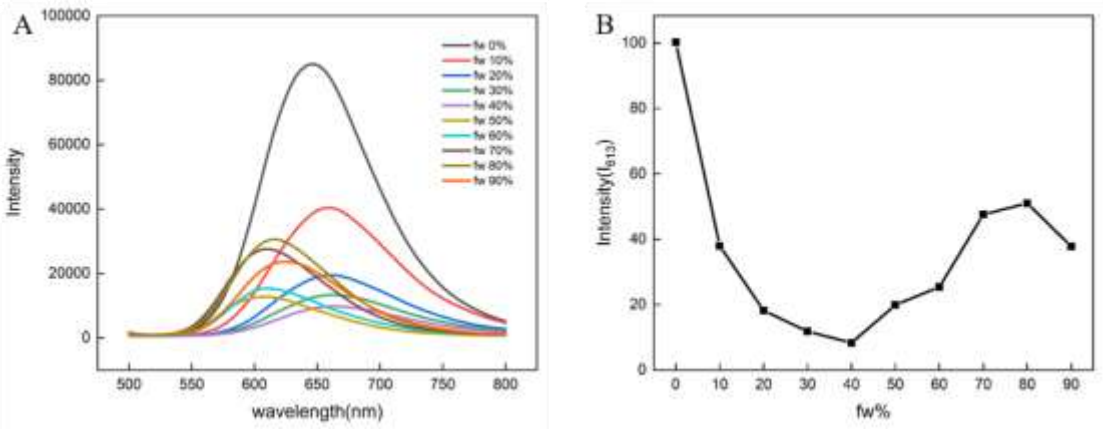

Fig. 5.6A) Fluorescence emission curves of Se-TPA in different ratios of THF/water mixed solutions. B) Trend of fluorescence intensity of Se-TPA at 645 nm.

The behavior observed for Se-TPA in 90% water well agrees with the expected pattern of the AIE phenomenon due to the formation of dye aggregates, which was also confirmed by the dynamic light scattering (DLS) results **(Fig. 5.7)**. The weaker emission of Se-TPA in the THF/water mixtures with f_w of 90% compared to that with f_w of 80% is probably due to the difference in aggregate morphology.[253]

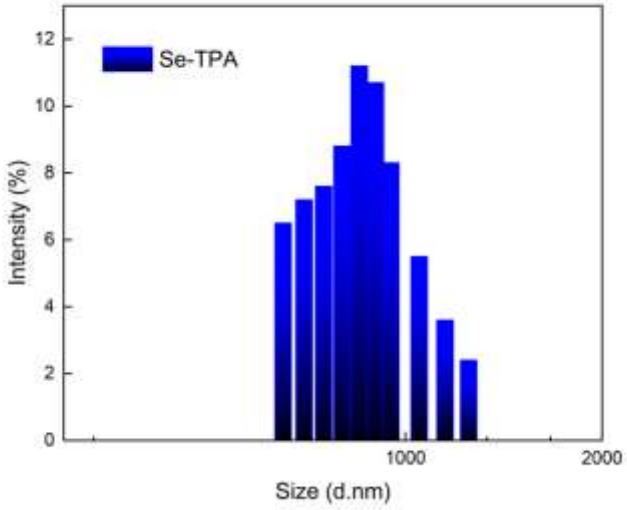

Fig. 5.7 Particle size distribution of Se-TPA aggregates in 90% water.

After understanding the basic characteristics of CYLYS and Se-TPA, we started to try to establish their FRET relationship. To enable FRET, the dyes were incorporated in pegylated

liposomes. Liposome formulations with different molar ratio between the two dyes were prepared and compared with liposomes incorporating the individual dyes.

Fig. 5.8A shows the emission spectra of the different liposomes investigated. When the excitation was placed at 460 nm, only the liposome loaded with Se-TPA showed a maximum emission at 610 nm and almost no emission at 760 nm. Similarly, liposomes incorporating only CYLYS exhibited a maximum emission at 760 nm under 650 nm excitation. For the mixed liposomes, as the Se-TPA content increased, the 460 nm excitation was used, and the emission intensity at 760 nm was greatly enhanced, suggesting the occurrence of the FRET effect. The liposomes with a Se-TPA/CYLYS molar ratio 4:1 did not form due to the presence of a Se-TPA precipitate. On the contrary, increasing the amount of CYLYS revealed that the fluorescence emission intensity at 760 nm also increased, partly due to the fluorescence enhancement induced by FRET and partly due to the fluorescence enhancement induced by increasing concentration of CYLYS itself. At the same time, the fluorescence emission intensity at 610 nm keeps decreasing as the content of CYLYS increases. At the Se-TPA/CYLYS ratio 1:4, the emission intensity at 610 nm is basically close to 1:3, which indicates that the liposome has reached the optimum. The emission intensity ratio between 760 nm and 610 nm of the liposomes examined, and reported in **Fig. 5.8B**, reached a maximum value at the ratio 1:4, which was selected for the next experiments and named CST-lipo. After this we made "clinical" liposomes, we opted to use 2% POPC and 5% DSPE-PEG2000-NH2 As the synthetic material of liposome, CYLYS is 4eq of Se-TPA. Obtained the liposome CST.

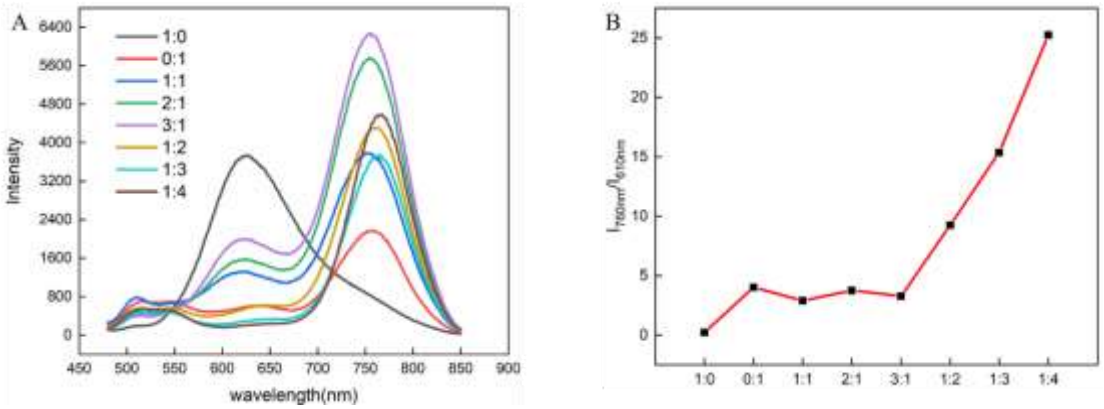

Fig. 5.8 A) Fluorescence emission curves of liposomes formed with different ratios of Se-

TPA/CYLYS. B) The relationship between the intensity ratio and ratio of 760nm and 610nm.

To further confirm that FRET is produced by the two dyes in liposomes, we performed liposome stability experiments and the results proved that the fluorescence of FRET is heavily dependent on the stability of liposomes. **Fig. 5.9** demonstrated that adding Triton-X100 to the CST-lipo sample, the emission spectrum significantly changed, with the recovery of the emission from Se-TPA and the decrease of the emission of CYLYS, observations consistent with the reduction of the FRET coupling. We were computed the spectral overlap integral and determine that the distance between the two molecules is R_0=5.06nm, meeting the necessary conditions for FRET to take place[10]. The resulting FRET efficiency was found to be 81%.

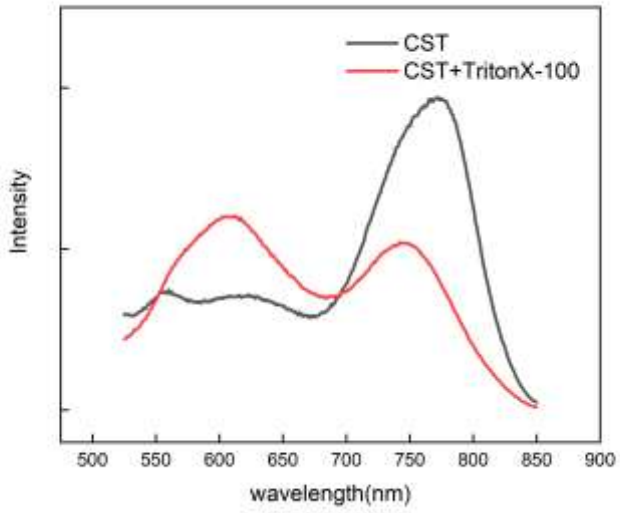

Fig. 5.9 Fluorescence emission curves of CST in PBS buffer (black) and in PBS buffer (red) with TritonX-100

The pH dependence of the emission was tested on the two dyes and CST-lipo. The fluorescence of Se-TPA was unaffected by pH (**Fig. 5.10A**), while the samples containing CYLYS were characterized, upon decreasing pH values, by a reduction in the intensity of the emission peak at 760 nm and the appearance of a new emission peak at 680 nm. We believe that this is an alteration of the emission due to the the protonation of the secondary amine in CYLYS. (**Fig.**

5.10B). **Fig. 5.10C** reports the pH dependence of the emission intensity ratio between 760 nm and 660 nm, which exhibited a linear dependence in the 3.5-5.5 pH range (see inset).

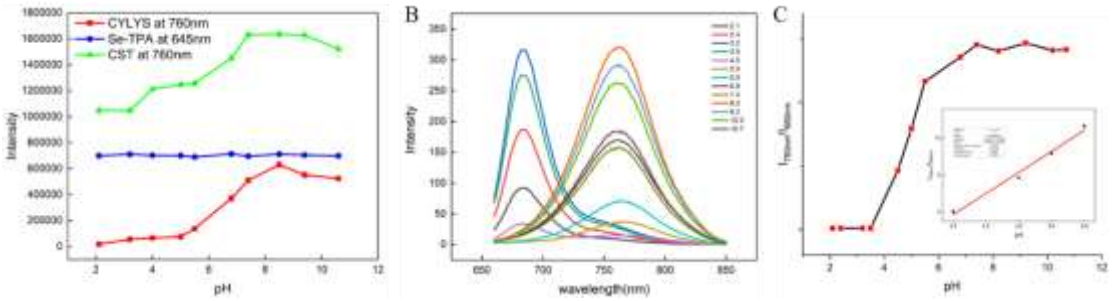

Fig. 5.10 A) Changes in fluorescence emission intensity with pH in PBS for Se-TPA, CYLYS and CST B) Fluorescence emission curves of CYLYS at different pH. C) The relationship of I760/I680 with pH, the inset shows the linear relationship between the ratio and pH at pH3.5-5.5.

The pH dependence of the emission of CST-lipo sample is displayed in **Fig. 5.11A**. The incorporation of the dye in the liposomes attenuates the pH effect on CYLYS, and the emission at 760 nm is partly retained at acidic pH. On the other side, the emission peak at 610 nm is reduced. **Fig. 5.11B** shows that for this sample the pH dependence of the 760/610 ratio is not linear, but quadratic in the 2-1-6.8 pH range (see inset).

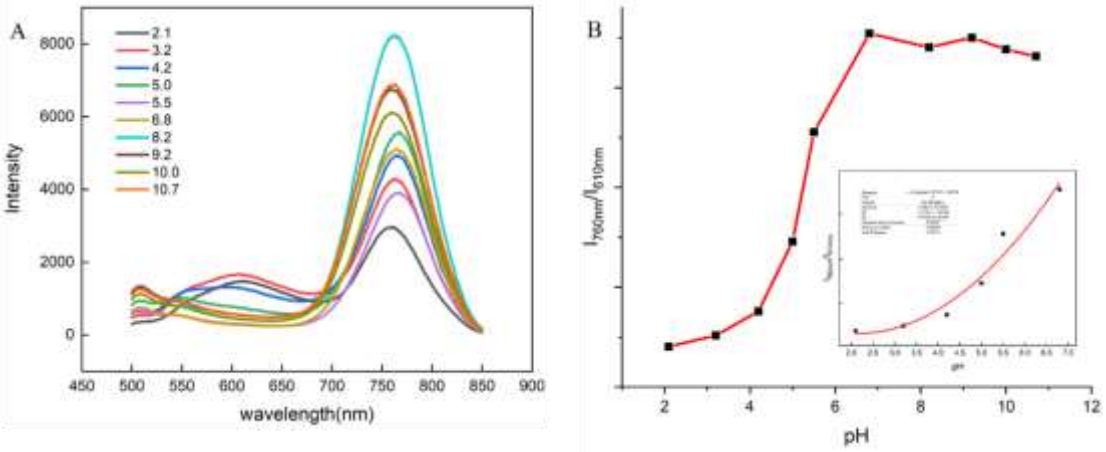

Fig. 5.11 A) Fluorescence curve of CST as a function of pH. B) the relationship between the ratio of 760nm and 610nm and pH. The illustration is the quadratic linearity of pH2.1-6.8

relation.

The photostability of the sample (**Fig. 5.12**), over one hour of illumination, was good, with only a slight decrease in the emission of CYLYS dye, when not incorporated in liposomes.

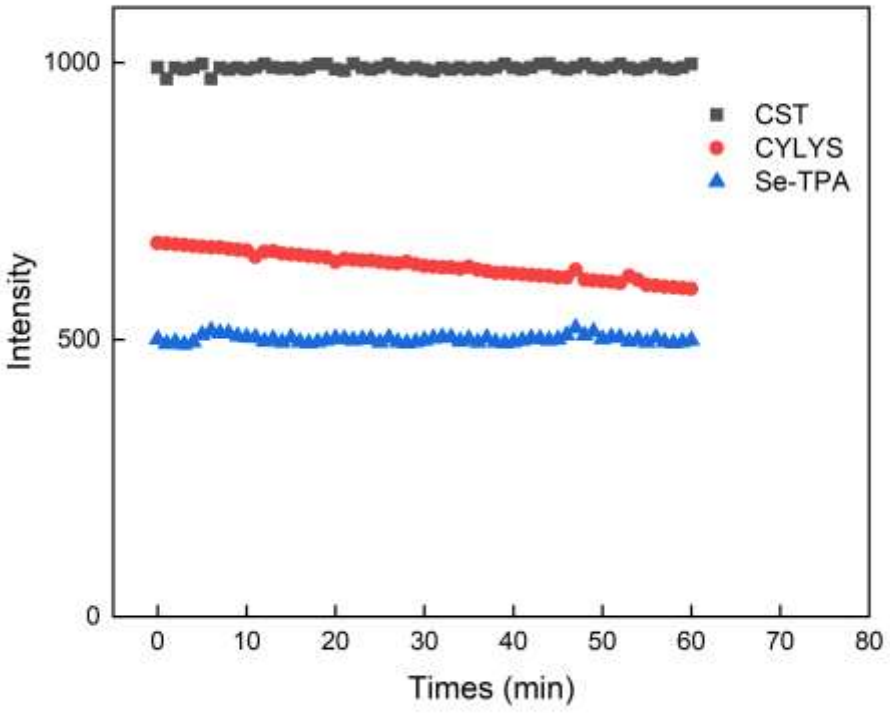

Fig. 5.12 Photostability of probes over 60 minutes

Next, the response of CST-lipo to sodium hypochlorite was tested in PBS at pH 7.4 (**Fig. 5.13A**). By increasing the amount of the analyte, the fluorescence intensity at 760 nm decreased progressively, while the emission intensity at 610 nm increased. The **Fig. 5.13B** reports a comparison between the photograph of the real samples before and after adding sodium hypochlorite solution.

The ratio fluorescence increases nearly 20 times before and after the response.

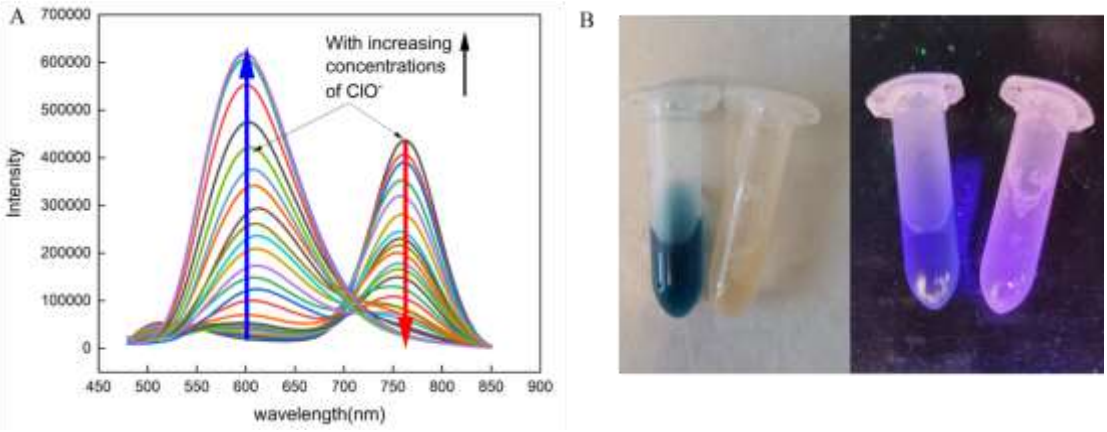

Fig. 5.13A) Ratio-response spectral curves of CST-lipo as function of 0-100 μM sodium hypochlorite. B) CST-lipo samples under bright (left photograph) or UV (right photograph) light. In each photograph, the left tube contained CST-lipo prior the addition of sodium hypochlorite.

By plotting the emission intensity ratio between 610 nm and 760 nm, an excellent linearity up to a 30 mM concentration of hypochlorite ion was obtained (**Fig. 5.14**). In these experimental conditions, a detection limit of 17.5 nM was determined for hypochlorous acid using CST-lipo sensor.

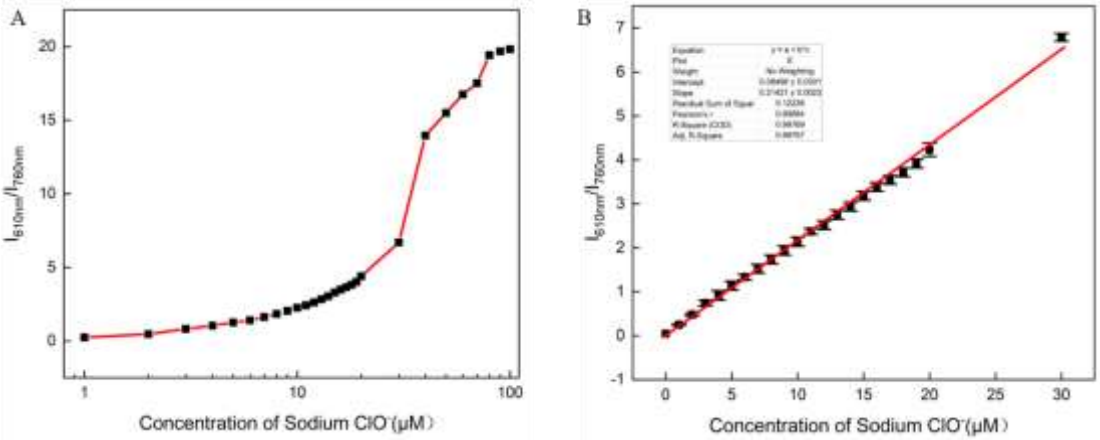

Fig. 5.14 A) The relationship between the emission intensity ratio of CST at 610nm and 760nm and the concentration of sodium hypochlorite solution. B) The linear relationship between sodium hypochlorite concentration and emission intensity ratio for 0–30 μM.

CYLYS exhibited remarkable sensitivity to hypochlorite and underwent rapid oxidation upon

exposure to hypochlorite, resulting in the quenching of near-infrared (NIR) fluorescence. **(Fig. 5.15A)** Conversely, Se-TPA displayed relative stability in the presence of hypochlorite, facilitating the realization of ratio-based hypochlorite detection. (**Fig. 5.15B**) As hypochlorite concentration varied, the fluorescence of CYLYS diminished, while that of Se-TPA was rekindled. According to the mechanism described in ref. 7, CYLYS and hypochlorous acid may form an oxirane derivative at the double bond, causing the fluorescence quenching at 760 nm, and the new substance formed has no absorption wavelength at 650 nm. FRET will end at this time, AIE fluorescence recovery of Se-TPA.

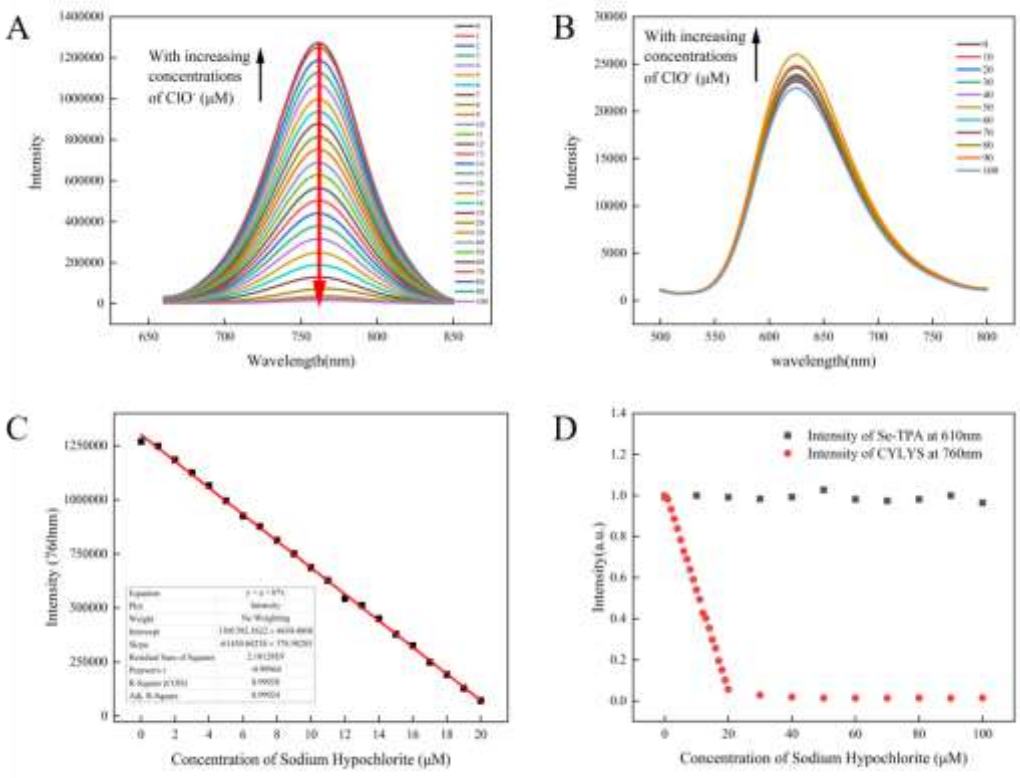

Fig. 5.15 A) Response spectral curves of CYLYS as function of 0-100 μM sodium hypochlorite. B) Response spectral curves of Se-TPA as function of 0-100 μM sodium hypochlorite. C) The linear relationship between sodium hypochlorite concentration and CYLYS emission intensity at 760nm for 0–20 μM. D) The relationship between the emission intensity of Se-TPA and CYLYS at 610nm and 760nm and the concentration of sodium hypochlorite.

The emission at 610 nm (excitation 460 nm) for Se-TPA, CYLYS and CST-lipo samples was

also measured dynamically in the presence of sodium hypochlorite 5 μM (**Fig. 5.16**). CYLYS dye did not emit, thus confirming that the emission detected in CST-lipo was due to Se-TPA dye after the inactivation of the FRET effect, thus showing that sodium hypochlorite can only simply quench the fluorescence of CYLYS, but cannot make it produce a new emission peak at 610nm. The fluorescence intensity of CST-lipo increased with time up to 1 h, while Se-TPA was stable in sodium hypochlorite. So the signal at 610nm is emitted by Se-TPA after FRET is destroyed.

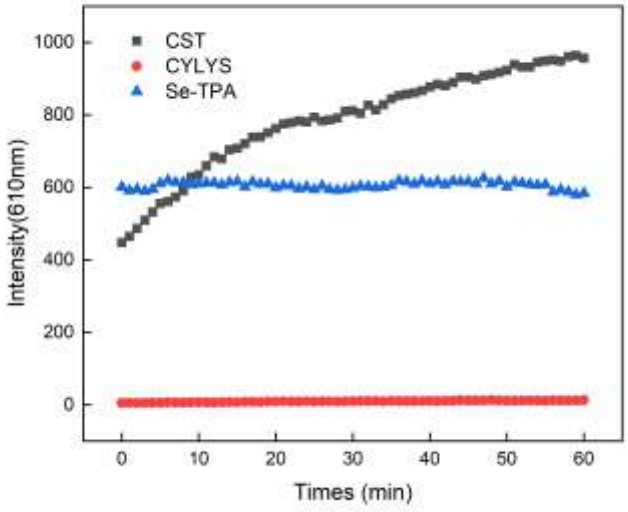

Fig. 5.16 5μM sodium hypochlorite solution, Se-TPA (blue), CYLYS (red) and CST-lipo (black) fluorescence intensity changes at 610nm.

The reaction with the analyte also caused a significant change in the size of CST-lipo sensor. DLS analysis (**Fig. 5.17**) showed that the hydrodynamic diameter of liposomes was around 230 nm (PDI 0.3) before the addition of sodium hypochlorite, and decreased to less than 100 nm (PDI 0.3) in the presence of the analyte.

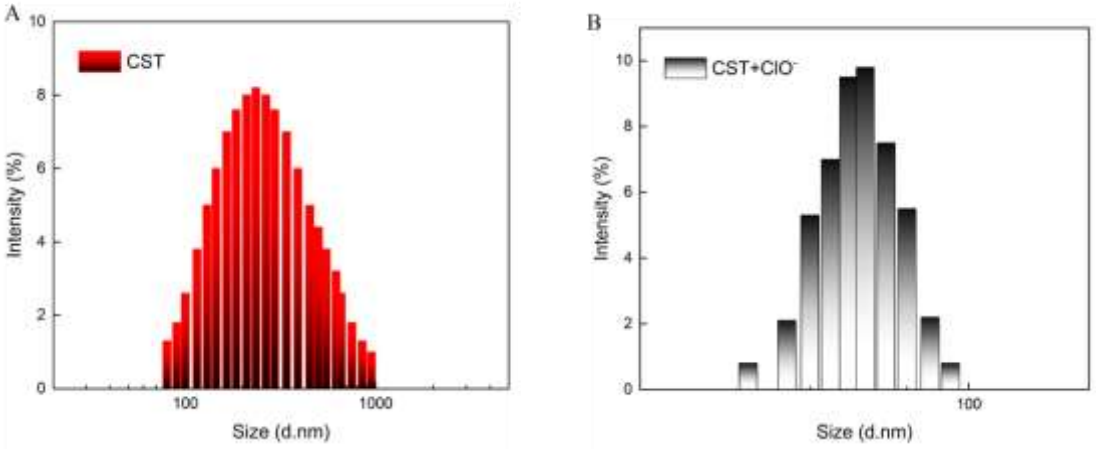

Fig. 5.17. A) Particle size distribution of CST. B) CST after response with ClO^-

To further confirm the mechanism of action of the sensor, an excess of hypochlorite was added to a solution of CYLYS and the system was analyzed by mass spectrometry. **Fig.5.18** showed that the double bond of CYLYS was oxidized first, and as the concentration of hypochlorite increased, the oxidized ethylene oxide began to follow the indole portion of the indole, and the amino with morpholine portion of the oxidized, and eventually formed aldehydes. The oxidation of the double bond resulted in the electron flow being impeded and the fluorescence of CYLYS disappeared. This result agrees with previous reports in the literature. [8]

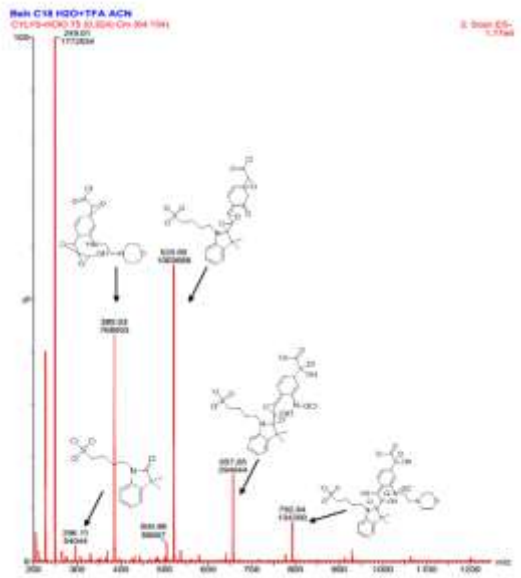

Fig. 5.18 Mass spectra of CYLYS after addition of an excess of sodium hypochlorite.

We also performed density-functional theory (DFT) calculations using Gaussian 09 B3LYP/6-31g(d) to further explain the reaction mechanism. (**Fig. 5.19**) The CYLYS molecule's main electrons are concentrated near the morpholine group, while its empty orbitals are distributed in the cyanine body. The energy difference between these two regions is only 0.6eV, which aligns with FRET production conditions since Se-TPA has an excitation energy of 2.41eV. However, after reacting CYLYS with hypochlorous acid, the reaction structure is destroyed and electrons shift towards ethylene oxide in the cyanine body. Energy is mainly provided by alpha orbital and there is a significant increase in energy difference although it does not exceed that of Se-TPA at 2.41eV. Unfortunately, this new product no longer absorbs light within a range of 600-650nm; Therefore, FRET cannot occur due to blocked absorption spectrum.

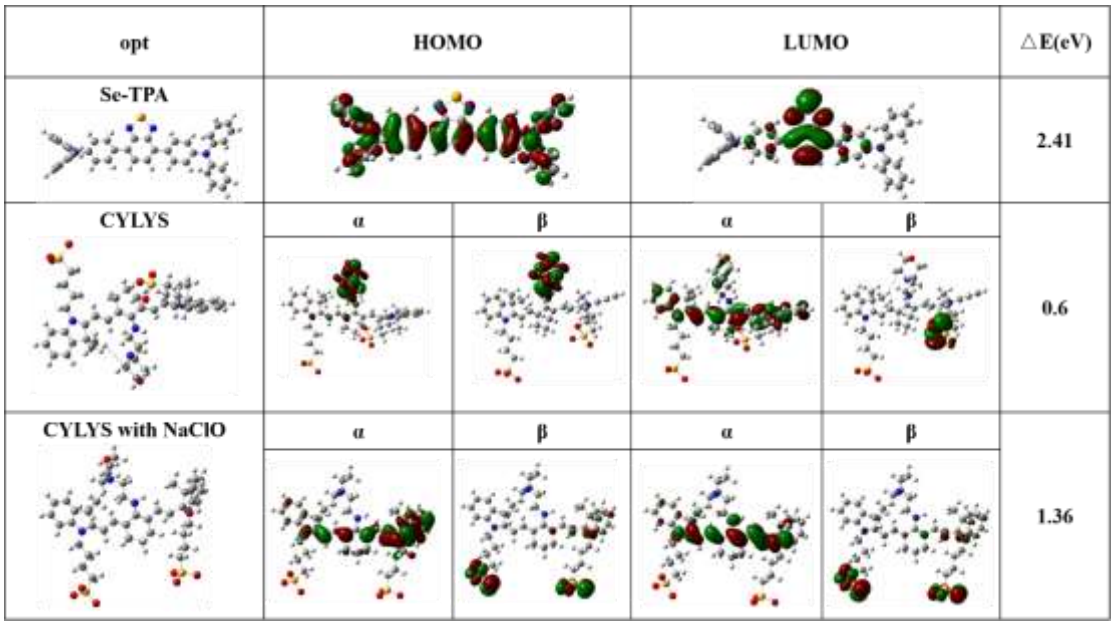

Fig. 5.19. Molecular model optimization and HOMO, LUMO orbital energy levels before and after the reaction of Se-TPA and CYLYS with hypochlorous acid

Finally, we performed a test to assess the selectivity of CST-lipo to detect the analyte (**Fig. 5.20**). Despite the presence of reactive oxygen and reactive nitrogen species, CST-lipo was able to show good stability, with significant selectivity only to sodium hypochlorite. The results obtained for CYLYS were very similar to those of CST-lipo, while Se-TPA was much more stable, showing little sensitivity to ions and reactive molecules.

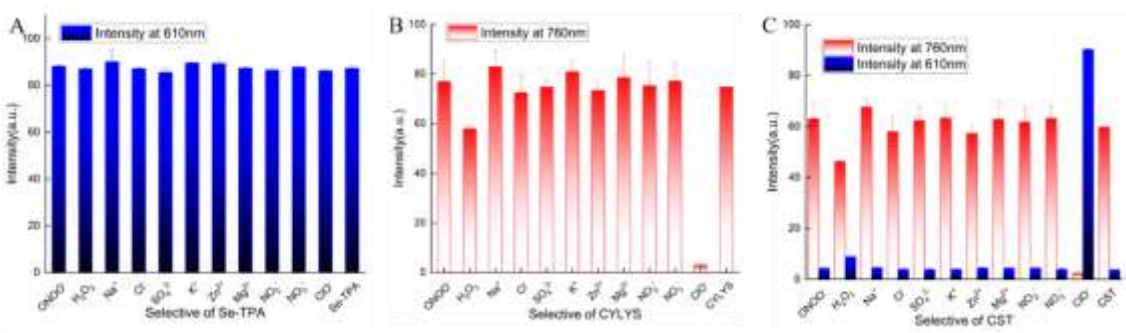

Fig. 5.20 The A) Se-TPA,B) CYLYS and C) CST-lipo of Selective histogram

5.4 Conclusion

In summary, we designed and synthesized two probes, Se-TPA and CYLYS, and characterized their properties. Se-TPA exhibited AIE properties in water, with an emission peak at 650 nm corresponding to the absorption peak of CYLYS. Both were used to fabricate a clinical liposome CST with FRET effect. Ratio metric detection of hypochlorous acid was achieved with CST under 460 nm excitation, and the emission intensity ratios of CST at 610 nm and 760 nm were proportional to the concentration of hypochlorous acid in the range of 0-30 μM, with a limit of detection as low as 17.5 nM. DFT calculations and mass spectrometry characterization confirmed the response mechanism. We also tested Se-TPA, CYLYS, and CST for selectivity and stability with excellent results. With the above characterization, we believe that CST has great potential for the detection of hypochlorite and rheumatoid arthritis imaging.

Chapter 6 Conclusion

In our research work, we focus on the development and application of various fluorescent probes for specific sensing purposes. These probes are tailored for specific analytical tasks, have unique properties, and show great potential in different applications.

1. Amino-Modified PDI Probe (N-PBI) for NO Sensing:

In our work, we designed and synthesized an amino-modified PDI probe (N-PBI) for selective sensing of nitric oxide (NO) in different environments (including cellular and atmospheric environments) for selective sensing of nitric oxide (NO).N-PBI has excellent nitric oxide selectivity, sensitivity, large Stokes shift, and near-infrared emission. In addition, we have achieved excellent detection sensitivity with a detection limit as low as 13 nM, which allows for the detection of NO in cells and air when used as a thin film. Together, these discoveries highlight N-PBI's superior ability to image NO, and hold great promise for the early detection of diseases associated with endogenous NO imbalance.

2. Fluorescent Probe (BNOH) for Picric Acid Detection:

In our study, we successfully designed and tested a fluorescent probe named BNOH, which contains a B-N bond and a hydroxyl group, and was mainly used for the sensitive detection of the explosive picric acid (PA).BNOH possesses an aggregation-induced emission (AIE) effect in aqueous environments, which shows a strong fluorescent signal.The interaction between BNOH and PA leads to a significant fluorescence quenching, which indicates high selectivity and sensitivity. This quenching mechanism is attributed to the formation of a stable 1:1 adduct between BNOH and PA, driven by π-π stacking and light-to-charge transfer. In addition, our results demonstrate the practical application of BNOH for field sensing as it can effectively detect PA in both solution and powder forms, which demonstrates the great potential of BNOH for homeland security and explosives detection efforts.

3.pH Sensing Array (pC) Using Two Probes (CH and CYTYR):

In the next study, we designed two pH-sensitive probes, CH and CYTYR. CH has aggregation-induced emission (AIE) properties and produces red-shifted fluorescence under alkaline conditions with a new emission peak at 655 nm. When combined in nanomicelles, CH and CYTYR produce a FRET effect under alkaline conditions. This combination led to the

development of the pH sensing array pC, enabling sensitive pH detection and extending the pH measurement range from 5.25 to 9.05. Notably, we validated the ability of the pC to differentiate between a variety of commercially available anti-aging creams within 15 minutes, demonstrating its great potential in the cosmetic safety industry for identifying product origin and quality.

4. Clinical Liposome CST for Hypochlorous Acid Detection:

In our research initiatives, we designed and synthesized two probes, Se-TPA and CYLYS, characterizing their properties and applications. Se-TPA demonstrated Aggregation-Induced Emission (AIE) characteristics in water, with an emission peak corresponding to CYLYS. These probes were utilized to create a clinical liposome CST with a FRET effect, enabling the ratio metric detection of hypochlorous acid. This approach covered a broad detection range and achieved an impressive limit of detection as low as 17.5 nM. Further investigations through DFT calculations and mass spectrometry confirmed the response mechanism. Se-TPA, CYLYS, and CST displayed excellent selectivity and stability, reinforcing the significant potential of CST for hypochlorite detection and its potential applications in rheumatoid arthritis imaging.

Collectively, our collaborative efforts in developing and utilizing these various fluorescent probes have made significant contributions to the fields of chemical sensing, diagnostics, security, and environmental monitoring. The unique properties of each probe, along with their promising detection capabilities, offer a wide range of applications, from early disease detection to homeland security and cosmetics quality assurance. Our work underscores the vital role of tailored fluorescent probes in advancing scientific research and addressing real-world challenges.

Reference

[1] M. Montalti, A. Credi, L. Prodi, M.T. Gandolfi, Handbook of photochemistry: CRC press; 2006.

[2] J.R. Lakowicz, Principles of fluorescence spectroscopy: Springer; 2006.

[3] C.A. Combs, H. Shroff, Fluorescence microscopy: a concise guide to current imaging methods, Current protocols in neuroscience, 79(2017) 2.1. -2.1. 25.

[4] J. Singh, Optical properties of condensed matter and applications: John Wiley & Sons; 2006.

[5] S. Kawata, M. Ohtsu, M. Irie, Nano-optics: Springer Science & Business Media; 2002.

[6] Z. Chen, V. Stepanenko, V. Dehm, P. Prins, L.D. Siebbeles, J. Seibt, et al., Photoluminescence and conductivity of self-assembled π–π stacks of perylene bisimide dyes, Chemistry–A European Journal, 13(2007) 436-49.

[7] Z. Lou, P. Li, P. Song, K. Han, Ratiometric fluorescence imaging of cellular hypochlorous acid based on heptamethine cyanine dyes, Analyst, 138(2013) 6291-5.

[8] M. Sun, H. Yu, H. Zhu, F. Ma, S. Zhang, D. Huang, et al., Oxidative cleavage-based near-infrared fluorescent probe for hypochlorous acid detection and myeloperoxidase activity evaluation, Anal. Chem., 86(2014) 671-7.

[9] H. Li, L. Guan, X. Zhang, H. Yu, D. Huang, M. Sun, et al., A cyanine-based near-infrared fluorescent probe for highly sensitive and selective detection of hypochlorous acid and bioimaging, Talanta, 161(2016) 592-8.

[10] Y. Yang, S. Wang, L. Lu, Q. Zhang, P. Yu, Y. Fan, et al., NIR-II Chemiluminescence Molecular Sensor for In Vivo High-Contrast Inflammation Imaging, Angew. Chem. Int. Ed. Engl., 59(2020) 18380-5.

[11] D.J. Butcher, Atomic fluorescence spectrometry: A review of advances in instrumentation and novel applications, Applied spectroscopy reviews, 51(2016) 397-416.

[12] E. Sevick-Muraca, Translation of near-infrared fluorescence imaging technologies: emerging clinical applications, Annu. Rev. Med., 63(2012) 217-31.

[13] P. Ranford, Sir George Gabriel Stokes, Bart (1819–1903): his impact on science and scientists, Philosophical Transactions of the Royal Society A, 378(2020) 20190524.

[14] N. Mehraban, H.S. Freeman, Developments in PDT sensitizers for increased selectivity

and singlet oxygen production, Materials, 8(2015) 4421-56.

[15] F. Metz, Theory of intramolecular radiationless transitions: I. Discussion of Frank-Condon factors of large polyatomic molecules over the whole energy region, Chem. Phys., 18(1976) 385-99.

[16] J.L. Bricks, Y.L. Slominskii, I.D. Panas, A.P. Demchenko, Fluorescent J-aggregates of cyanine dyes: basic research and applications review, Methods Appl Fluoresc, 6(2017) 012001.

[17] C. Dou, Z. Ding, Z. Zhang, Z. Xie, J. Liu, L. Wang, Developing conjugated polymers with high electron affinity by replacing a C-C unit with a B<--N unit, Angew. Chem. Int. Ed. Engl., 54(2015) 3648-52.

[18] S. Kato, T. Matsumoto, T. Ishi-i, T. Thiemann, M. Shigeiwa, H. Gorohmaru, et al., Strongly red-fluorescent novel donor-pi-bridge-acceptor-pi-bridge-donor (D-pi-A-pi-D) type 2,1,3-benzothiadiazoles with enhanced two-photon absorption cross-sections, Chem. Commun., (2004) 2342-3.

[19] H. Li, D. Kim, Q. Yao, H. Ge, J. Chung, J. Fan, et al., Activity-Based NIR Enzyme Fluorescent Probes for the Diagnosis of Tumors and Image-Guided Surgery, Angew. Chem. Int. Ed. Engl., 60(2021) 17268-89.

[20] Y. Li, J. Hou, H. Zhou, M. Jia, S. Chen, H. Huang, et al., A fluorescence sensor array based on perylene probe monomer-excimer emission transition for the highly efficient differential sensing of metal ions and drinking waters, Sens. Actuators, B, 319(2020).

[21] J.M. Kovaleski, M.J. Wirth, Peer reviewed: applications of fluorescence recovery after photobleaching, Anal. Chem., 69(1997) 600A-5A.

[22] O. Brede, F. David, S. Steenken, Styrene triplets: Absorption spectra, lifetimes and quantum yields, J. Photochem. Photobiol. A: Chem., 97(1996) 127-31.

[23] R. Jiang, J. Dai, X. Dong, Q. Wang, Z. Meng, J. Guo, et al., Improving Image-Guided Surgical and Immunological Tumor Treatment Efficacy by Photothermal and Photodynamic Therapies Based on a Multifunctional NIR AIEgen, Adv. Mater., 33(2021) e2101158.

[24] T. Kubo, C. Katoh, K. Yamada, K. Okano, H. Tokuyama, T. Fukuyama, A mild inter- and intramolecular amination of aryl halides with a combination of CuI and CsOAc, Tetrahedron, 64(2008) 11230-6.

[25] B. Liscic, H.M. Tensi, L.C. Canale, G.E. Totten, Quenching theory and technology: CRC Press; 2010.

[26] M.R. Eftink, C.A. Ghiron, Fluorescence quenching studies with proteins, Anal. Biochem., 114(1981) 199-227.

[27] J. ZHANG, P. ZHANG, W. LIU, C.N. ZHANG, Y. LI, Z. HUANG, PHOTO BLANCHING OF HYPOCRELLIN B AND PHOTODAMAGE OF GELATIN IN AQUEOUS SOLUTION, Advances In Biomedical Photonics And Imaging, World Scientific2008, pp. 284-7.

[28] A. Samanta, Solvation dynamics in ionic liquids: what we have learned from the dynamic fluorescence stokes shift studies, The Journal of Physical Chemistry Letters, 1(2010) 1557-62.

[29] E.A. Jares-Erijman, T.M. Jovin, FRET imaging, Nat. Biotechnol., 21(2003) 1387-95.

[30] R. Roy, S. Hohng, T. Ha, A practical guide to single-molecule FRET, Nat. Methods, 5(2008) 507-16.

[31] C. Berney, G. Danuser, FRET or no FRET: a quantitative comparison, Biophys. J., 84(2003) 3992-4010.

[32] D.W. Piston, G.-J. Kremers, Fluorescent protein FRET: the good, the bad and the ugly, Trends Biochem. Sci, 32(2007) 407-14.

[33] G.W. Ewing, Instrumental methods of chemical analysis, (1960).

[34] M. Chalfie, Y. Tu, G. Euskirchen, W.W. Ward, D.C. Prasher, Green fluorescent protein as a marker for gene expression, Science, 263(1994) 802-5.

[35] S.Y. Lim, W. Shen, Z. Gao, Carbon quantum dots and their applications, Chem. Soc. Rev., 44(2015) 362-81.

[36] B.S. Arslan, B. Arkan, M. Gezgin, Y. Derin, D. Avcı, A. Tutar, et al., The improvement of photovoltaic performance of quinoline-based dye-sensitized solar cells by modification of the auxiliary acceptors, J. Photochem. Photobiol. A: Chem., 404(2021).

[37] M. Li, H. Chen, S. Li, G. Wang, F. Wei, X. Guo, et al., Active Self-Assembled Monolayer Sensors for Trace Explosive Detection, Langmuir, 36(2020) 1462-6.

[38] W. Xu, D. Wang, B.Z. Tang, NIR-II AIEgens: A Win-Win Integration towards Bioapplications, Angew. Chem. Int. Ed. Engl., 60(2021) 7476-87.

[39] H.E. Hackney, M. Paladino, H. Fu, D.G. Hall, Diazaboryl-naphthyl-ketone: A New

Scaffold with Bright Fluorescence, Aggregation-Induced Emission, and Application in the Quantitation of Trace Boronic Acids in Drug Intermediates, Chemistry, 26(2020) 14324-9.

[40] J.H. Kim, J.H. Yun, J.Y. Lee, Recent Progress of Highly Efficient Red and Near-Infrared Thermally Activated Delayed Fluorescent Emitters, Advanced Optical Materials, 6(2018).

[41] B. Li, M. Zhao, F. Zhang, Rational Design of Near-Infrared-II Organic Molecular Dyes for Bioimaging and Biosensing, ACS Materials Letters, 2(2020) 905-17.

[42] Z. Sheng, B. Guo, D. Hu, S. Xu, W. Wu, W.H. Liew, et al., Bright Aggregation-Induced-Emission Dots for Targeted Synergetic NIR-II Fluorescence and NIR-I Photoacoustic Imaging of Orthotopic Brain Tumors, Adv. Mater., (2018) e1800766.

[43] X. Chai, H.H. Han, A.C. Sedgwick, N. Li, Y. Zang, T.D. James, et al., Photochromic Fluorescent Probe Strategy for the Super-resolution Imaging of Biologically Important Biomarkers, J. Am. Chem. Soc., 142(2020) 18005-13.

[44] F. da Silva Miranda, A.M. Signori, J. Vicente, B. de Souza, Jacks P. Priebe, B. Szpoganicz, et al., Synthesis of substituted dipyrido[3,2-a:2′,3′-c]phenazines and a new heterocyclic dipyrido[3,2-f:2′,3′-h]quinoxalino[2,3-b]quinoxaline, Tetrahedron, 64(2008) 5410-5.

[45] P. Gao, W. Pan, N. Li, B. Tang, Fluorescent probes for organelle-targeted bioactive species imaging, Chem Sci, 10(2019) 6035-71.

[46] D. Li, C.B. Patel, G. Xu, A. Iagaru, Z. Zhu, L. Zhang, et al., Visualization of Diagnostic and Therapeutic Targets in Glioma With Molecular Imaging, Frontiers in Immunology, 11(2020).

[47] S. Liang, X. Deng, P. Ma, Z. Cheng, J. Lin, Recent Advances in Nanomaterial-Assisted Combinational Sonodynamic Cancer Therapy, Adv. Mater., (2020) e2003214.

[48] M.K. Lowery, A.J. Starshak, J.N. Esposito, P.C. Krueger, M.E. Kenney, Dichloro(phthalocyanino)silicon, Inorg. Chem., 4(1965) 128-.

[49] J.A. Ludwig, J.N. Weinstein, Biomarkers in cancer staging, prognosis and treatment selection, Nat. Rev. Cancer, 5(2005) 845-56.

[50] W. Mao, J. Tang, L. Dai, X. He, J. Li, L. Cai, et al., A general strategy to design highly fluorogenic far-red and near-infrared tetrazine bioorthogonal probes, Angew. Chem. Int. Ed. Engl., (2020).

[51] F. Ren, H. Liu, H. Zhang, Z. Jiang, B. Xia, C. Genevois, et al., Engineering NIR-IIb fluorescence of Er-based lanthanide nanoparticles for through-skull targeted imaging and imaging-guided surgery of orthotopic glioma, Nano Today, 34(2020).

[52] E. Wagner-Wysiecka, Mid-infrared spectroscopy for characterization of Baltic amber (succinite), Spectrochim Acta A Mol Biomol Spectrosc, 196(2018) 418-31.

[53] H. Wan, H. Ma, S. Zhu, F. Wang, Y. Tian, R. Ma, et al., Developing a Bright NIR-II Fluorophore with Fast Renal Excretion and Its Application in Molecular Imaging of Immune Checkpoint PD-L1, Adv. Funct. Mater., 28(2018).

[54] W. Wang, Y. Kong, J. Jiang, Q. Xie, Y. Huang, G. Li, et al., Engineering the Protein Corona Structure on Gold Nanoclusters Enables Red-Shifted Emissions in the Second Near-infrared Window for Gastrointestinal Imaging, Angew. Chem. Int. Ed. Engl., (2020).

[55] W. Wang, Y. Kong, J. Jiang, Q. Xie, Y. Huang, G. Li, et al., Engineering the Protein Corona Structure on Gold Nanoclusters Enables Red-Shifted Emissions in the Second Near-infrared Window for Gastrointestinal Imaging, Angew. Chem. Int. Ed. Engl., 59(2020) 22431-5.

[56] L. Wu, A.C. Sedgwick, X. Sun, S.D. Bull, X.P. He, T.D. James, Reaction-Based Fluorescent Probes for the Detection and Imaging of Reactive Oxygen, Nitrogen, and Sulfur Species, Acc. Chem. Res., 52(2019) 2582-97.

[57] P. He, Y. Chen, X.N. Li, Y.Y. Yan, C. Liu, Aggregation-Induced Emission-Active Iridium(III) Complexes for Sensing Picric Acid in Water, Chemosensors, 11(2023).

[58] J.S. Liu, T. Fu, C.F. Liu, F.F. Wu, H.X. Wang, Sensitive detection of picric acid in an aqueous solution using fluorescent nonconjugated polymer dots as fluorescent probes, Nanotechnology, 32(2021).

[59] F. Neese, Software update: the ORCA program system, version 4.0, Wiley Interdisciplinary Reviews: Computational Molecular Science, 8(2018) e1327.

[60] K. Patir, B. Barman, S. Basumatary, One Pot Synthesis of Multicolor Emissive Nitrogen Doped Carbon Dots and its Application as Acetone and Picric Acid Sensor, Iranian Journal of Science and Technology Transaction a-Science, 45(2021) 1301-10.

[61] A. Pagoto, F. Garello, G.M. Marini, M. Tripepi, F. Arena, P. Bardini, et al., Novel Gastrin-Releasing Peptide Receptor Targeted Near-Infrared Fluorescence Dye for Image-Guided

Surgery of Prostate Cancer, Mol Imaging Biol, 22(2020) 85-93.

[62] J. Qi, C. Sun, D. Li, H. Zhang, W. Yu, A. Zebibula, et al., Aggregation-Induced Emission Luminogen with Near-Infrared-II Excitation and Near-Infrared-I Emission for Ultradeep Intravital Two-Photon Microscopy, ACS Nano, 12(2018) 7936-45.

[63] S. Dey, A. Saha, P. Kumar, C. Kar, S. Chakraborty, P.K. Sukul, Self-assembled nanomaterials of naphthalene monoimide in aqueous medium for multimodal detection of picric acid, J. Photochem. Photobiol. A: Chem., 423(2022).

[64] M.H. Lim, D. Xu, S.J. Lippard, Visualization of nitric oxide in living cells by a copper-based fluorescent probe, Nat. Chem. Biol., 2(2006) 375-80.

[65] T. Malinski, Z. Taha, Nitric oxide release from a single cell measured in situ by a porphyrinic-based microsensor, Nature, 358(1992) 676-8.

[66] W.H. Chen, G.F. Luo, X.Z. Zhang, Recent Advances in Subcellular Targeted Cancer Therapy Based on Functional Materials, Adv. Mater., 31(2019) e1802725.

[67] L. Chen, D. Wu, J.M. Kim, J. Yoon, An ESIPT-Based Fluorescence Probe for Colorimetric, Ratiometric, and Selective Detection of Phosgene in Solutions and the Gas Phase, Anal. Chem., 89(2017) 12596-601.

[68] Z. Mao, H. Jiang, X. Song, W. Hu, Z. Liu, Development of a Silicon-Rhodamine Based Near-Infrared Emissive Two-Photon Fluorescent Probe for Nitric Oxide, Anal. Chem., 89(2017) 9620-4.

[69] Y. Shen, Q. Zhang, X. Qian, Y. Yang, Practical assay for nitrite and nitrosothiol as an alternative to the Griess assay or the 2,3-diaminonaphthalene assay, Anal. Chem., 87(2015) 1274-80.

[70] E. Sasaki, H. Kojima, H. Nishimatsu, Y. Urano, K. Kikuchi, Y. Hirata, et al., Highly sensitive near-infrared fluorescent probes for nitric oxide and their application to isolated organs, J. Am. Chem. Soc., 127(2005) 3684-5.

[71] Y. Yang, S.K. Seidlits, M.M. Adams, V.M. Lynch, C.E. Schmidt, E.V. Anslyn, et al., A highly selective low-background fluorescent imaging agent for nitric oxide, J. Am. Chem. Soc., 132(2010) 13114-6.

[72] D. Fukumura, S. Kashiwagi, R.K. Jain, The role of nitric oxide in tumour progression, Nat.

Rev. Cancer, 6(2006) 521-34.

[73] L.E. McQuade, J. Ma, G. Lowe, A. Ghatpande, A. Gelperin, S.J. Lippard, Visualization of nitric oxide production in the mouse main olfactory bulb by a cell-trappable copper(II) fluorescent probe, Proc Natl Acad Sci U S A, 107(2010) 8525-30.

[74] C.G. Dai, J.L. Wang, Y.L. Fu, H.P. Zhou, Q.H. Song, Selective and Real-Time Detection of Nitric Oxide by a Two-Photon Fluorescent Probe in Live Cells and Tissue Slices, Anal. Chem., 89(2017) 10511-9.

[75] H. Kojima, N. Nakatsubo, K. Kikuchi, S. Kawahara, Y. Kirino, H. Nagoshi, et al., Detection and imaging of nitric oxide with novel fluorescent indicators: diaminofluoresceins, Anal. Chem., 70(1998) 2446-53.

[76] H. Kojima, Y. Urano, K. Kikuchi, T. Higuchi, Y. Hirata, T. Nagano, Fluorescent Indicators for Imaging Nitric Oxide Production, Angew. Chem. Int. Ed. Engl., 38(1999) 3209-12.

[77] K. Liu, X. Kong, Y. Ma, W. Lin, Rational Design of a Robust Fluorescent Probe for the Detection of Endogenous Carbon Monoxide in Living Zebrafish Embryos and Mouse Tissue, Angew. Chem. Int. Ed. Engl., 56(2017) 13489-92.

[78] X. Yang, Y. Guo, R.M. Strongin, Conjugate addition/cyclization sequence enables selective and simultaneous fluorescence detection of cysteine and homocysteine, Angew. Chem. Int. Ed. Engl., 50(2011) 10690-3.

[79] J. Miao, Y. Huo, X. Lv, Z. Li, H. Cao, H. Shi, et al., Fast-response and highly selective fluorescent probes for biological signaling molecule NO based on N-nitrosation of electron-rich aromatic secondary amines, Biomaterials, 78(2016) 11-9.

[80] Z. Huang, S. Ding, D. Yu, F. Huang, G. Feng, Aldehyde group assisted thiolysis of dinitrophenyl ether: a new promising approach for efficient hydrogen sulfide probes, Chem. Commun., 50(2014) 9185-7.

[81] F.C. Fang, Antimicrobial reactive oxygen and nitrogen species: concepts and controversies, Nat. Rev. Microbiol., 2(2004) 820-32.

[82] N. Gupta, S. Imam Reja, V. Bhalla, M. Gupta, G. Kaur, M. Kumar, An Approach for the Selective Detection of Nitric Oxide in Biological Systems: An in vitro and in vivo Perspective, Chem Asian J, 11(2016) 1020-7.

[83] C.C. Chang, F. Wang, J. Qiang, Z.J. Zhang, Y.H. Chen, W. Zhang, et al., Benzothiazole-based fluorescent sensor for hypochlorite detection and its application for biological imaging, Sens. Actuators, B, 243(2017) 22-8.

[84] T. Nagano, T. Yoshimura, Bioimaging of nitric oxide, Chem. Rev., 102(2002) 1235-70.

[85] A.C. Sedgwick, X. Sun, G. Kim, J. Yoon, S.D. Bull, T.D. James, Boronate based fluorescence (ESIPT) probe for peroxynitrite, Chem. Commun., 52(2016) 12350-2.

[86] M.H. Lim, S.J. Lippard, Copper complexes for fluorescence-based NO detection in aqueous solution, J. Am. Chem. Soc., 127(2005) 12170-1.

[87] M.D. Laramie, A. Levitz, M. Henary, Cyanine and Squaric Acid Metal Sensors, Sens. Actuators, B, 243(2017) 1191-204.

[88] M.R. Weng, X. Yang, Y. Ni, C.C. Xu, H. Zhang, J.J. Shao, et al., Deep-red fluorogenic probe for rapid detection of nitric oxide in Parkinson's disease models, Sens. Actuators, B, 283(2019) 769-75.

[89] S. Ma, D.C. Fang, B. Ning, M. Li, L. He, B. Gong, The rational design of a highly sensitive and selective fluorogenic probe for detecting nitric oxide, Chem. Commun., 50(2014) 6475-8.

[90] X. Lv, Y. Wang, S. Zhang, Y. Liu, J. Zhang, W. Guo, A specific fluorescent probe for NO based on a new NO-binding group, Chem. Commun., 50(2014) 7499-502.

[91] A. Beltran, M.I. Burguete, D.R. Abanades, D. Perez-Sala, S.V. Luis, F. Galindo, Turn-on fluorescent probes for nitric oxide sensing based on the ortho-hydroxyamino structure showing no interference with dehydroascorbic acid, Chem. Commun., 50(2014) 3579-81.

[92] L. Chen, D. Wu, C.S. Lim, D. Kim, S.J. Nam, W. Lee, et al., A two-photon fluorescent probe for specific detection of hydrogen sulfide based on a familiar ESIPT fluorophore bearing AIE characteristics, Chem. Commun., 53(2017) 4791-4.

[93] C. Sun, W. Shi, Y. Song, W. Chen, H. Ma, An unprecedented strategy for selective and sensitive fluorescence detection of nitric oxide based on its reaction with a selenide, Chem. Commun., 47(2011) 8638-40.

[94] T. Gao, P. Xu, M. Liu, A. Bi, P. Hu, B. Ye, et al., A water-soluble ESIPT fluorescent probe with high quantum yield and red emission for ratiometric detection of inorganic and organic palladium, Chem Asian J, 10(2015) 1142-5.

[95] X. Li, X. Gao, W. Shi, H. Ma, Design strategies for water-soluble small molecular chromogenic and fluorogenic probes, Chem. Rev., 114(2014) 590-659.

[96] Z. Dai, L. Tian, B. Song, X. Liu, J. Yuan, Development of a novel lysosome-targetable time-gated luminescence probe for ratiometric and luminescence lifetime detection of nitric oxide in vivo, Chem Sci, 8(2017) 1969-76.

[97] L. Yuan, W. Lin, Y. Xie, B. Chen, J. Song, Development of a ratiometric fluorescent sensor for ratiometric imaging of endogenously produced nitric oxide in macrophage cells, Chem. Commun., 47(2011) 9372-4.

[98] C. Gao, L. Lin, W. Sun, Z.L. Tan, J.R. Huang, L. He, et al., Dihydropyridine-derived BODIPY probe for detecting exogenous and endogenous nitric oxide in mitochondria, Talanta, 176(2018) 382-8.

[99] M.H. Lim, B.A. Wong, W.H. Pitcock, Jr., D. Mokshagundam, M.H. Baik, S.J. Lippard, Direct nitric oxide detection in aqueous solution by copper(II) fluorescein complexes, J. Am. Chem. Soc., 128(2006) 14364-73.

[100] S.K. Mohan Nalluri, J. Zhou, T. Cheng, Z. Liu, M.T. Nguyen, T. Chen, et al., Discrete Dimers of Redox-Active and Fluorescent Perylene Diimide-Based Rigid Isosceles Triangles in the Solid State, J. Am. Chem. Soc., 141(2019) 1290-303.

[101] F. Bedioui, N. Villeneuve, Electrochemical nitric oxide sensors for biological samples - Principle, selected examples and applications, Electroanalysis, 15(2003) 5-18.

[102] L. Chen, D. Wu, J. Yoon, An ESIPT based fluorescence probe for ratiometric monitoring of nitric oxide, Sens. Actuators, B, 259(2018) 347-53.

[103] J. Zhao, S. Ji, Y. Chen, H. Guo, P. Yang, Excited state intramolecular proton transfer (ESIPT): from principal photophysics to the development of new chromophores and applications in fluorescent molecular probes and luminescent materials, Phys. Chem. Chem. Phys., 14(2012) 8803-17.

[104] D. Wu, J.C. Ryu, Y.W. Chung, D. Lee, J.H. Ryu, J.H. Yoon, et al., A Far-Red-Emitting Fluorescence Probe for Sensitive and Selective Detection of Peroxynitrite in Live Cells and Tissues, Anal. Chem., 89(2017) 10924-31.

[105] M. Wang, Z.C. Xu, X. Wang, J.N. Cui, A fluorescent and colorimetric chemosensor for

nitric oxide based on 1,8-naphthalimide, Dyes and Pigments, 96(2013) 333-7.

[106] D. Wu, A.C. Sedgwick, T. Gunnlaugsson, E.U. Akkaya, J. Yoon, T.D. James, Fluorescent chemosensors: the past, present and future, Chem. Soc. Rev., 46(2017) 7105-23.

[107] D. Wu, L. Chen, N. Kwon, J. Yoon, Fluorescent Probes Containing Selenium as a Guest or Host, Chem, 1(2016) 674-98.

[108] H.B. Yu, L.J. Jin, Y. Dai, H.Q. Li, Y. Xiao, From a BODIPY-rhodamine scaffold to a ratiometric fluorescent probe for nitric oxide, New J. Chem., 37(2013) 1688-91.

[109] F. Hou, L. Zhu, H. Zhang, Z. Qiao, N. Wei, Y. Zhang, A high selective and sensitive fluorescence probe based on chromone fluorophore for imaging H 2 S in living cells, New J. Chem., (2020).

[110] H.X. Zhang, J.B. Chen, X.F. Guo, H. Wang, H.S. Zhang, Highly sensitive determination of nitric oxide in biologic samples by a near-infrared BODIPY-based fluorescent probe coupled with high-performance liquid chromatography, Talanta, 116(2013) 335-42.

[111] Y. Gabe, Y. Urano, K. Kikuchi, H. Kojima, T. Nagano, Highly sensitive fluorescence probes for nitric oxide based on boron dipyrromethene chromophore-rational design of potentially useful bioimaging fluorescence probe, J. Am. Chem. Soc., 126(2004) 3357-67.

[112] H.X. Zhang, J.B. Chen, X.F. Guo, H. Wang, H.S. Zhang, Highly sensitive low-background fluorescent probes for imaging of nitric oxide in cells and tissues, Anal. Chem., 86(2014) 3115-23.

[113] H. Li, D. Zhang, M. Gao, L. Huang, L. Tang, Z. Li, et al., Highly specific C-C bond cleavage induced FRET fluorescence for in vivo biological nitric oxide imaging, Chem Sci, 8(2017) 2199-203.

[114] A. Diaz, M. Ortiz, I. Sanchez, R. Cao, A. Mederos, J. Sanchiz, et al., Interactions of nitric oxide with copper(II) dithiocarbamates in aqueous solution, J. Inorg. Biochem., 95(2003) 283-90.

[115] X. Zhang, W.S. Kim, N. Hatcher, K. Potgieter, L.L. Moroz, R. Gillette, et al., Interfering with nitric oxide measurements. 4,5-diaminofluorescein reacts with dehydroascorbic acid and ascorbic acid, J. Biol. Chem., 277(2002) 48472-8.

[116] H. Yu, Y. Xiao, L. Jin, A lysosome-targetable and two-photon fluorescent probe for

monitoring endogenous and exogenous nitric oxide in living cells, J. Am. Chem. Soc., 134(2012) 17486-9.

[117] L.E. McQuade, M.D. Pluth, S.J. Lippard, Mechanism of nitric oxide reactivity and fluorescence enhancement of the NO-specific probe CuFL1, Inorg. Chem., 49(2010) 8025-33.

[118] C. Szabo, Multiple pathways of peroxynitrite cytotoxicity, Toxicol. Lett., 140-141(2003) 105-12.

[119] D. Wu, Y.Z. Shen, J.H. Chen, G.T. Liu, H.Y. Chen, J. Yin, Naphthalimide-modified near-infrared cyanine dye with a large stokes shift and its application in bioimaging, Chin. Chem. Lett., 28(2017) 1979-82.

[120] R.K. Gupta, S.K. Pathak, B. Pradhan, D.S. Shankar Rao, S. Krishna Prasad, A.S. Achalkumar, Self-assembly of luminescent N-annulated perylene tetraesters into fluid columnar phases, Soft Matter, 11(2015) 3629-36.

[121] C. Xue, R. Sun, R. Annab, D. Abadi, S. Jin, Perylene monoanhydride diester: a versatile intermediate for the synthesis of unsymmetrically substituted perylene tetracarboxylic derivatives, Tetrahedron Lett., 50(2009) 853-6.

[122] D.K. Wang, M. Wang, K.X. Chen, Y.J. You, J. Zhang, X.H. Zhou, et al., A dual functional 1D Cd-based coordination polymer for the highly luminescent sensitive detection of Fe3+ and picric acid, Appl. Organomet. Chem., 34(2020).

[123] M. Fabin, M. Lapkowski, T. Jarosz, Methods for Detecting Picric Acid-A Review of Recent Progress, Applied Sciences-Basel, 13(2023).

[124] P.F. Fan, C. Liu, Q.J. Li, C.C. Hu, X.W. Wu, X.H. Zhang, et al., Microwave-assisted rapid synthesis of ovalbumin-stabilized gold nanoclusters for picric acid determination, Journal of Central South University, 30(2023) 74-84.

[125] A. Abbasi, M. Shakir, Simple One-step Solid-state Synthesis of Highly Crystalline N Doped Carbon Dots As Selective Turn Off-sensor for Picric Acid and Metanil Yellow, Journal of Fluorescence, 32(2022) 1239-46.

[126] T. Santiwat, N. Sornkaew, K. Srikittiwanna, M. Sukwattanasinitt, N. Niamnont, Electrospun nanofiber sheets mixed with a novel triphenylamine-pyrenyl salicylic acid fluorophore for the selective detection of picric acid, Journal of Photochemistry and

Photobiology a-Chemistry, 434(2023).

[127] R.M. Farsi, N.M. Alharbi, F.S. Basingab, N.M. Nass, S.Y. Qattan, S.A. Hassoubah, et al., Biodegradation of picric acid (2,4,6-trinitrophenol, TNP) by free and immobilized marine Enterococcus thailandicus isolated from the red sea, Saudi Arabia, Egyptian Journal of Aquatic Research, 47(2021) 307-12.

[128] R. Beeram, V.S. Vendamani, V.R. Soma, Deep learning approach to overcome signal fluctuations in SERS for efficient On-Site trace explosives detection, Spectrochimica Acta Part a-Molecular and Biomolecular Spectroscopy, 289(2023).

[129] D.Y. Lin, R.L. Dong, P. Li, S.F. Li, M.H. Ge, Y.F. Zhang, et al., A novel SERS selective detection sensor for trace trinitrotoluene based on meisenheimer complex of monoethanolamine molecule, Talanta, 218(2020).

[130] R.W. Madden, J. Mahdavieh, R.C. Smith, R. Subramanian, An explosives detection system for airline security using coherent x-ray scattering technology, Conference on Hard X-Ray, Gamma-Ray, and Neutron Detector Physics X, San Diego, CA, 2008.

[131] F.F. Tian, J. Yu, J.L. Hu, Y. Zhang, M.X. Xie, Y. Liu, et al., Determination of emulsion explosives with Span-80 as emulsifier by gas chromatography-mass spectrometry, J. Chromatogr. A, 1218(2011) 3521-8.

[132] M.A.C. Hartel, T.M. Klapotke, J. Stierstorfer, L. Zehetner, Vapor Pressure of Linear Nitrate Esters Determined by Transpiration Method in Combination with VO-GC/MS, Propellants Explosives Pyrotechnics, 44(2019) 484-92.

[133] T.H. Bunning, J.S. Strehse, A.C. Hollmann, T. Botticher, E. Maser, A Toolbox for the Determination of Nitroaromatic Explosives in Marine Water, Sediment, and Biota Samples on Femtogram Levels by GC-MS/MS, Toxics, 9(2021).

[134] M.C. Monti, D.A. Alexson, J.K. Okamitsu, NQR detection of explosive simulants using RF atomic magnetometers, Conference on Detection and Sensing of Mines, Explosive Objects, and Obscured Targets XXI, Baltimore, MD, 2016.

[135] T. Nichols, S. Gidcumb, T. Ketterl, G. Brauns, A Portable Discrete Frequency NQR Explosives Detection System, Conference on Detection and Sensing of Mines, Explosive Objects, and Obscured Targets XXIV, Baltimore, MD, 2019.

[136] P. Hemnani, A.K. Rajarajan, G. Joshi, S.V.G. Ravindranath, Ieee, N-14 NQR spectrometer for explosive detection: A Review, International Conference on Automatic Control and Dynamic Optimization Techniques (ICACDOT), Int Inst Informat Technol, Pune, INDIA, 2016, pp. 1120-5.

[137] T.M. Osan, L.M.C. Cerioni, J. Forguez, J.M. Olle, D.J. Pusiol, NQR: From imaging to explosives and drugs detection, Physica B-Condensed Matter, 389(2007) 45-50.

[138] A. Konnai, T. Asaji, H. Nohmi, N. Odano, Development of NQR explosive detection technique for transportation security, Science and Technology of Energetic Materials, 70(2009) 55-61.

[139] C. Fuche, J. Deseille, Ion mobility spectrometry: a tool to detect narcotics and explosives, Actualite Chimique, (2010) 91-5.

[140] T.L. Buxton, P.D. Harrington, Trace explosive detection in aqueous samples by solid-phase extraction ion mobility spectrometry (SPE-IMS), Appl. Spectrosc., 57(2003) 223-32.

[141] L.V. Haley, J.M. Romeskie, GC-IMS: A technology for many applications, Conference on Enforcement and Security Technologies, Boston, Ma, 1998, pp. 375-83.

[142] J.M. Perr, K.G. Furton, J.R. Almirall, Application of a SPME-IMS detection system for explosives detection, Conference on Sensors, and Command, Control, Communications, and Intelligence (C31) Technologies for Homeland Security and Homeland Defense IV, Orlando, FL, 2005, pp. 667-72.

[143] A. Zalewska, W. Pawlowski, W. Tomaszewski, Limits of detection of explosives as determined with IMS and field asymmetric IMS vapour detectors, Forensic Sci. Int., 226(2013) 168-72.

[144] W. Huang, E. Smarsly, J.S. Han, M. Bender, K. Seehafer, I. Wacker, et al., Truxene-Based Hyperbranched Conjugated Polymers: Fluorescent Micelles Detect Explosives in Water, Acs Applied Materials & Interfaces, 9(2017) 3068-74.

[145] W.J. Peveler, A. Roldan, N. Hollingsworth, M.J. Porter, I.P. Parkin, Multichannel Detection and Differentiation of Explosives with a Quantum Dot Array, Acs Nano, 10(2016) 1139-46.

[146] X.H. Wang, Y.Z. Guo, D. Li, H. Chen, R.C. Sun, Fluorescent amphiphilic cellulose

nanoaggregates for sensing trace explosives in aqueous solution, Chem. Commun., 48(2012) 5569-71.

[147] Y. Salinas, R. Martinez-Manez, M.D. Marcos, F. Sancenon, A.M. Costero, M. Parra, et al., Optical chemosensors and reagents to detect explosives, Chem. Soc. Rev., 41(2012) 1261-96.

[148] W.F. Shu, C.W. Guan, W.H. Guo, C.Y. Wang, Y.J. Shen, Conjugated poly(aryleneethynylenesiloles) and their application in detecting explosives, J. Mater. Chem., 22(2012) 3075-81.

[149] C.E. Hay, J. Lee, D.S. Silvester, A methodology to detect explosive residues using a gelled ionic liquid based field-deployable electrochemical device, J. Electroanal. Chem., 872(2020).

[150] B. Ju, Y. Wang, Y.M. Zhang, T. Zhang, Z.H. Lu, M.J. Li, et al., Photostable and Low-Toxic Yellow-Green Carbon Dots for Highly Selective Detection of Explosive 2,4,6-Trinitrophenol Based on the Dual Electron Transfer Mechanism, Acs Applied Materials & Interfaces, 10(2018) 13040-7.

[151] X.K. Tian, H. Peng, Y. Li, C. Yang, Z.X. Zhou, Y.X. Wang, Highly sensitive and selective paper sensor based on carbon quantum dots for visual detection of TNT residues in groundwater, Sens. Actuators, B, 243(2017) 1002-9.

[152] H.H. Fan, G.Q. Xiang, Y.L. Wang, H. Zhang, K.K. Ning, J.Y. Duan, et al., Manganese-doped carbon quantum dots-based fluorescent probe for selective and sensitive sensing of 2,4,6-trinitrophenol via an inner filtering effect, Spectrochimica Acta Part a-Molecular and Biomolecular Spectroscopy, 205(2018) 221-6.

[153] F.B. Sen, N. Begic, M. Bener, R. Apak, Fluorescence turn-off sensing of TNT by polyethylenimine capped carbon quantum dots, Spectrochimica Acta Part a-Molecular and Biomolecular Spectroscopy, 271(2022).

[154] F. Ghasemi, M.R. Hormozi-Nezhad, Determination and identification of nitroaromatic explosives by a double-emitter sensor array, Talanta, 201(2019) 230-6.

[155] M. Yang, J.F. Xu, H.H. Ma, M.Z. Lei, X.J. Ni, Z.W. Shen, et al., Microstructure development during explosive welding of metal foil: morphologies, mechanical behaviors and mechanisms, Composites Part B-Engineering, 212(2021).

[156] O. Adegoke, N.N. Daeid, Colorimetric optical nanosensors for trace explosive detection using metal nanoparticles: advances, pitfalls, and future perspective, Emerging Topics in Life Sciences, 5(2021) 367-79.

[157] X.W. Yan, M. Gharib, L. Esrafili, S.J. Wang, K.G. Liu, A. Morsali, Ultrasound Irradiation Assisted Synthesis of Luminescent Nano Amide-Functionalized Metal-Organic Frameworks; Application Toward Phenol Derivatives Sensing, Frontiers in Chemistry, 10(2022).

[158] D. Kotsikau, M. Ivanovskaya, Metal oxide semiconductor sensors for detection of toxic and explosive gases, NATO Advanced Research Workshop on Electronic Noses and Sensors for the Detection of Explosives, Warwick, ENGLAND, 2003, pp. 93-115.

[159] Z. Zhao, X.J. Li, G. Tao, C.X. Du, CuCr bulk alloy produced by mechanical alloying and explosive compaction, Transactions of Nonferrous Metals Society of China, 19(2009) S626-S9.

[160] J.H. Lee, S. Kang, J.Y. Lee, J. Jaworski, J.H. Jung, Instant Visual Detection of Picogram Levels of Trinitrotoluene by Using Luminescent Metal-Organic Framework Gel-Coated Filter Paper, Chemistry-a European Journal, 19(2013) 16665-71.

[161] X.Y. Feng, L.H. Zeng, D.T. Zou, Z.Z. Zhang, G.H. Zhong, S.Y. Peng, et al., Trace-doped metal-organic gels with remarkably enhanced luminescence, Rsc Advances, 7(2017) 37194-9.

[162] C. Wang, L. Tian, W. Zhu, S.Q. Wang, P. Wang, Y. Liang, et al., Dye@bio-MOF-1 Composite as a Dual-Emitting Platform for Enhanced Detection of a Wide Range of Explosive Molecules, Acs Applied Materials & Interfaces, 9(2017) 20076-85.

[163] L. Liu, R. Ding, Y.Y. Mao, B.Q. Sun, Theoretical investigations on the nitro-explosive sensing process of a MOF sensor: Roles of hydrogen bond and pi-pi stacking, Chem. Phys. Lett., 793(2022).

[164] S.J. Dong, J.S. Hu, K. Wu, M.D. Zheng, A Mg(II)-MOF as recyclable luminescent sensor for detecting TNP with high selectivity and sensitivity, Inorg. Chem. Commun., 95(2018) 111-6.

[165] L. Yang, Y.L. Liu, C.G. Liu, F. Ye, Y. Fu, A luminescent sensor based on a new Cd-MOF for nitro explosives and organophosphorus pesticides detection, Inorg. Chem. Commun., 122(2020).

[166] T.T. Wang, Y.Y. Jia, Q. Chen, R. Feng, S.Y. Tian, T.L. Hu, et al., A new luminescent metal-organic framework for selective sensing of nitroaromatic explosives, Science China-Chemistry, 59(2016) 959-64.

[167] D. Xincun, W. Guangfa, D. Zhuohua, Recent Progress in Colorimetric/fluorescent Sensing toward Improvised Explosives(Invited), Acta Photonica Sinica, 51(2022).

[168] G.H. Hong, C. Qian, P.C. Xue, X.L. Liu, Q.Q. Wang, M.Y. Liu, et al., Linear Oligocarbazole-Based Organogelators: Synthesis and Fluorescent Probing of Explosives, Eur. J. Org. Chem., 2014(2014) 6155-62.

[169] Y.T. Nguyen, S. Shin, K. Kwon, N. Kim, S.W. Bae, BODIPY-based fluorescent sensors for detection of explosives, Journal of Chemical Research, 47(2023).

[170] B. Liu, B.Z. Tang, Aggregation-Induced Emission: More Is Different, Angewandte Chemie-International Edition, 59(2020) 9788-9.

[171] Y.W. Lu, Y.Q. Tan, Y.Y. Gong, H. Li, W.Z. Yuan, Y.M. Zhang, et al., High efficiency D-A structured luminogen with aggregation-induced emission and mechanochromic characteristics, Chin. Sci. Bull., 58(2013) 2719-22.

[172] Y.Q. Dong, J.W.Y. Lam, A.J. Qin, Z. Li, J.X. Sun, H.S. Kwok, et al., Aggregation-induced emission, Conference on Organic Light Emitting Materials and Devices X, San Diego, CA, 2006.

[173] Y.F. Zuo, R.T.K. Kwok, J.W. Sun, J.W.Y. Lam, B.Z. Tang, Aggregation-Induced Emission Macromolecular Materials for Antibacterial Applications, Macromol. Rapid Commun., (2023).

[174] P.B. Han, H. Xu, Z.F. An, Z.Y. Cai, Z.X. Cai, H. Chao, et al., Aggregation-Induced Emission, Progress in Chemistry, 34(2022) 1-130.

[175] L. Xu, P. Li, Direct introduction of a naphthalene-1, 8-diamino boryl [B (dan)] group by a Pd-catalysed selective boryl transfer reaction, Chem. Commun., 51(2015) 5656-9.

[176] H. Kruse, S. Grimme, A geometrical correction for the inter-and intra-molecular basis set superposition error in Hartree-Fock and density functional theory calculations for large systems, The Journal of chemical physics, 136(2012) 154101.

[177] C.-Y. Lee, S.-J. Ahn, C.-H. Cheon, Protodeboronation of ortho-and para-phenol boronic acids and application to ortho and meta functionalization of phenols using boronic acids as

blocking and directing groups, The Journal of Organic Chemistry, 78(2013) 12154-60.

[178] S. Ding, Q. Ma, M. Zhu, H. Ren, S. Tian, Y. Zhao, et al., Direct Transformation from Arylamines to Aryl Naphthalene-1, 8-diamino Boronamides: A Metal-Free Sandmeyer-Type Process, Molecules, 24(2019) 377.

[179] W.M. Wan, D. Tian, Y.N. Jing, X.Y. Zhang, W. Wu, H. Ren, et al., NBN-Doped Conjugated Polycyclic Aromatic Hydrocarbons as an AIEgen Class for Extremely Sensitive Detection of Explosives, Angew. Chem. Int. Ed. Engl., 57(2018) 15510-6.

[180] C. Cheng, L. Chao-Yi, S.-A. SHAHZAD, Z. Hui-Peng, Y. Cong, J. Xing, Phenothiazine and BN-doped AIE probes integrated fluorescence sensor array for detection and discrimination of nitro explosives, Chinese Journal of Analytical Chemistry, 48(2020) e20075-e80.

[181] A. Chowdhury, P.S. Mukherjee, Electron-rich triphenylamine-based sensors for picric acid detection, The Journal of Organic Chemistry, 80(2015) 4064-75.

[182] A. Muise, S. Desmarais, Women's perceptions and use of "anti-aging" products, Sex Roles, 63(2010) 126-37.

[183] M.S. Ferreira, M.C. Magalhaes, J.M. Sousa-Lobo, I.F. Almeida, Trending Anti-Aging Peptides, Cosmetics, 7(2020).

[184] A.N. Zaid, R. Al Ramahi, Depigmentation and Anti-aging Treatment by Natural Molecules, Curr. Pharm. Des., 25(2019) 2292-312.

[185] N. Chondrogianni, S. Kapeta, I. Chinou, K. Vassilatou, I. Papassideri, E.S. Gonos, Anti-ageing and rejuvenating effects of quercetin, Experimental Gerontology, 45(2010) 763-71.

[186] R.H. Binstock, The war on "anti-aging medicine", Gerontologist, 43(2003) 4-14.

[187] S. Baydanoff, E. Konova, N. Ivanova, Determination of anti-AGE antibodies in human serum, Glycoconjugate J., 13(1996) 335-9.

[188] A. Muise, S. Desmarais, Women's Perceptions and Use of "Anti-Aging" Products, Sex Roles, 63(2010) 126-37.

[189] C.E. Mykytyn, Anti-aging medicine: A patient/practitioner movement to redefine aging, Social Science & Medicine, 62(2006) 643-53.

[190] I. Mevlitoglu, B. Engin, M. Kaplan, How Effective are Anti-Ageing Products?, Turkderm-Turkish Archives of Dermatology and Venerology, 43(2009) 2-6.

[191] I. Nesic, V. Savic, A. Kolarevic, Investigation of Efficacy of Anti-Aging Liposomal Intimate Gel: An In Vivo Long-Term Study, Acta Facultatis Medicae Naissensis, 37(2020) 48-56.

[192] C.C. Felippi, D. Oliveira, A. Stroher, A.R. Carvalho, E. Van Etten, M. Bruschi, et al., Safety and Efficacy of Antioxidants-Loaded Nanoparticles for an Anti-Aging Application, Journal of Biomedical Nanotechnology, 8(2012) 316-21.

[193] B. Eren, S.T. Tanriverdi, F.A. Kose, O. Ozer, Antioxidant properties evaluation of topical astaxanthin formulations as anti-aging products, Journal of Cosmetic Dermatology, 18(2019) 242-50.

[194] T.R. Chang, H. Li, H.N. Lv, M.H. Tan, S.B. Hou, X. Liu, et al., Extraction, Physicochemical Properties, Anti-Aging, and Antioxidant Activities of Polysaccharides from Industrial Hemp Residues, Molecules, 27(2022).

[195] G.P. Hong, S.G. Min, Y.J. Jo, Anti-Oxidative and Anti-Aging Activities of Porcine By-Product Collagen Hydrolysates Produced by Commercial Proteases: Effect of Hydrolysis and Ultrafiltration, Molecules, 24(2019).

[196] S.M. Ali, G. Yosipovitch, Skin pH: from basic science to basic skin care, Acta dermato-venereologica, 93(2013) 261-7.

[197] S. Eissa, R.A. Almthen, M. Zourob, Disposable electrochemical immunosensor array for the multiplexed detection of the drug metabolites morphine, tetrahydrocannabinol and benzoylecgonine, Microchimica Acta, 186(2019) 1-9.

[198] Y. Li, J. Hou, H. Zhou, M. Jia, S. Chen, H. Huang, et al., A fluorescence sensor array based on perylene probe monomer-excimer emission transition for the highly efficient differential sensing of metal ions and drinking waters, Sens. Actuators, B, 319(2020) 128212.

[199] C. Zhang, K.S. Suslick, A colorimetric sensor array for organics in water, J. Am. Chem. Soc., 127(2005) 11548-9.

[200] B.A. Suslick, L. Feng, K.S. Suslick, Discrimination of complex mixtures by a colorimetric sensor array: coffee aromas, Anal. Chem., 82(2010) 2067-73.

[201] J.A.R. Teodoro, H.V. Pereira, D.N. Correia, M.M. Sena, E. Piccin, R. Augusti, Forensic discrimination between authentic and counterfeit perfumes using paper spray mass

spectrometry and multivariate supervised classification, Analytical Methods, 9(2017) 4979-87.

[202] L.N. Al-Eitan, H.A. Aljamal, R.Q. Alkhatib, Gas chromatographic-mass spectrometric analysis of sunscreens and their effects on mice liver and kidney enzyme function, Clinical Cosmetic and Investigational Dermatology, 12(2019) 11-21.

[203] N.J. Sadgrove, Honest nutraceuticals, cosmetics, therapies, and foods (NCTFs): standardization and safety of natural products, Crit. Rev. Food Sci. Nutr., 62(2022) 4326-41.

[204] M. Malet-Martino, R. Martino, Analysis of Counterfeit Medicines and Adulterated Dietary Supplements by NMR, Emagres, 4(2015) 159-70.

[205] S. Paraschos, P. Magiatis, E. Gikas, I. Smyrnioudis, A.L. Skaltsounis, Quality profile determination of Chios mastic gum essential oil and detection of adulteration in mastic oil products with the application of chiral and non-chiral GC-MS analysis, Fitoterapia, 114(2016) 12-7.

[206] S.H. Cho, H.J. Park, J.H. Lee, J.A. Do, S. Heo, J.H. Jo, et al., Determination of anabolic-androgenic steroid adulterants in counterfeit drugs by UHPLC-MS/MS, J. Pharm. Biomed. Anal., 111(2015) 138-46.

[207] J. Fiori, V. Andrisano, LC-MS method for the simultaneous determination of six glucocorticoids in pharmaceutical formulations and counterfeit cosmetic products, J. Pharm. Biomed. Anal., 91(2014) 185-92.

[208] G. Pagliuca, C. Bozzi, F.R. Gallo, G. Multari, G. Palazzino, R. Porra, et al., Triacylglycerol "hand-shape profile" of Argan oil. Rapid and simple UHPLC-PDA-ESI-TOF/MS and HPTLC methods to detect counterfeit Argan oil and Argan-oil-based products, J. Pharm. Biomed. Anal., 150(2018) 121-31.

[209] S. Orecchio, R. Indelicato, S. Barreca, Determination of Selected Phthalates by Gas Chromatography-Mass Spectrometry in Personal Perfumes, Journal of Toxicology and Environmental Health-Part a-Current Issues, 78(2015) 1008-18.

[210] Y. Aghoutane, M. Brebu, M. Moufid, R. Ionescu, B. Bouchikhi, N. El Bari, Detection of Counterfeit Perfumes by Using GC-MS Technique and Electronic Nose System Combined with Chemometric Tools, Micromachines, 14(2023).

[211] B. Pacholczyk-Sienicka, G. Ciepielowski, L. Albrecht, The First Application of H-1 NMR

Spectroscopy for the Assessment of the Authenticity of Perfumes, Molecules, 26(2021).

[212] M. Zangheri, M.M. Calabretta, D. Calabria, J. Fiori, M. Guardigli, E. Michelini, et al., Immunological Analytical Techniques for Cosmetics Quality Control and Process Monitoring, Processes, 9(2021).

[213] H. Rebiere, A. Kermaidic, C. Ghyselinck, C. Brenier, Inorganic analysis of falsified medical products using X-ray fluorescence spectroscopy and chemometrics, Talanta, 195(2019) 490-6.

[214] T. Wang, X. Yang, J. Men, J. Zhou, H. Zhang, A near-infrared fluorescent probe based on boric acid hydrolysis for hydrogen peroxide detection and imaging in HeLa cells, Luminescence, 35(2020) 208-14.

[215] T. Wang, X. Yang, J. Men, J. Zhou, H. Zhang, A near-infrared fluorescent probe based on boric acid hydrolysis for hydrogen peroxide detection and imaging in HeLa cells, Luminescence, 35(2020) 208-14.

[216] H.T. Zhang, R.C. Liu, Y. Tan, W.H. Xie, H.P. Lei, H.Y. Cheung, et al., A FRET-based Ratiometric Fluorescent Probe for Nitroxyl Detection in Living Cells, Acs Applied Materials & Interfaces, 7(2015) 5438-43.

[217] J. Liu, H. Lu, Y. Liu, J. Zhang, C. Li, X. Xu, et al., Efficient Organic Solar Cells Based on Non-Fullerene Acceptors with Two Planar Thiophene Fused Perylene Diimide Units, ACS Appl Mater Interfaces, (2020).

[218] A.B. Descalzo, K. Rurack, On the signalling pathways and Cu(II)-mediated anion indication of N-meso-substituted heptamethine cyanine dyes, Chemistry, 15(2009) 3173-85.

[219] K. Kiyose, S. Aizawa, E. Sasaki, H. Kojima, K. Hanaoka, T. Terai, et al., Molecular design strategies for near-infrared ratiometric fluorescent probes based on the unique spectral properties of aminocyanines, Chemistry–A European Journal, 15(2009) 9191-200.

[220] F. Rispo, G. De Negri Atanasio, I. Demori, G. Costa, E. Marchese, S. Perera-del-Rosario, et al., An extensive review on phenolic compounds and their potential estrogenic properties on skin physiology, Frontiers in Cell and Developmental Biology, 11(2024) 1305835.

[221] L. Xiao-Jun, Y. Xue, Mechanism of fluorescence enhancement of HClO detected by excited-state intramolecular proton transfer based HBT-OMe molecule, Acta Phys. Sin.,

72(2023) 7.

[222] Y.J. Zhan, P. Yu, X.H. Wang, Y. Xie, H.X. Zhang, F. Zhang, Activatable NIR-II Lanthanides-Polymetallic Oxomolybdate Hybrid Nanosensors for Monitoring Chemotherapy Induced Enteritis, Adv. Funct. Mater., 33(2023) 10.

[223] J.J. Zhao, P.L. Zhai, B. Gu, S.P. Tang, A Readily Available Red-Emitting Methylthio-Substituted Salicylaldehyde Azine with AIE Feature for Ratiometric Detection of HClO, Anal. Sens., (2023) 8.

[224] L.A. Shangguan, X.L. Qian, Z.Y. Wu, T.T. Han, W.L. Sun, L. Liu, et al., A ratiometric nanoprobe for the in vivo bioimaging of hypochlorous acid to detect drug-damaged liver and kidneys, Analyst, 148(2023) 762-71.

[225] B.H. Ding, S.H. Han, H.Q. Xiong, B.H. Wang, B.J. Zuo, X.Z. Song, A Highly Selective Ratiometric Fluorescent Probe for the Detection of Hypochlorite in Acute Lung Injury, Chin. J. Org. Chem., 43(2023) 2878-84.

[226] B.W. Gong, S.Y. Zhang, X. Wang, G.Y. Ran, X.H. Zhang, J. Xi, et al., Inflammation Intensifies Monocrotaline-Induced Liver Injury, J. Agric. Food. Chem., 71(2023) 3433-43.

[227] B.W. Gong, S.Y. Zhang, X. Wang, G.Y. Ran, X.H. Zhang, J. Xi, et al., Inflammation Intensifies Monocrotaline-Induced Liver Injury, J. Agric. Food. Chem., (2023) 3433-43.

[228] V. Kumar, Megha, P. Kaur, K. Singh, Bis-cyanostilbene based fluorescent materials: A rational design of AIE active probe for hypochlorite sensing, Spectrochimica Acta Part a-Molecular and Biomolecular Spectroscopy, 302(2023) 11.

[229] S.J. Li, P.P. Wang, K. Yang, Y. Liu, D. Cheng, L.W. He, Construction of HClO activated near-infrared fluorescent probe for imaging hepatocellular carcinoma, Anal. Chim. Acta, 1252(2023) 8.

[230] S.J. Li, K. Yang, P.P. Wang, Y. Liu, D. Cheng, L.W. He, Monitoring heat stroke with a HClO-activatable near-infrared fluorescent probe, Sens. Actuators, B, 385(2023) 7.

[231] Y.Q. Li, Y. Zhou, X. Liu, J.N. Lei, X. Qin, G.Y. Li, et al., A NIR ratiometric fluorescence probe for rapid, sensitive detection and bioimaging of hypochlorous acid, Spectrochimica Acta Part a-Molecular and Biomolecular Spectroscopy, 302(2023) 7.

[232] Z. Li, M.X. Tan, N.C. Lian, F. Ke, F. Zhang, C.S. Wang, et al., A cyanine carbazole oxime

fluorescent probe selectively detects hypochlorite in Hi5 cells and C. elegans, Tetrahedron Lett., 118(2023) 6.

[233] D. Liu, X.X. Yue, H.K. Zhang, K. Li, Z.H. Yang, B.H. Wang, et al., Probing drug-mediated fluctuations of HClO levels in the endoplasmic reticulum by a ratiometric fluorescent probe with a large emission shift, Dyes and Pigments, 215(2023) 7.

[234] Q.L. Liu, X. Li, M. Xiao, Y. Ai, G. Liu, H.C. Ding, et al., A "Turn-on" Fluorescent Probe Based on Phenothiazine for Selectively Recognizing ClO⁻ and its Practical Applications, Journal of Fluorescence, (2023) 9.

[235] Q.L. Liu, M. Xiao, H.C. Ding, C.B. Fan, G. Liu, S.Z. Pu, A water-soluble colorimetric and ratiometric fluorescent probe based on phenothiazine for the detection of hypochlorite ion, Dyes and Pigments, 215(2023) 7.

[236] X.T. Mao, S. Xu, C.X. Wu, C.B. Fan, D.B. Zhang, S.Z. Pu, Development of a lysosome-targeted iridium (III) complex-based fluorescent probe for detection of HOCl and its application in living cells and water samples, Inorg. Chim. Acta, 556(2023) 8.

[237] M. Rabha, S.K. Sheet, B. Sen, I. Konthoujam, K. Aguan, S. Khatua, Ruthenium(II) Complex-based Highly Specific Luminescence Light-up Probe for Detecting HOCl via C(sp²)-H Chlorination, ChemistrySelect, 8(2023) 9.

[238] H.M. Shangguan, Q.W. Liu, Y.J. Wang, Z.X. Teng, R.M. Tian, T. Wu, et al., Bioimaging of a chromenoquinoline-based ratiometric fluorescent probe for detecting ClO⁻, Spectrochimica Acta Part a-Molecular and Biomolecular Spectroscopy, 303(2023) 8.

[239] Y.M. Tian, G.B. Liu, W.N. Wu, X.L. Zhao, X.F. Han, Y.C. Fan, et al., A p-toluenesulfonamide-modified benzo h chromene hydrazone: Fluorescent turn-on detection of hypochlorite and its application to imaging the endoplasmic reticula of living cells and zebrafishes, Spectrochimica Acta Part a-Molecular and Biomolecular Spectroscopy, 296(2023) 8.

[240] S.Q. Tu, M.X. Tan, Y.L. Guo, X.Y. Wu, L.P. Li, W. Li, et al., A big blue-shift phenanthroline fluorescent probe with for detecting hypochlorous acid in live cells, Tetrahedron Lett., 117(2023) 6.

[241] X.F. Wang, Z.Y. Cheng, J.J. Wu, F. Yang, Z.Z. Zhang, F. Tang, et al., Rapid and sensitive

detection of endogenous HClO in living cells and zebrafish using a phenothiazine-based fluorescent probe, Tetrahedron, 145(2023) 6.

[242] W.J. Xu, Z.Q. Li, D.Y. Tan, Q.X. Liu, S.X. Su, Y.D. Chen, et al., Intracellular biothiols assisted triple-channel imaging of mitochondrial HClO in living cells, Sens. Actuators, B, 393(2023) 8.

[243] R. Yu, W. Kan, X. Qi, Y. Zhang, L.M. Ding, L.Y. Wang, et al., An ICT phenanthro 9,10-d imidazole-based fluorescence probe with aggregated characteristic for colorimetric detection of hypochlorous acid and its applications in water samples and living cells, Inorg. Chim. Acta, 558(2023) 7.

[244] Y. Yuan, S.Z. Xiong, L.Q. Lv, W. Hu, X.X. Xiong, C.Y. Li, et al., A dual lock-and-key probe for high-fidelity visualizing abdominal aortic aneurysm-related inflammation via a PET-TICT integrated near-infrared platform, Chem. Eng. J., 471(2023) 9.

[245] H. Zhang, Q.C. Feng, J.T. Hou, Z.P. Li, J.L. Shen, Carboxy Bodipy-Based Fast Trigger Fluorescent Probe for Imaging Endogenous Hypochlorous Acid, Chemosensors, 11(2023) 11.

[246] X.W. Zhang, F. Zhang, B.S. Yang, B. Liu, A dual-site fluorescent probe for discriminately detecting low and high concentration of hypochlorite in living cells, Spectrochimica Acta Part a-Molecular and Biomolecular Spectroscopy, 299(2023) 8.

[247] Z.Y. Zhang, L.L. Ma, Y.L. Huang, Y. Zhou, H. Zhang, J.W. Yan, et al., A facile ratiometric near-infrared fluorescent probe using conjugated 1,8-naphthalimide and dicyanoisophorone with a vinylene linker for detection and bioimaging of hypochlorite, Analytical Methods, 15(2023) 3420-5.

[248] Y. Zheng, S. Wu, Y.F. Bing, H.M. Li, X.Q. Liu, W.L. Li, et al., A Simple ICT-Based Fluorescent Probe for HOCl and Bioimaging Applications, Biosensors-Basel, 13(2023) 11.

[249] J.H. Zhu, C.C. Miao, X.C. Wang, Designing a turn-on ultrasensitive fluorescent probe based on ICT-FRET for detection and bioimaging of Hypochlorous acid, Spectrochimica Acta Part a-Molecular and Biomolecular Spectroscopy, 294(2023) 7.

[250] H.C. Ding, L.S. Yue, Y. Ai, Z.F. Zhu, C.B. Fan, G. Liu, et al., A dual-responsive fluorescent probe based on cyanine and naphthalimide units for detecting HClO and H2S in living cells, Spectrochimica Acta Part a-Molecular and Biomolecular Spectroscopy, 304(2024)

8.

[251] L.L. Yang, L.F. Li, R.Y. Liu, C.G. Xie, J. Zhao, W.G. Chang, et al., Cationic fluorescent carbon dots with solution ultra-stability and its rapid/ on-site sensing application for HClO, Talanta, 267(2024) 9.

[252] M.Á. Moro, V.M. Darley-Usmar, I. Lizasoain, Y. Su, R.G. Knowles, S. Moncada, et al., The formation of nitric oxide donors from peroxynitrite, Br. J. Pharmacol., 116(1995) 1999-2004.

[253] A. Liang, H. Wang, Y. Chen, X. Zheng, T. Cao, X. Yang, et al., Benzoselenadiazole-based donor-acceptor small molecule: Synthesis, aggregation-induced emission and electroluminescence, Dyes and Pigments, 149(2018) 399-406.

[254] P. Zhang, S. Li, C. Fu, Q. Zhang, Y. Xiao, C. Ding, A colorimetric and near-infrared ratiometric fluorescent probe for the determination of endogenous tyrosinase activity based on cyanine aggregation, Analyst, 144(2019) 5472-8.